1-1-2017

Synthesis Of Discrete Transition Metal (ni, Fe, Co, Mn) Phosphide Nanoparticles: Compositional Effect On Catalytic And Magnetic Properties

Da Li
Wayne State University,

SYNTHESIS OF DISCRETE TRANSITION METAL (Ni, Co, Fe, Mn) PHOSPHIDE NANOPARTICLES: COMPOSITIONAL EFFECT ON CATALYTIC AND MAGNETIC PROPERTIES

by

DA LI

DISSERTATION

Submitted to Graduate School

of Wayne State University,

Detroit, Michigan

in partial fulfillment of the requirements

for the degree of

DOCTOR OF PHILOSOPHY

2017

MAJOR: CHEMISTRY (Inorganic)

Approved By:

_____

Advisor Date

_____

_____

_____

_____

DEDICATION

To Yan Chen and Huaiming Li

ACKNOWLEDGEMENTS

First and foremost, I would like to express my deepest appreciation and thanks to my advisor Dr. Stephanie L. Brock. It has been an honor to be one of her Ph.D. students. She has always been extraordinarily patient and supportive in mentoring me to become an independent and creative scientist. Her enthusiasm for research has always motivated me. She provided me the best opportunities and experiences I could ever ask for.

I want to thank my undergraduate advisor, Jinku Liu, who brought my interest into the “Nano” world. He has been encouraging me all these years and always has faith in me. Without him, I would not even have the opportunity to pursue a career as scientist in the US.

I would like to thank my committee members, Dr. Stanislav Groysman, Dr. Jennifer L. Stockdill, and Dr. Eranda Nikolla. They have provided numerous brilliant comments and feedback, which make this dissertation work in a better shape.

I have had pleasure of working with many talented collaborators, Dr. Claudio Verani and Habib Baydoun, Dr. Eranda Nikolla and Ayad Nacy, Dr. Gavin Lawes and Maheshika Palihawadana. They offered me numerous intellectual ideas.

I would like to thank my colleagues and my friends, Habib and Ruchira. You all have provided selfless support and sincere friendship over these years. I want to thank my other lab mates, Lathansa, Roshini, Derak, Jessica, Indika, Malsha, Sam, Tepora, Lakmini, Lalani, Krista, Bogdan, Kody and Mikaylah. I’m so lucky to work and be around with them.

I would like to thank staff members in the Lumigen Instrument Center. Thank Dr. Zhi Mei (Mike) for helping me to use TEM and SEM, Dr. Philip Martin for his help with PXRD. My gratitude is also extended to Dr. Munk for guiding me in teaching. It has been so inspiring and cheerful to work with her. I also want to thank Melissa and Bernie for giving tremendous help no matter what task or circumstance I brought to them.

I would like to thank National Science Foundation and Wayne State University for supporting my PhD study financially (CHE-1361741, DMR-1631470, Thomas C. Rumble Fellowship, summer dissertation fellowship) and providing me the chance to fully focus on my research study.

Last but not the least, I would like to thank my parents, Yan Chen and Huaiming Li. Their unconditional support and endless love is always my strongest motivation. I would like to thank my aunt Xin Li and her family for giving me a second home in the United States. I would also like to thank my girlfriend, Shirley. Her encouragement, quiet patience and unwavering love were extremely important for the past four years of my life.

PREFACE

This dissertation is based closely on the following refereed publications:

Chapter 3: Li, D., Senevirathne, K., Aquilina, L., Brock, S. L. Inorganic Chemistry, **2015**, 54, 7968-7975.

Chapter 4: Li, D., Perera, M., Kulikowski, B., Lawes, G., Seda, T., Brock, S. L. Chemistry of Materials, **2016**, 28, 3920-3927.

Chapter 5: Li, D., Baydoun, H., Verani, C. N., Brock, S. L. Journal of the American Chemical Society, **2016**, 138, 4006-4009.

Chapter 6: Li, D., Baydoun, H., Kulikowski, B., Brock, S. L. Chemistry of Materials, **2017**, 29, 3048-3054.

Chapter 7: Li, D., Whisnant K. G., Brock, S. L. "Visible Light Induced Photocatalytic Hydrogen Evolution Using a Ni_2P-CdS Hybrid Aerogel System." In preparation.

TABLE OF CONTENTS

LIST OF SCHEMES

LIST OF TABLES

LIST OF FIGURES

LIST OF ABBREVIATIONS

SPAP	solution-phase arrested-precipitation
MPs	Metal phosphides
TOP	Trioctylphosphine
TOPO	Trioctylphosphine oxide
OE	octyl either
ODE	octadecene
OAm	oleylamine
TEM	transmission electron microscopy
HRTEM	high solution transmission electron microscopy
FFT	fast Fourier transform
EDS	energy dispersive spectroscopy
STEM	scanning transmission electron microscopy
HAADF	high angle annular dark field
ICP-MS	inductively coupled plasma-mass spectrometry
IR	infrared
DFS	diffuse reflectance spectroscopy
CV	cyclic voltammetry
BET	Brunauer-Emmett-Teller
BJH	Barrett-Joyner-Halenda
FC	field-cooled
ZFC	zero-field-cooled
RDE	rotating disc electrode
OER	oxygen evolution reaction

HER	hydrogen evolution reaction
ICP-MS	inductively coupled plasma mass
XPS	X-Ray photoelectron spectroscopy
PECVD	plasma enhanced chemical vapor deposition
RHE	reversible hydrogen electrode
HDS	hydrodesulfurization
HDO	hydrodeoxygenation
PCET	proton-coupled electron transfer
CPE	controlled potential electrolysis

CHAPTER 1. INTRODUCTION

Solid materials that have one or more dimensions within 1-100 nm range are defined as nanomaterials. The dimensions within this range are usually composed of 10-500 atoms closely arranging to each other. Due to the limited number of atoms, nanomaterials can have unique magnetic, optical, or electronic properties when compared to their relative bulk phases, such as the quantum confinement in quantum dots, the superparamagnetism of iron oxide nanoparticles, and the surface plasmon resonance of gold nanoparticles. Moreover, because nanomaterials have large surface to volume ratios, they are highly surface activate. Therefore, nanomaterials are considering as promising candidates for catalytic, photovoltaics, drug delivery and many other new technological applications.

Due to the wide range of unique magnetic, redox and catalytic properties exhibited by transition metal phosphides, the development of methods for their production on the nanoscale with control of size, shape and composition, is an important endeavor.[1-4,5-9] Over the last 15 years, the Brock group has developed various methods to prepare different binary transition metal pnictide and chalcogenide nanomaterials with fine control over size, shape and composition for applications such as hydrodesulfurization (HDS) and hydrodeoxygenation (HDO), magnetic refrigeration, and thermoelectric devices. Recently, ternary metal phosphides have attracted enormous attention due to the superior catalytic performance over the binary phases. Therefore, the Brock group are now focusing on establishing the synthetic factors that enable access to different phase-pure

ternary transition metal phosphides and studying the synergetic interaction or electronic modulation between the two metals.

In this dissertation, the research is focused on: (1) optimizing the synthesis of nanoscale phase-pure Ni_5P_4 and NiP_2 by establishing the relationship between critical synthetic parameters and the phase of nickel phosphide produced; (2) Synthesizing $Co_xFe_{2-x}P$ nanoparticles with different compositions, establishing the mechanism of nanoscale ternary phosphide formation and studying the magnetic properties of $Co_xFe_{2-x}P$ nanoparticles as a function of composition (3) Synthesizing $M_{2-x}Mn_xP$ (M = Co, Fe) nanoparticles with different compositions, establishing the mechanism of nanoscale ternary phosphide formation and studying the oxygen evolution reaction activity from water using $M_{2-x}Mn_xP$ (M = Co, Fe) nanoparticles as electro-catalysts; (4) Combining metal chalcogenide semiconductor aerogel with Ni_2P nanoparticles to achieve efficient photocatalytic hydrogen evolution reaction (HER) from water splitting.

The relevant background Information of solution phase synthesis of binary and ternary transition metal phosphides, magnetism, electrocatalytic oxygen evolution, and photocatalytic hydrogen evolution catalysis are described in this chapter.

1.1 Solution-phase Arrested Precipitation Synthesis of Nanomaterials

The solution-phase arrested-precipitation (SPAP) method was employed for synthesizing all nanomaterials in this dissertation. Typically, for the synthesis of metal phosphide nanoparticles using this method it involves the decomposition of organometallic reagents in mixtures of high boiling solvents/coordinating ligands and subsequent reaction of the generated metallic species with phosphines to

generate transition metal phosphides. As shown in **Figure 1.1**, La Mer's model of nucleation and growth can be used to explain the formation of highly monodisperse nanocrystals. When injecting the precursors rapidly into a hot solvent, monomers form due to the thermal decomposition of precursors (**Figure 1.1a**). The concentration of monomers keeps increasing until reaching a critical concentration known as the nucleation threshold and monomers start being consumed through the nucleation (**Figure 1.1b**). With the nucleation process going on, the concentration of monomers saturates due to the equilibrium between the monomer generation and consumption (**Figure 1.1c**). After this point, the monomer consumption rate becomes higher than the generation rate, causing the decrease of monomers concentration. When the concentration of monomers becomes lower than the nucleation threshold, formation of new nuclei ceases and the addition of monomers to existing nuclei becomes more favorable (**Figure 1.1d**). When the concentration of monomer is further decreased, particle growth takes place with Ostwald ripening (**Figure 1.1e**). In Ostwald ripening, smaller particles with higher surface energy are dissolved by larger particles. The longer the reaction time, the longer Ostwald ripening will remain, which results in bigger average particle size. While the metal precursors are decomposed in the presence of coordinating ligands, these ligands can bond to the surface of newly formed particles and thus control particle growth. Longer chain ligands can limit particle growth and minimize particle aggregation. Crystals prefer to grow on the facet that bonded with less ligands and result in 1D or 2D materials. The selection of precursor reagents is also important, because the monomer generation rate can be varied by using

precursors with different chemical activities and result in different final particle sizes. In general, the control over the synthesis of nanoparticles can be achieved by changing a variety of reaction conditions in the SPAP method.

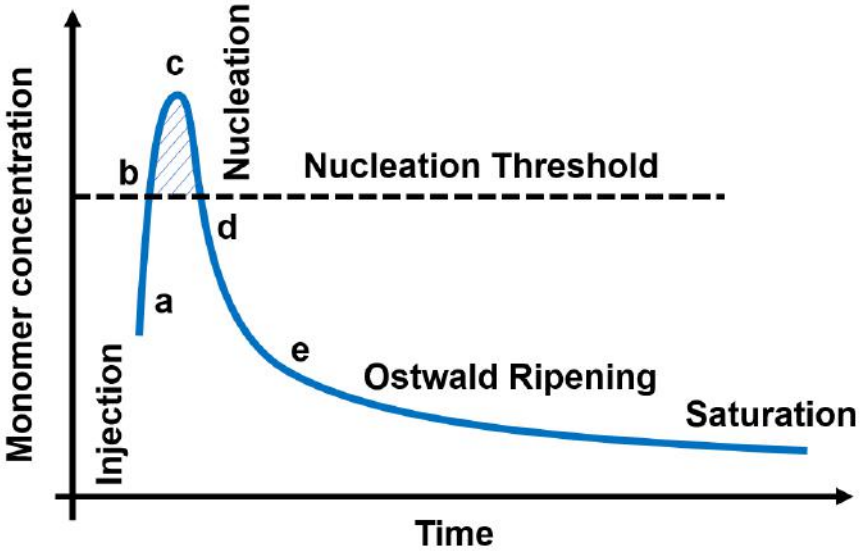

Figure 1.1. Schematic illustration of La Mer's model for nucleation and growth.

1.2 Transition Metal Phosphides

Metal phosphides (MPs) nanomaterials show a wide range of properties and are attracting enormous attention. Metal-rich nickel phosphides such as Ni_2P are potent hydrotreating catalysts[1, 2, 5, 8, 10-12] while the more phosphorus-rich phases such Ni_5P_4 and NiP_2 are promising candidates for lithium ion battery electrode materials, due to their high gravimetric and volumetric capacity.[13, 14] Furthermore, all of these phases show considerable potential to be used in hydrogen evolution catalysis.[15-17] Ternary phosphides of formula $Ni_{2-x}Co_xP$ and $Ni_{2-x}Fe_xP$ have shown improved hydrodesulfurization (HDS) activity relative to the best of the binary phases (Ni_2P) for low concentrations of Co and Fe ($x \leq 0.1$). Transition metal phosphide nanoparticles are also emerging as a new class of water oxidation catalysts with reports of high activity in binary metal phosphides such as Ni_2P,[18-20] Co_2P,[21, 22] and CoP.[23-25] Recently, the ternary metal phosphides CoFeP, NiCoP, and NiFeP have shown improved OER activity over the binary phases (Co_2P, Fe_2P or Ni_2P), attributed to synergism between the two metals.[22, 26-29] a phenomenon also observed in for CoMnP.[28] Because the magnetic and catalytic properties of transition metal phosphides depend on the size and shape (in the nano regime) as well as the composition,[5-9] there has been considerable effort made to synthesize transition metal phosphide nanomaterials as described below.

1.2.1 Synthesis of Binary Transition Metal Phosphides: Ni, Co, Fe, Mn

1.2.1.1 Nickel Phosphide

Nanoparticles of metal-rich nickel phosphides can be synthesized by the decomposition of organometallic species, or decomplexation of metal complexes,

to generate active nickel species, and their subsequent reaction with alkyl phosphines (e.g. trioctylphosphine TOP).[30] While the reactive form of P is not known, PH_3 generated from alkene elimination steps has been purported to be the active species in nickel phosphide formation. Thus, TOP acts as both a coordinating solvent and a reactant and is used as a nonstoichiometric precursor (in large excess), making it difficult to control the evolution between different phases. The Schaak Group first reported the synthesis of discrete Ni_2P nanoparticles by injecting a mixture of $Ni(acac)_2$ and TOP into a hot solution. In this method, Ni nanoparticles first formed and then be converted into Ni_2P hollow nanoparticles by TOP.[31] Later in the same year, the Brock group reported on the formation of solid spherical Ni_2P nanoparticles prepared by the reaction of bis(1,5-cyclooctadiene)-nickel(0) and TOP at 345 °C in trioctylphosphine oxide (TOPO).[8] Another study by the Brock group, in which nickel acetylacetonate was used as the nickel source, established the role of reaction parameters, such as reactant concentration, time, temperature and co-solvent (oleylamine), in determining the final stoichiometric phase: $Ni_{12}P_5$ vs Ni_2P and the degree to which hollow particles formed due to the Kirkendall effect.[32] This study and others showed that precursor particles, which serve as templates for the final crystalline phosphide product, form when the reactants are first heated at 230 °C.[32] For P/Ni ratios larger than 2.24, heating the Ni source and TOP at 230 °C will form relatively small (< 10 nm) amorphous Ni_xP_y nanoparticles, whereas at lower ratios, relatively large (> 20 nm) crystalline Ni nanoparticles are formed as the templating intermediates. Increasing TOP quantity, reaction temperature and reaction time favors the transformation of

the intermediate particles to the Ni_2P phase in lieu of the more metal-rich $Ni_{12}P_5$ phase. In contrast, increasing the oleylamine (OAm), which served as both reducing agent and surfactant, to nickel ratio results in a more metal-rich phase and reduces the Kirkendall effect, resulting in a reduction in the size of hollows in particles prepared from large crystalline Ni nanoparticle templates.[32]

Despite considerable attention on metal-rich phosphides, little research on the synthesis of phosphorus-rich nickel phosphides nanoparticles has been published.[14, 33] The Tatsumisago group reported a synthetic method for phase-pure Ni_5P_4 and NiP_2, with the phase selectivity achieved by using different Ni precursors (nickel acetylacetonate and nickel acetate tetrahydrate) in combination with TOP in TOPO, but the mechanism of phase control and the key factors that underscore selectivity were not presented.[14]

1.2.1.2 Iron Phosphide

The first synthesis of FeP nanoparticles was reported by our group, in which iron acetylacetonate was treated with highly reactive tristrimethysilyl phosphine ($P(SiMe_3)_3$) at temperatures in the range 240-320 °C using TOPO as solvent.[34] Phase-pure FeP nanoparticles with an average size of 4.65 nm were prepared. Hyeon and coworkers reported the formation of Fe_2P nanorods by injecting iron pentacarbonyl ($Fe(CO)_5$) in TOP into a mixture of octylether and oleylamine at 300 °C.[35] In this case, slower injection rates and additional injection of iron precursor favored longer nanorods. Later, a work addressing the roles of the different synthetic levers in determing the phases of iron phosphides was reported by Brock and coworkers. Fe_2P and FeP nanoparticles were synthesized by reacting Fe

nanoparticles (prepared by decomposing $Fe(CO)_5$ in a mixture of OAm and octadecene at 200 °C) with TOP at temperatures in the region of 350-385 °C, in which shorter reaction and lower temperatures favored the more metal-rich phase Fe_2P.[6]

1.2.1.3 Cobalt Phosphide

The Robinson group studied the diffusion processes that occur during the phase transformation of Co to Co_2P to CoP nanoparticles from reaction with TOP.[36] Co nanoparticles were synthesized by injecting $Co_2(CO)_8$ into 180 °C 1,2-dichlorobenzene, in which TOPO was used as a stabilizing agent. Reacting Co nanoparticles with TOP generated Co_2P nanoparticles and further reacting Co_2P nanoparticles with TOP generated CoP nanoparticles. However, in this case, the Co_2P nanoparticles are not highly uniform (they exist as both hollow big particles and small dense particles).

The Robinson group also reported that reacting $Co(oleate)_2$ with trioctylphosphine oxide (TOPO), normally a coordinating solvent in other systems, leads to Co_2P hyperbranched nanocrystals. In this study, TOPO is found to be not only the coordinating solvent but also as the P source at the first time. The final morphology of Co_2P can be controlled from hexagonal symmetric structures to sheaflike structures by varying the concentration of the surfactant.

1.2.1.4 Manganese Phosphide

Nanoparticles of manganese phosphides are notoriously difficult to make. The synthesis of manganese phosphide nanoparticles was first reported by our group using manganese carbonyl ($Mn_2(CO)_{10}$) and $P(SiMe_3)_3$ at a reaction temperature

higher then 220 °C.[37] TOP was also used as P source by our group to prepare MnP nanorods, in which a mixture of $Mn_2(CO)_{10}$ and TOP was injected into a hot TOPO solution.[38] Nanoparticles of the metal rich Mn_2P phase have

not been reported, presumably due to the highly oxophilic nature of manganese.

1.2.2 Synthesis of Ternary Transition Metal Phosphides.

For ternary phosphide nanomaterials, $Ni_xCo_{2-x}P$ nanoparticles were prepared by substituting $Ni(acac)_2$ with $Co(acac)_2$ for the corresponding Co metal amount.[39] For this ternary phosphide, phase-pure compositions were prepared up to x=1.7. For Ni rich compositions, solid spherical particles were observed while with increasing the amount of Co, hollow particles appeared, indicative of the higher mobility of Co metal in the phosphide lattice. From a detailed mechanistic study for Ni:Co=1:1 composition, it was determined that the particle sizes and morphology could be controlled by varying the initial M:P ratio.

1.2.2.1 Nickel Iron Phosphide

A protocol for synthesizing $Ni_xFe_{2-x}P$ nanoparticles was reported by our group.[40] By introducing $Fe(CO)_5$ into the Ni_xP_y solution (prepared by heating $Ni(acac)_2$, TOP, oleylamine, and octyl ether at 230 ºC), Fe is diffused into the Ni_xP_y forming a Ni-Fe-P alloy and this alloy was crystallized to form the final ternary phosphide at high temperatures. Using this approach, phase pure $Ni_{2-x}Fe_xP$ nanoparticles were prepared over the whole composition range ($0 \leq x \geq 2$). In these ternary phosphide particles, the spherical morphology observed in Ni-rich compositions shifted to nanorods in Fe-rich compositions.

1.2.2.2 Cobalt Iron Phosphide

The Han group reported the synthesis of anisotropic cobalt-iron phosphide nanocrystals using Co and Fe oleate precursors in the presence of oleylamine (OAm) and trioctylphosphine (TOP).[36] However, they only reported two compositions, both at the Co-rich end of the solid solution, $Co_{1.5}Fe_{0.5}P$ and $Co_{1.7}Fe_{0.3}P$. Subsequently, the Sun group reported an approach to synthesize $Co_xFe_{2-x}P$ over all x using Fe and Co acetylacetonate precursors.[26] In this case, Co-Fe-O is prepared first and then converted into Co-Fe-P by reaction with TOP at high temperature. However, the need for a two-step synthesis and the unpredictable metal ratio change from mixed-metal oxides to ternary metal phosphides ($(Co_{0.08}Fe_{0.92})_3O_4$, $(Co_{0.38}Fe_{0.62})_3O_4$ and $(Co_{0.66}Fe_{0.33})_3O_4$ produced $(Co_{0.16}Fe_{0.84})_2P$, $(Co_{0.47}Fe_{0.53})_2P$ and $(Co_{0.79}Fe_{0.21})_2P$, respectively) increases the complexity of targeting desired compositions. Moreover, the average size of the final products in $Co_xFe_{2-x}P$ particles prepared to date are more than 100 nm in diameter and the methods lack the ability to control size.

1.2.2.3 Manganese Iron Phosphide

Whitmire and coworkers reported a synthesis of Fe-rich $Fe_{2-x}Mn_xP$ nanoparticles using $FeMn(CO)_8(\mu\text{-}PH_2)$ as a single-source molecular precursor.[41] However, the need to prepare the single molecule precursor increased the complexity of this synthesis and Mn incorporation was limited and unpredictable.

1.3 Magnetism

All materials exhibit magnetism and show different responses to external magnetic fields due to the orientation of their magnetic moments. Depending on

the structure of materials, the orientation of their magnetic moments, and their responses to the external applied magnetic field, materials can be classified into 5 types as shown in **Figure 1.2**. Magnetic susceptibility (χ) is defined as the ratio between magnetization (M) and the applied field (H).

1.3.1 Diamagnetism

Diamagnetic materials don't have unpaired electrons and their net magnetic moment is zero. They are repelled by an external magnetic field because their magnetic susceptibility (χ) values are negative and very small (~-10^{-5}). As shown in **Figure 1.2b**, the response of magnetization as a function of applied field for diamagnetic materials is linear and reversible with a negative slope. Diamagnetism occurs in all materials. However, this weak effect is overcome by other magnetism if unpaired electrons exist in the material.

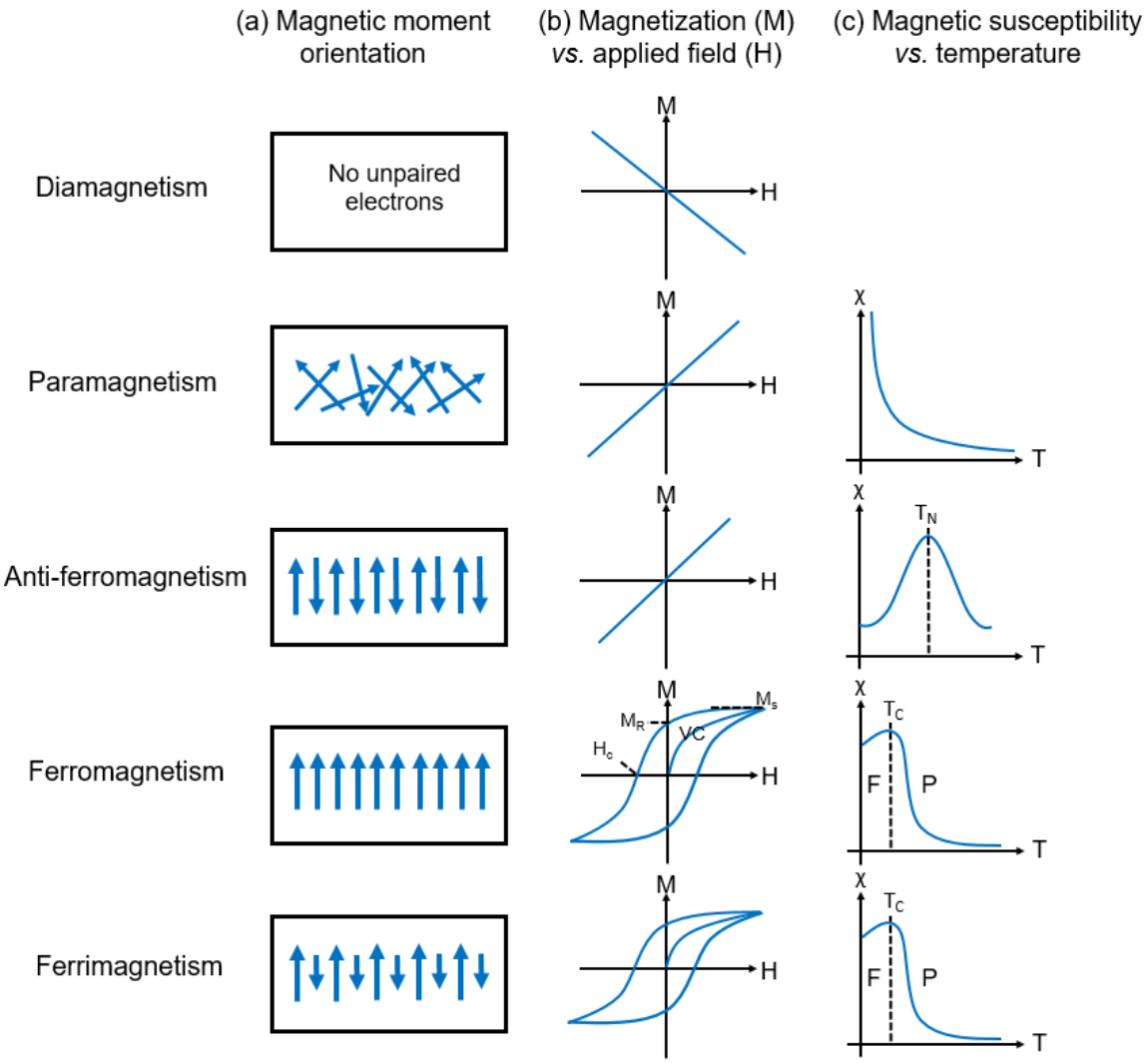

Figure 1.2. Illustration of (a) magnetic moment orientation in different types of magnetism. Typical curves of (b) magnetization (M) as a function of applied magnetic field (H) and (c) magnetic susceptibility (χ) as a function of temperature (T).

1.3.2 Paramagnetism

when unpaired electrons exist and magnetic moments are oriented randomly in a material (**Figure 1.2a**), the material is classified as paramagnetic material. The net magnetic moment in this material is positive no matter whether an external field is applied or not. When an external field is applied, the magnetic moments align parallel with the field direction. The susceptibility for a paramagnetic material is small but positive (10^{-3} – 10^{-5}) and the magnetization increases linearly with increasing applied magnetic field (**Figure 1.2b**). In addition, the susceptibilities of paramagnetic materials are inversely proportional to their temperature as shown in **Equation 1.1** and **Figure 1.2c**, in which C is the Curie constant, a property that relates a material's magnetic susceptibility to its temperature, and T is temperature.

$$\chi = C/T \qquad \text{Equation 1.1}$$

1.3.3 Anti-ferromagnetism

When unpaired electrons exist and neighboring magnetic moments with the same magnetization point in opposite directions, it results in a cancelation (**Figure 1.2a**) and anti-ferromagnetism occurs. The magnetization of anti-ferromagnetic materials increase linearly with increasing applied field. The susceptibility of this type material is small, positive (0 – 10^{-2}), and temperature dependent. As shown in **Figure 1.2c**, the susceptibility first increases with increasing temperature and then decreases after a certain point. The temperature at this point is called Nèel temperature (T_N). When the temperature is above T_N, anti-ferromagnets behave similarly to paramagnets.

1.3.4 Ferromagnetism

when unpaired electrons exist and magnetic moments align parallel in the same direction, resulting a large net magnetization without the applied magnetic field (**Figure 1.2a**), ferromagnetism occurs. Ferromagnetic materials are the most important class of magnetic materials as they can be utilized in various applications such as data storage, magnetic refrigeration, and transformers. The magnetic susceptibilities of ferromagnetic materials are large, positive (>> 1), and temperature dependent. As shown in (**Figure 1.2a**), the susceptibility first increases with increasing temperature until the transition temperature, which is known as Curie temperature (T_C), is reached. When the temperature is above T_C, the magnetic moments no longer align parallel in the same direction, which causes the decrement of the susceptibility. Because of the disordered alignment of the magnetic moments, the material becomes paramagnetic.

The magnetization of a ferromagnetic material first increases with the steadily increasing applied magnetic field until it reaches a saturation. The magnetization at this saturation point is called saturation magnetization (M_S) and this first curve is the virgin curve (VC, **Figure 1.2b**). When the magnetization saturates, all the magnetic moments align in the same direction with the applied field. When the applied field steadily decreases to zero, the magnetization decreases, but not to zero, resulting in hysteresis. This indicates that partial magnetization remains even after removing the applied magnetic field, which is a typical trait of ferromagnetic materials. The remaining magnetization remained is called the remnant magnetization (M_R). When the applied field starts increasing steadily in the opposite direction, the magnetization can be reduced to zero and the magnitude

of the applied field at this point is called the coercivity (H_C). When the applied field continues increasing steadily, the magnetization will saturate again. The values of M_S and H_C are important parameters when ferromagnetic materials are used as practical applications. For example, materials that have relatively high H_C are preferred for data storage applications, while magnetic refrigeration candidates should have low H_C values.

1.3.5 Ferrimagnetism

When unpaired electrons exist and neighboring magnetic moments with different magnitudes align antiparallel, a net magnetization without the applied magnetic field results (**Figure 1.2a**) and ferrimagnetism occurs. Ferrimagnetic materials exhibit similar behavior to ferromagnetic materials and have all the typical traits of ferromagnetic materials (hysteresis, T_C, remnant magnetization, **Figure 1.2c**) except they have a smaller magnetic moment.

1.4 Magnetic Behavior of Nanomaterials

Regions known as magnetic domains exist in all ferromagnetic materials. In this region, all magnetic moments align in the same direction and produce a net magnetic moment (**Figure 1.3a**). However, a material can have multiple magnetic domains that are separated by domain walls. These magnetic domains have different orientations and thus affect the net magnetic field produced. When an external magnetic field is applied, magnetic domains that align in the same direction with the field start growing at the expense of other domains (**Figure 1.3a**) by migrating domain walls. With the decrease in particle size, the formation of domain walls is no longer energetically favorable and thus each particle only has

one magnetic domain. Once the particle size drops below a critical diameter (D_C), the reversal of magnetization occurs through coherent rotation instead of domain wall migration (**Figure 1.3b**). The coherent rotation requires a higher energy and thus results in higher coercivity values of nanoparticles than those of bulk materials. However, when the size is sufficiently small, the magnetic moments in nanoparticles can be affected by thermal fluctuations and nanoparticles exhibit superparamagnetism. Superparamagnetic materials can be magnetized to a saturated state by an external field and hysteresis is no longer observed **(Figure 1.4b)**.

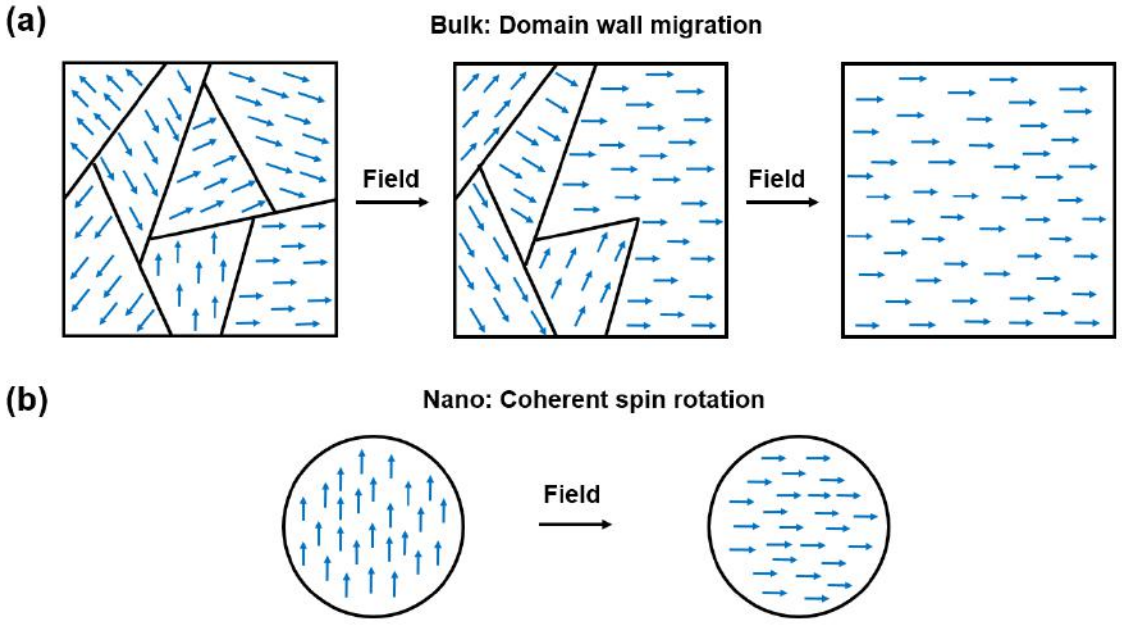

Figure 1.3. Magnetic moment alignments of bulk and nano ferromagnetic materials.

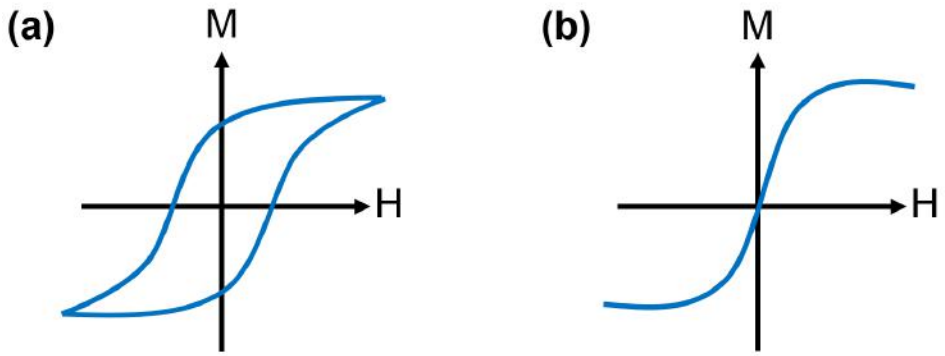

Figure 1.4. Comparison of the magnetization (M) *vs.* applied magnetic field (H) curves of (a) ferromagnetic and (b) superparamagnetic materials.

When the temperature is sufficiently low, thermal fluctuations are weak so magnetic moments become blocked. This temperature is called the blocking temperature (T_b). When above the T_b, the magnetism will transit from ferromagnetic to superparamagnetic.

As shown in **Figure 1.5**, the T_b of superparamagnetic nanoparticles can be determined by employing zero-field-cooled (ZFC) and field-cooled (FC) magnetization *vs.* temperature experiments in a low field (on the order of 100 Oe). During ZFC measurement, the nanoparticles are cooled in a zero-magnetic field, freezing the magnetic moments in random orientations. An external magnetic field is applied and the temperature is slowly ramped up. Thermal motion enables alignment of magnetic moments with the field through coherent spin rotation, causing the increase of the magnetization. At T_b, when thermal fluctuations are strong enough to re-orient spins randomly, the magnetization saturates. FC plots are collected by cooling nanoparticles in an applied field and then ramping the temperature up gradually in the presence of an applied magnetic field. When nanoparticles are cooled in a magnetic field, the magnetic moments are frozen and pointing in the same direction with the applied field. The magnetization remains constant regardless of the increasing temperature until T_b is approached, at which point the moments randomize and a decrease in magnetization occur. Above T_b, both ZFC and FC curves show paramagnetic behavior and the magnetization decreases with the increasing temperature. T_b is normally determined from the peak of the ZFC curve (**Figure 1.5**). The T_C of nanoparticles can be estimated from the first derivation of ZFC and FC curves. A more accurate T_C determination of

nanoparticles can be obtained by carrying out M vs. H measurements at different temperatures close to the T_C estimated from ZFC and FC curves. These so-called Arrott plots are obtained by plotting M^2 vs. H/M at different temperatures. At T_C, a linear curve that passes through the origin is observed in Arrott plots.

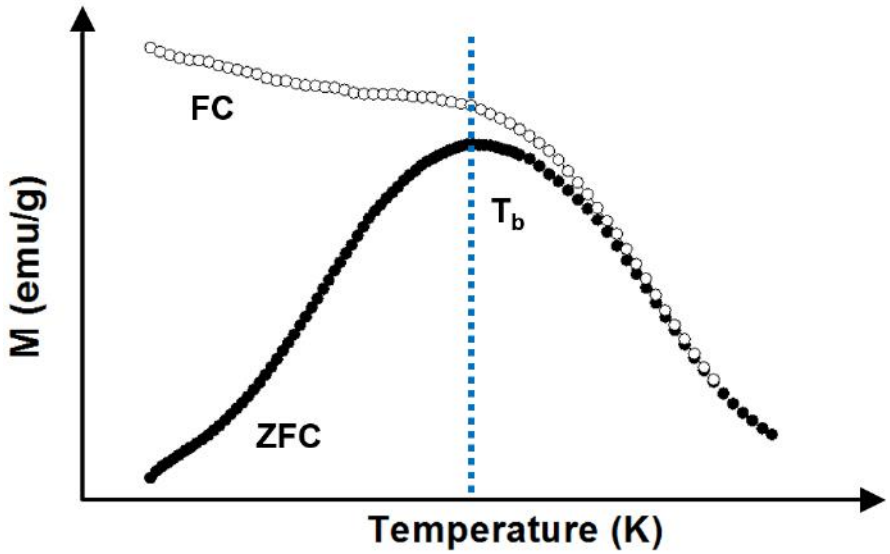

Figure 1.5. Magnetization as a function of temperature measured for ZFC and FC for superparamagnetic nanoparticles.

1.5 Oxygen Evolution Electrocatalysis

Due to increasing global energy demand and the climate change impact of CO_2 emission from traditional energy resources, it is essential to find an abundant and renewable energy system to supplement (or supplant) current resources. Splitting water utilizing electricity or visible light is a promising and appealing pathway because water is a clean and renewable energy source. Water splitting (OER, **Equation 1.2**) is composed of two half reactions: the oxygen evolution reaction (OER, **Equation 1.3**) and the hydrogen evolution reaction (HER, **Equation 1.4**).

$$2H_2O \rightarrow O_2 + 2H_2 \qquad \textbf{Equation 1.2}$$

$$2H_2O \rightarrow O_2 + 4H^+ + 4e^- \qquad \textbf{Equation 1.3}$$

$$2H^+ + 2e^- \rightarrow H_2 \qquad \textbf{Equation 1.4}$$

The Oxygen evolution reaction is critical in the water splitting process to create clean H_2 fuel. It is the first step in the overall water splitting reaction and has a high activation barrier, requiring the transfer of four electrons and four protons. In order to improve the efficiency of OER, electrocatalysts can be used. Ruthenium and iridium oxides are well-known catalysts, but their widespread application in industry has been limited by their scarcity in nature. Recently, the synthesis of novel catalyst materials composed of inexpensive, earth-abundant, yet comparatively active metals (e.g., transition metal based oxides and phosphates) have been extensively explored for large-scale OER applications.

1.6 Hydrogen Evolution Photocatalysis

Converting solar energy into chemically stored energy through photosynthesis is another effective method to generate renewable energy. A general strategy to

produce H_2 fuel via photocatalytic water splitting is to use solar energy for the water oxidation half-reaction to O_2 and the proton reduction half-reaction to H_2. For the hydrogen evolution reaction (HER), a co-catalyst is usually combined with a photosensitizer to construct a multi-component photocatalytic system. An electron source is usually needed in order to only study the reductive half-reaction, the focus of the present investigation. A general scheme for photocatalytic HER is shown in **Scheme 1.1**. The first step is absorption of photons. A photosensitizer is usually a semiconductor, in which electrons and holes can be generated at the conduction band and valence band, respectively, if the energy of incident light is larger than the band gap. The second step is charge separation and migration. In this step, the photogenerated electrons and holes can migrate to the active sites on surface and be utilized for surface chemical reactions (the third step). This process can be enhanced by decreasing electron hole recombination possibility through shortening migration distance or lowering the number of defects. However, if the photosensitizer does not have enough active sites on the surface, the photogenerated electrons and holes will recombine with each other and lower catalysis efficiency. Therefore, a co-catalyst is usually loaded on the surface of the photosensitizer to increase the active sites. Finally, the electrons can reduce protons in the water to form hydrogen and the holes can oxidize electron donors or hole scavengers such as alcohol or sulfide ion.

Scheme 1.1. Main process for photocatalytic hydrogen evolution half reaction.

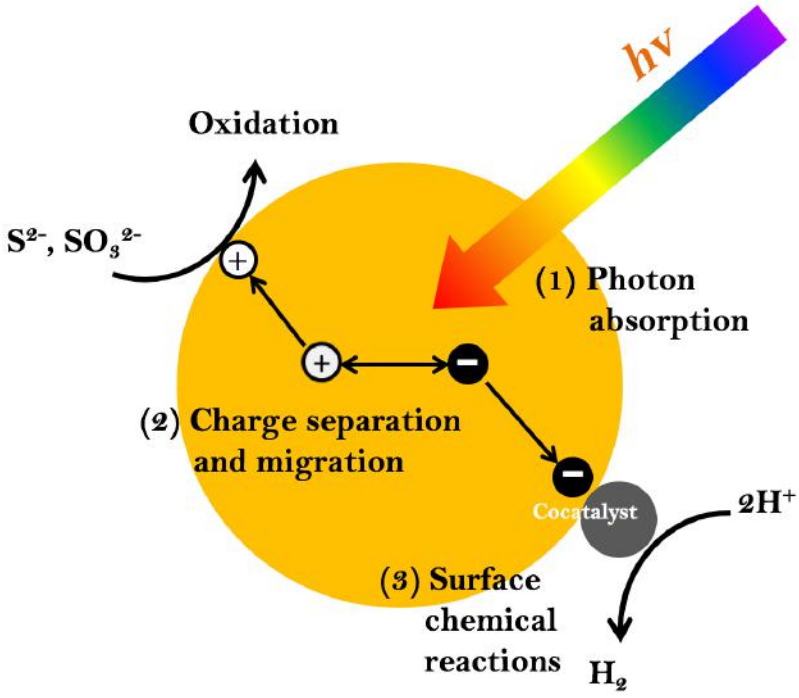

The loading of co-catalysts onto the photosensitizer can both boost the photoexcited electron–hole pair separation and reduce the activation potentials for HER, which results in the enhancement of the photocatalytic activities. As for the OER electro-catalyst, the reported cocatalysts are normally precious metals, such as Ru or Pt, which limits their practical application due to their scarcity and high cost. Efficient catalysts made of earth-abundant materials are desirable.

1.7 Thesis Statement

In order to meet growing global energy demand and reduce CO_2 emission from traditional energy resources, great efforts have been made to develop new systems that produce clean energy or utilize energy more efficiently. Photocatalytic evolution of hydrogen from water utilizing visible light is a promising and appealing pathway because water is a clean and renewable energy source. Magnetic

refrigeration, on the other hand, is a cooling technology based on the magnetocaloric effect that consumes 30% less energy than traditional gas-compression refrigeration and requires no refrigerant, eliminating emissions of refrigerant gases and associated environmental consequence.

1.7.1 Traditional Materials for Water Splitting and Magnetic Refrigeration

Ruthenium and iridium oxides are well-known water splitting catalysts.[42, 43] Nevertheless, the scarcity of Ru and Ir pose serious limitations to the widespread adoption of water splitting as a green approach to renewable energy. On the other hand, gadolinium and gadolinium-based salts (e.g., $Gd_5(Si_2Ge_2)$) are commonly used in magnetic refrigeration due to their large magnetic entropy. However, commercial use is limited due to the high cost of Gd. Therefore, great efforts have been spent on developing potential candidate materials composed of stable, Earth-abundant metals for these applications.

1.7.2 New Materials and the Motivation for Their Study

Magnetocaloric materials based on magnetic 3d elements (Mn, Fe, Co, Ni) are much less expensive than those based on rare earth elements and have drawn increasing attention. Investigations have been especially focused on Mn based materials because of the high atomic moment that Mn can achieve (up to 4 μ_B per Mn atom).[44] Also, inspired by the oxygen-evolving center of Photosystem II, manganese-based materials have garnered considerable attention for the oxygen evolution reaction, various works has been reported using manganese oxide and phosphate as water oxidation catalysts.[45-49]

1.7.3 Transition Metal Phosphides for Water Splitting and Magnetic Refrigeration

Transition metal phosphides exhibit a wide range of unique magnetic, redox and catalytic properties. The $Fe_{2-x}M_xP$ (M = Co, Mn) bulk materials have been widely studied as potential functional magnetocaloric materials.[50-53] The magnetic properties can be altered from paramagnetic Co_2P to ferromagnetic $Fe_{2-x}Co_xP$ with a tunable Curie point close to or above room temperature,[54] which makes these materials potentially suitable for magnetic imaging, therapies, refrigeration, or data storage.[55-57] More importantly, it is expected that the cycling rate in magnetic refrigeration can be further improved by preparing these materials on the nanoscale due to the reduced thermal hysteresis.[58] On the other hand, transition metal phosphide nanoparticles are also emerging as a new class of water splitting catalysts with reports of high activity in binary metal phosphides such as Ni_2P, Co_2P, and CoP. The OER and HER catalytic activities of metal phosphide materials can also be further improved by introduction of a second metal into binary metal phosphide systems. Recently, the ternary metal phosphides CoFeP, NiCoP, and NiFeP have shown improved OER activity over the binary phases (Co_2P, Fe_2P or Ni_2P) attributed to synergism between the two metals.

Despite their promise, comparatively little research has been done on ternary (relative to binary) nanoparticles of metal phosphides. There are two major challenges in the synthesis of ternary phosphide nanoparticles: the first is the possibility of phase segregation due to the different reactivities of the two metal precursors and the second is the difficulty in controlling the stoichiometric phases

of the final product because of the various oxidation states that the transition metals can adopt.

1.7.4 Goals and Dissertation Outline

This dissertation research was focused on four major goals. (1) The first goal was to study the effect of synthetic levers in metal phosphide nanoparticles formation and employ these levers to enable the control over compositions, morphology, and size of different ternary transition metal (Mn, Fe, Co) phosphides. (2) The second goal was to evaluate the composition-dependent magnetic properties of these ternary phosphide nanoparticles. (3) The third goal was to evaluate the composition-dependent catalytic properties of these ternary phosphide nanoparticles toward water oxidation and evaluate the synergistic effects between different metals. (4) The last goal was to combine metal phosphide nanomaterials with light absorbers to achieve efficient photocatalytic hydrogen evolution reaction (HER).

The dissertation is laid out as follows: **Chapter 2** presents a detailed description of the synthetic and characterization techniques used in this dissertation research. **Chapter 3** discusses the role of synthetic levers on nickel phosphide nanoparticle formation. **Chapter 4** describes the synthesis and characterization of discrete $Co_{2-x}Fe_xP$ nanoparticles and their magnetic properties. **Chapter 5** and **Chapter 6** describe the synthesis and characterization of $M_{2-x}Mn_xP$ nanoparticles (M = Co, Fe, respectively) and their catalytic properties toward electro-catalytic water oxidation. **Chapter 7** describes the formation of Ni_2P-CdS hybrid aerogels and the evaluation of their activity towards the photo-catalytic hydrogen evolution reaction.

Finally, **Chapter 8** summarizes our work and proposes further research directions.

Portions of the text in this chapter were reprinted with permission from: Chemistry of Materials, 2017, 29, 3048-3054, Chemistry of Materials, 2016, 28, 3920-3927, Journal of the American Chemical Society, 2016, 138, 4006-4009, and Inorganic Chemistry, 2015, 54, 7968-7975.

CHAPTER 2. MATERIAL CHARACTERIZATION TECHNIQUES

Metal phosphide (Ni_2P, Ni_5P_4, NiP_2, $Co_xFe_{2-x}P$, $Co_{2-x}Mn_xP$, $Fe_{2-x}Mn_xP$) and chalcogenide (CdS) nanomaterials were synthesized using the solution-phase arrested-precipitation method under an inert gas (argon) atmosphere. The materials were characterized using Powder X-Ray Diffraction (PXRD), Transmission Electron Microscopy (TEM), Energy Dispersive Spectroscopy (EDS), Scanning Transmission Electron Microscope (STEM), X-Ray Photoelectron Spectroscopy (XPS), Inductively Coupled Plasma-Mass Spectrometry (ICP-MS), Infrared Spectroscopy (IR) and Cyclic Voltammetry (CV). This chapter includes a detailed description of the synthetic and characterization techniques used in this dissertation research.

2.1 Materials

2.2.1 Metal Precursors

Nickel acetylacetonate ($Ni(acac)_2$, 95%) and bis(1,5-cyclooctadiene) nickel (0) ($Ni(COD)_2$, 98%) were purchased from Alfa Aesar. Nickel(II) acetate tetrahydrate ($Ni(OAc)_2•4H_2O$, 99%), Iron pentacarbonyl ($Fe(CO)_5$, 99.999%), dicobalt octacarbonyl ($Co_2(CO)_8$, >90%), dimanganesedecacarbonyl ($Mn_2(CO)_{10}$, 98%), and ruthenium oxide (RuO_2, 99.9%) were purchased from Sigma-Aldrich. Cadmium oxide (99.999%) was purchased from Strem Chemicals. $Co_2(CO)_8$ was stored in a refrigerator maintained at -20 °C in a glovebox.

2.2.2 Solvents

Tri-n-octylphosphine (TOP, 97%) was purchased from STREM. n-octyl ether (OE) was purchased from TCI America. Oleylamine (OAm, C18 content 80−90%)

was purchased from ACROS. Bis(trimethylsilyl)sulfide (TMS), trioctylphosphine oxide (TOPO, 90%), tetranitromethane (TNM), 11-mercaptoundecanoic acid 95% (MUA), 1-tetradecylphosphonic acid (TDPA, 98%), tetramethylammonium hydroxide pentahydrate (TMAH, 97%), 4-fluorothiopheno (98%), 1-Octadecene (90% tech.) and isopropanol (99.5%) were purchased from Sigma Aldrich. Chloroform and hexane (Certified ACS grade) were purchased from Fisher Scientific. Ethanol (200 proof) was purchased from Decon Laboratories. Toluene, methanol, acetone and ethyl acetate were purchased from Mallinckrodt. Nafion (5%, LQ-1105) was purchased from Ion Power. Ultrapure water was used in all the manipulations (resistivity = 18.1 $M\Omega.cm^{-1}$). TOPO was distilled before use; all other chemicals were used as received.

2.2 Experimental Techniques

2.2.1 Schlenk Line Techniques

Due to the air-sensitive nature of the chemicals or intermediates involved in the reactions, all nanomaterials in this dissertation were synthesized in solution phase using Schlenk line techniques. A Schlenk line is usually composed of two manifolds. One is connected to a vacuum pump by a cold trap, which can prevent solvents or chemical vapors from contaminating the pump, to create a vacuum. The other one is connected to an inert gas supply (Ar, N_2, etc.) to create an inert atmosphere. Typically, the air-sensitive materials are placed into a Schlenk flask inside a glove box, which can provide an inert atmosphere. The Schlenk flask is then transferred to a fume hood and connected to Schlenk line. A heating mantle

connected to a programmable temperature controller is usually used as a heating source.

2.2.2 Tube Furnace

In some cases, a tube furnace, which is an electric heating device, is needed to perform an after-synthesis conversion or purification on as-prepared nanoparticles. A tube furnace consists of a quartz tube surrounded by heating coils that are embedded in a thermally insulating matrix. The temperature can be monitored and controlled by a thermocouple and a temperature controller, respectively. The temperature controller can be programmed to control the ramping rate and soaking time. A combustion boat is usually used to contain samples inside the tube. The tube can be connected to one or more gas resources, such as argon, hydrogen, or nitrogen, and flow controllers are used to control the flow rate of different gases. This allows the sample to be treated under the desired atmosphere. Multiple boats containing different chemicals can be added at the same time to achieve chemical conversion. For example, NiO nanoparticles (in one boat) can be converted into Ni_2P by NaH_2PO_2 (in another boat) under active flow of 5% H_2/Ar at 400 °C for 1 hour. In this dissertation, a tube furnace was used to remove surface ligands on FeMnP nanorods (see details in **Chapter 6**).

2.3 Characterization Techniques

2.3.1 Powder X-Ray Diffraction

X-rays are produced as shown in **Figure 2.1**. First, a heated tungsten filament provides a continuous electron beam. Then the electrons strike a target (normally

Cu) on the anode after acceleration by a potential difference (30 - 60 kV) from which X-rays are emitted.

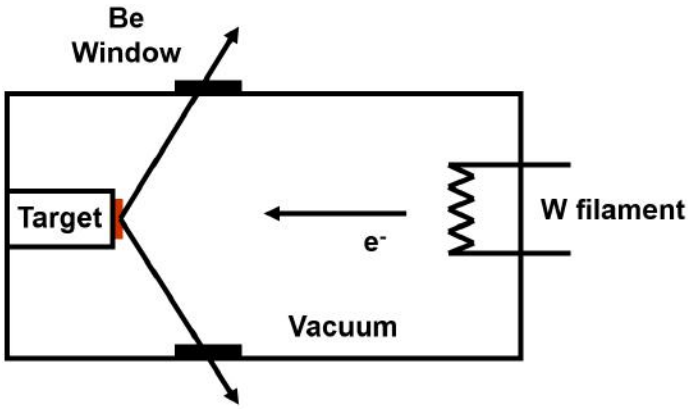

Figure 2.1. Schematic illustration of a filament X-ray tube.

As the incident electrons have been accelerated, they have sufficient energy and will ionize some 1s (K shell) electrons of Cu. As shown in **Figure 2.2**, the ionization creates a vacant hole in the K shell and an electron in an outer orbital (2p or 3p) will transit back to occupy the vacancy, releasing the energy that appears as X-radiation. The released energy has fixed values depending on which orbital the electron transited from. For Cu, the 2p to 1s transition is called Kα, which has a wavelength of 1.5418 Å, and the 3p to 1s is called Kβ with a wavelength of 1.3922 Å. The Kα transition occurs more than other transitions, so the Kα radiation is more intense and is typically used in diffraction experiments. As the electrons in the 2p orbital have two spin states ($2p_{1/2}$ and $2p_{3/2}$) with slightly different energies, the Kα transition is a doublet, $K\alpha_1$=1.54051 Å and $K\alpha_2$=1.54433 Å. Kβ radiation can be removed by applying a Ni filter, because the energy required to ionize the 1s electrons of Ni corresponds to 1.488 Å, which is higher than 1.3922 Å (Kα of Cu) but lower than 1.5418 Å (Kβ of Cu).

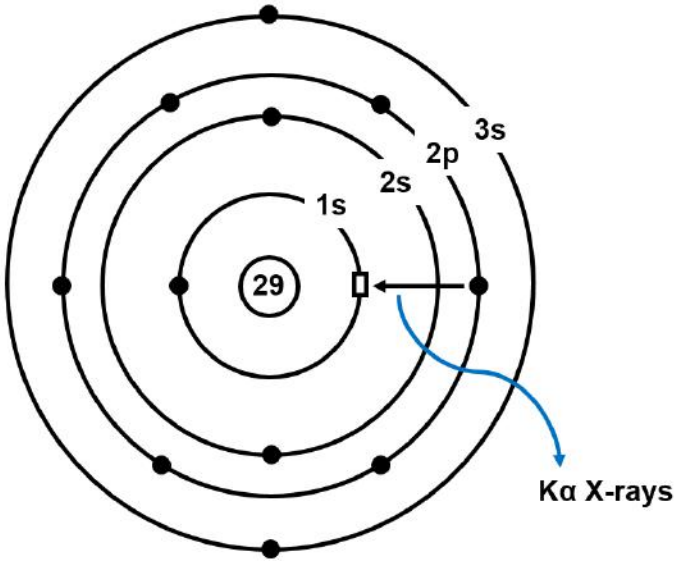

Figure 2.2. Illustration of Cu Kα X-ray generation.

When a wave is scattered by a periodic array with long rage order, it will produce constructive and destructive interference at specific angles resulting in diffraction. A crystalline solid is a material that has a highly-ordered structure with a distance between atoms (2-3 Å) similar to the wavelength of X-rays (~ 1 Å). Therefore, X-ray diffraction spectra can be used to elucidate the atomic arrangement of materials.

Bragg's Law can be used to illustrate X-ray diffraction by crystals. Two X-ray beams, a and b, interact with two adjacent atoms on two parallel planes that are separated by a distance d (**Figure 2.3**). Portions of the X-rays are reflected off the plane with an angle same as the incident angle (θ). However, the beam bb' travels an extra distance of zxy (**Equation 2.1**) than the beam aa'. In order to achieve constructive interference between two beams, the distance xyz must equal an integral number of wavelengths (**Equation 2.2**, Bragg's Law).

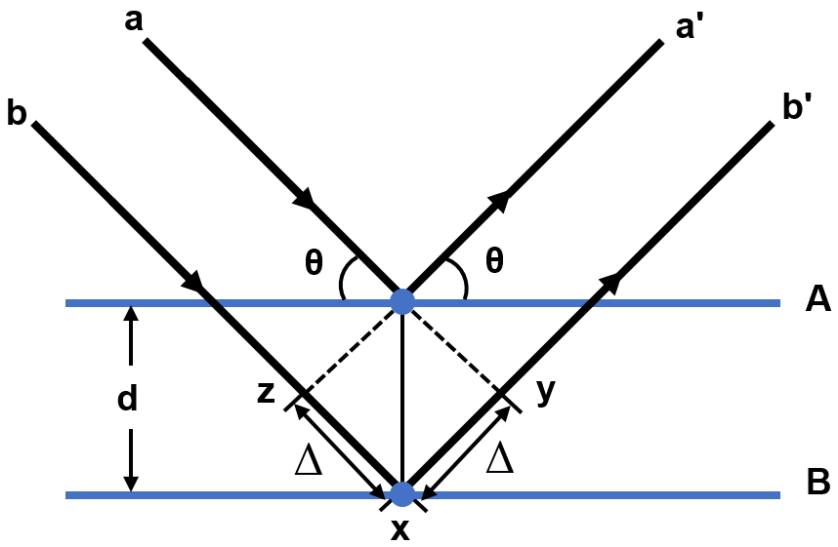

Figure 2.3. Illustration of Bragg's law (adapted from West).[59]

$$zxy = 2\Delta = 2d\sin\theta \qquad \textbf{Equation 2.1}$$

$$zxy = 2\Delta = 2d\sin\theta = n\lambda \ (n = 1, 2, 3, \ldots n) \qquad \textbf{Equation 2.2}$$

Therefore, by measuring the Bragg angle θ, the d-spacing can be obtained and used to determine the size and shape of the unit cell.

The principle of the powder X-ray diffraction experiment is shown in **Figure 2.4.** A finely powdered sample should have crystals randomly arranged in all orientations. Therefore, for each set of planes at least some crystals must be oriented at the Bragg angle relative to the incident beam. When the monochromatic X-rays hit the sample, diffraction occurs and the diffracted beams are detected by the detector.

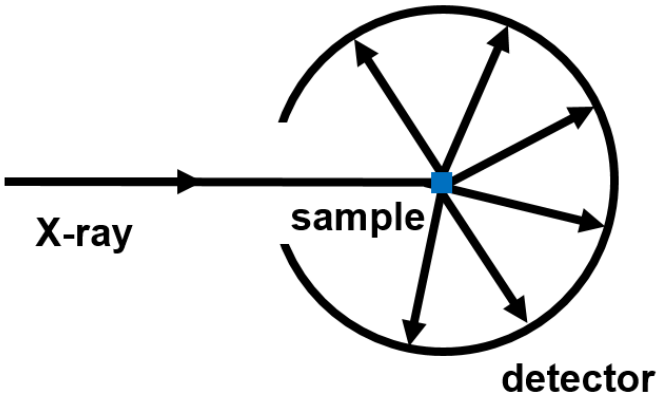

Figure 2.4. Illustration of diffraction from a powdered sample (adapted from West).[59]

A typical PXRD pattern is shown in **Figure 2.5**. Peaks at different θ angles correspond to different crystal planes with different d-spacings. By matching the experimental pattern with reference patterns, the structure of the sample can be determined. Broad peaks are normally observed in PXRD patterns of nanoparticles due to the limited number of crystalline planes, which leads to insufficient destructive interferences near the Bragg angle. Additionally, for anisotropic materials that prefer to grow along certain directions, the peaks corresponding to these directions are narrow and more intense than other peaks, reflecting the higher number of diffracting planes.

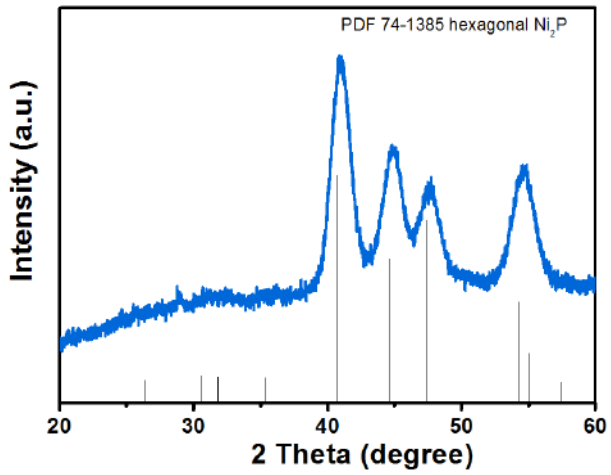

Figure 2.5. PXRD pattern of Ni_2P nanoparticles.

The breadth of the peaks can be used to calculate the crystallite size (t) using the Scherrer equation (**Equation 2.3**), in which λ is the X-ray wavelength, k is the shape factor (0.9 for spherical particles), β is the full width half maximum of the peak (FWHM), and θ is the Bragg angle.

$$t = k\lambda/\beta\cos\theta \qquad \textbf{Equation 2.3}$$

The ionization energy of 1s electrons for Co corresponds to 1.6081 Å, so 1s electrons of Co can be knocked out by the X-ray generated by a Cu anode ($K\alpha_1$=1.54051 Å). An outer shell electron in Co will then refill the empty 1s vacancy and release X-ray radiation that causes a fluorescent background, lowering the signal to noise ratio. This fluorescence issue usually occurs in samples that contain Co or Fe species and can be solved by either a discriminator or using another X-ray anode material such as Mo ($K\alpha_1$=0.7093).

In this dissertation, a Bruker D2 Phaser X-ray diffractometer with Cu Kα radiation operated at 30 kV and 10 mA was used to measure all PXRD patterns. A zero-background quartz holder was used to deposit samples on and data was acquired in the 2θ range 30-70° with a step size of 0.02° at a scan rate of 1 s per

step. PXRD patterns were processed using Jade 5.0 software and compared to powder diffraction files (PDFs) from the ICDD database.

2.3.2 Transmission Electron Microscopy

When an object is too small to be observed by the naked eye, a microscope is used. A microscope usually contains one or more optical lenses that can provide an enlarged image of the sample of interest. As shown in **Equation 2.4**, the resolution of a microscope depends on the wavelength of the radiation. Therefore, due to the large wavelength of visible light (> 400 nm), the resolution of an optical microscope can only reach hundreds of nanometers, making it difficult for observing materials in nanoscale.

$$\delta = 0.61\lambda/\mu\sin\beta \qquad \textbf{Equation 2.4}$$

δ = resolution

λ = wavelength

μ = refractive index of the viewing medium

β = semi-angle of collection of the magnifying lens

Louis de Broglie first demonstrated that electrons have wave-like properties in 1925, which provided the foundation for the development of electron microscopy. Electrons have extremely small wavelengths which can be controlled by applying different voltages (**Equation 2.5**). For electron microscopy operated at a voltage of 100 kV, a resolution as high as 0.24 nm can be reached.

$$\lambda = h/(2m_0eV)^{1/2} \qquad \textbf{Equation 2.5}$$

h = Planck's constant

V = accelerating voltage

m_0 = mass of electron

Figure 2.6 shows the signals generated when a sample is bombarded with a high-energy electron beam. Among these processes, the direct beam (transmitted electrons) is primarily used in transmission electron microscopy (TEM). Other processes and their applications are listed in **Table 2.1**.

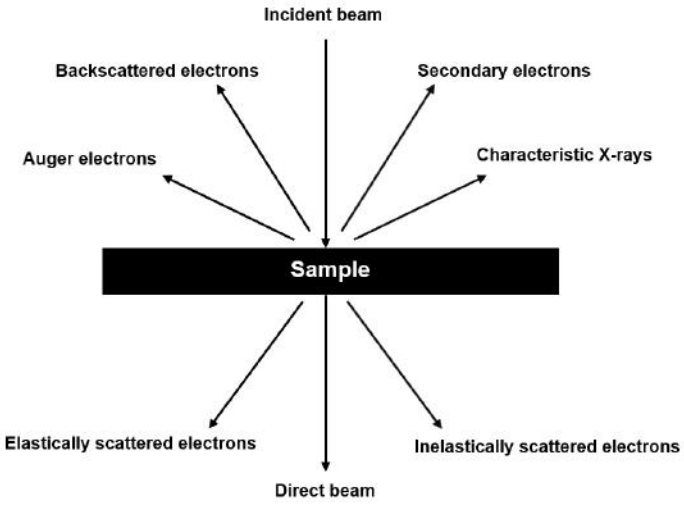

Figure 2.6. Signals generated when a sample is bombarded with a high-energy electron beam (adapted from Williams).[60]

Table 2.1. Signals generated when a sample is bombarded with a high-energy electron beam and their applications for materials characterization.

Type of signal	Applications
Auger electrons	Auger Electron Spectroscopy
Backscattered electrons	Scanning Electron Microscopy
Secondary electrons	Scanning Electron Microscopy
Characteristic X-rays	Energy Dispersive Spectroscopy
Inelastically scattered electrons	Electron Diffraction
Elastically scattered electrons	Scanning Transmission Electron Microscopy / Electron Energy Loss spectroscopy

Figure 2.7 shows a comparison between light microscopy and TEM. TEM uses electron beams, which are produced by an electron gun through the application of a high voltage (100 kV to 400 kV), instead of visible light for forming highly magnified images. Similar to light microscopy, condenser lenses are used in order to control the intensity and angular aperture of the produced electron beam before interacting with the sample. Objective lenses focus the beam coming through the specimen while the intermediate projective lenses expand the beam on the viewing screen. However, these lenses are all made of electromagnets instead of glass, which provide the ability to adjust the pathway of electron beams due to the negative charge on electrons. The final image of the sample can be observed on a fluorescent screen and captured by a camera.

In nanotechnology, electron microscopy is an important characterization tool used to analyze size, morphology, chemical composition, and crystallinity of materials. In this dissertation research, TEM, energy dispersive spectroscopy (EDS), and scanning transmission microscopy (STEM) were mainly used and will be discussed in detail in **Sections 2.3.2, 2.3.3,** and **2.3.4**.

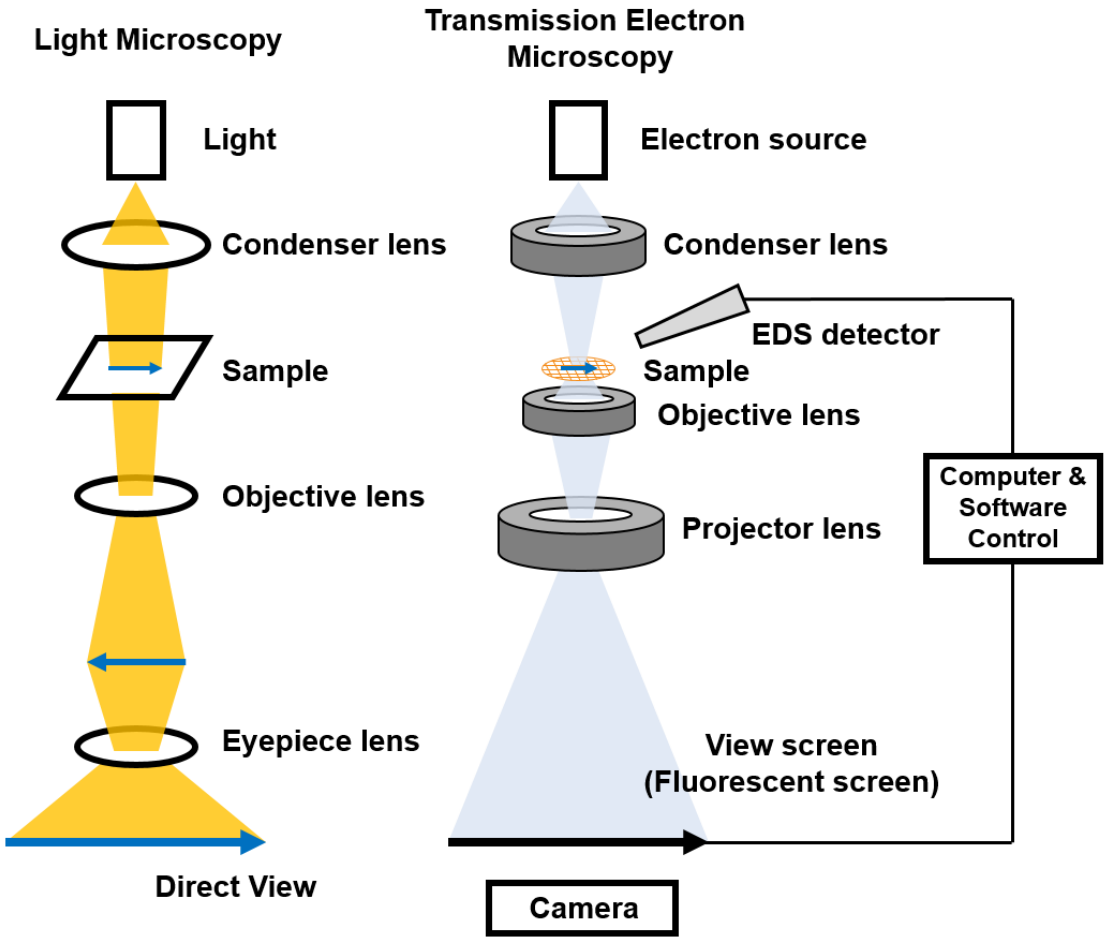

Figure 2.7. Illustration of a comparison between light microscopy and transmission electron microscopy.

In this dissertation research, the nanoparticles are supported on a copper grid coated with a thin carbon film. Since TEM imaging is based on the transmitted radiation, the contrast of the image depends on the atomic number of the elements and the thickness of the sample. To obtain a high-quality image, the sample deposited should be uniform and sufficiently thin (<1000 Å).

TEM has two basic imaging modes: dark field mode and bright field mode. In the bright field mode (**Figure 2.8a**), the transmitted electrons get weakened by interacting with the sample. Thicker areas or regions of higher atomic number block more electrons and result in a dark area in the final image. While thinner

areas or regions with lower atomic number will appear bright. The background is bright because no electrons were blocked by the sample. An objective aperture blocks the diffracted beams and only the direct beam reaches the screen. In the dark field mode (**Figure 2.8b**) only the diffracted beams reach the screen and the direct beam is blocked by an objective aperture. In these images the crystalline region of the material appears bright in a dark background. Normally the bright field mode is used to observe the morphology and size of samples whicle the dark field mode is used to acquire the information regarding crystals and defects.

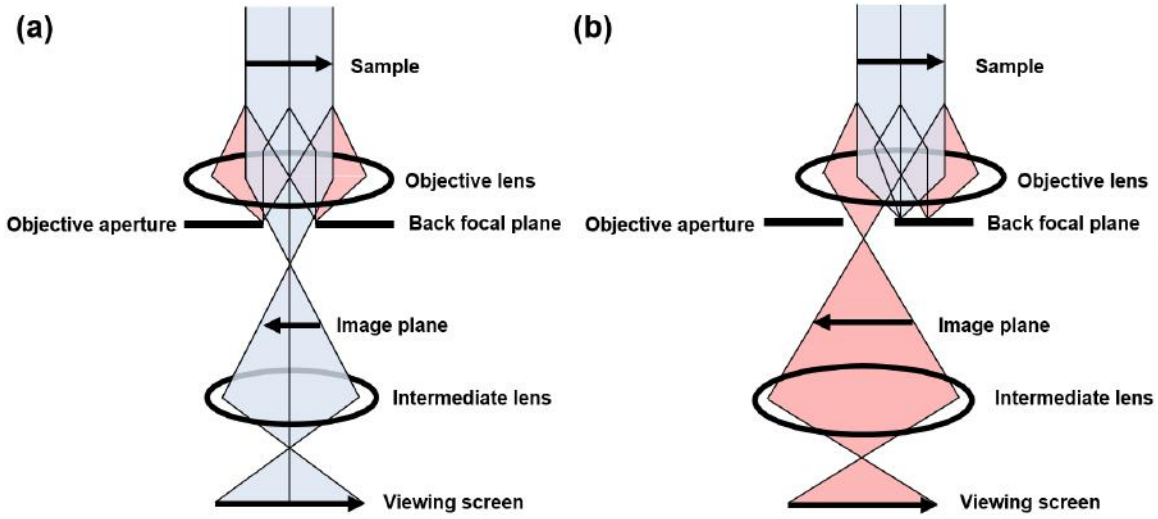

Figure 2.8. Basic imaging modes of TEM (a) bright field mode and (b) dark field mode (adapted from Williams).[60]

In this dissertation, TEM was performed using a JEOL 2010 electron microscope operated at a voltage of 200 kV and a beam current of 107-108 μA with a coupled EDS detector (EDAX Inc.). The images were captured using Amtv600 software provided by the Advanced Microscopy Techniques Corporation. Samples for TEM analysis were prepared by depositing a drop of chloroform

nanoparticle dispersion onto a carbon-coated 200 mesh Cu grid, followed by air-drying.

2.3.3 Energy Dispersive Spectroscopy (EDS)

As shown in **Figure 2.5**, X-rays can be generated when a sample is bombarded with high energy electrons. The energy of the generated X-rays is characteristic of the bombarded element due to the unique electron configuration, as discussed in **section 2.3.1**. Therefore, the energies and intensities of generated X-rays can be used to identify elements and their relative concentrations. As shown in **Figure 2.6**, an EDS unit is usually coupled with a TEM or a SEM.

The typical spectrum is a plot of X-ray counts (intensity) vs. energy as shown by the representative plot of CoMnP nanoparticles in **Figure 2.9**. EDS is a semi-quantitative method. Normally, only peaks which have high signal to noise ratio (> 3) should be considered for identification while ones exhibiting no overlap with other peaks can be used for quantification.

In this dissertation, EDS data was collected using an EDS detector (EDAX Inc.) coupled to the JEOL 2010 TEM instrument.

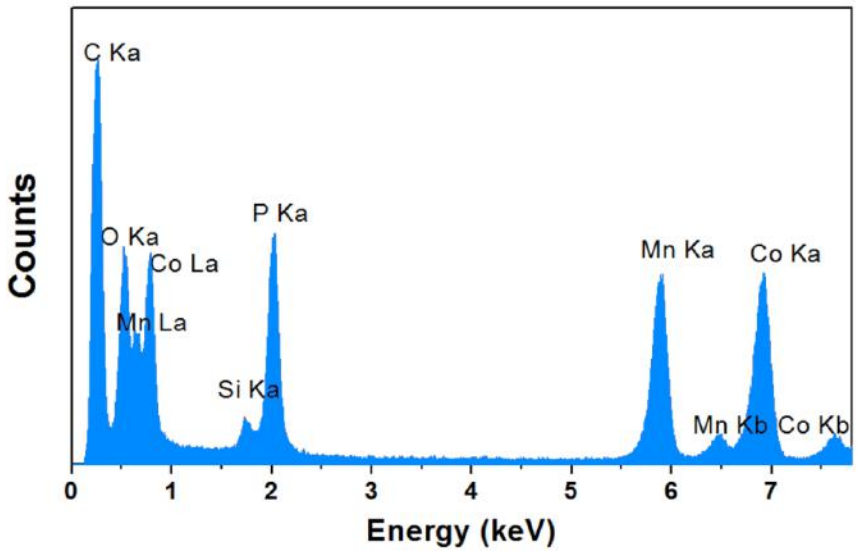

Figure 2.9. EDS spectrum of a CoMnP nanoparticle sample.

2.3.4 Scanning Transmission Electron Microscopy

Scanning transmission electron microscopy (STEM) is one type of TEM, but instead of passing electron beams through a sample and forming an image as in TEM, STEM uses a finely focused beam of electrons to scan through a sample in a raster pattern. STEM can be equipped with different detectors to provide various analytical techniques such as annular dark-field imaging, EDS elemental mapping, or electron energy loss spectroscopy (EELS), which are vital to study the homogeneity and structure at atomic level of a sample.

In this dissertation, STEM and EDS elemental maps were collected using an FEI Titan 80−300 scanning transmission electron microscope (STEM) with ChemiSTEM technology operated at 200 kV. This instrument is housed at North Carolina State University and data were acquired by Y. Liu.

2.3.5 X-ray Photoelectron Spectroscopy

X-ray photoelectron spectroscopy (XPS) is a technique that measures the chemical environment and oxidation states of elements on the surface (0-10 nm)

of a material. This technique uses X-rays, normally produced by a Mg or Al source, to irradiate the sample of interest. Under irradiation with X-rays, electrons at core levels will adsorb the photon energy and be ejected. The kinetic energy (E_K) and number of ejected electrons are measured by the instrument (**Figure 2.10**). **Equation 2.5** shows the relationship between E_K and the binding energy (E_B) of an ejected electron, with E_P and ϕ representing the photon energy and the work function of the instrument, respectively.

$$E_B = E_P - (E_K + \phi) \qquad \textbf{Equation 2.5}$$

As E_P depends on the metal source used for X-ray ($E_{P\text{-}Mg\text{-}K\alpha}$ = 1253.6 eV and $E_{P\text{-}Al\text{-}K\alpha}$ = 1486.6 eV) and E_K is measured by the instrument, E_B can be calculated by **Equation 2.5**. The binding energy of the electron ejected is element-specific and varies with the electron configuration of the element, so it can be used to identify the element and its oxidation state or binding environment.

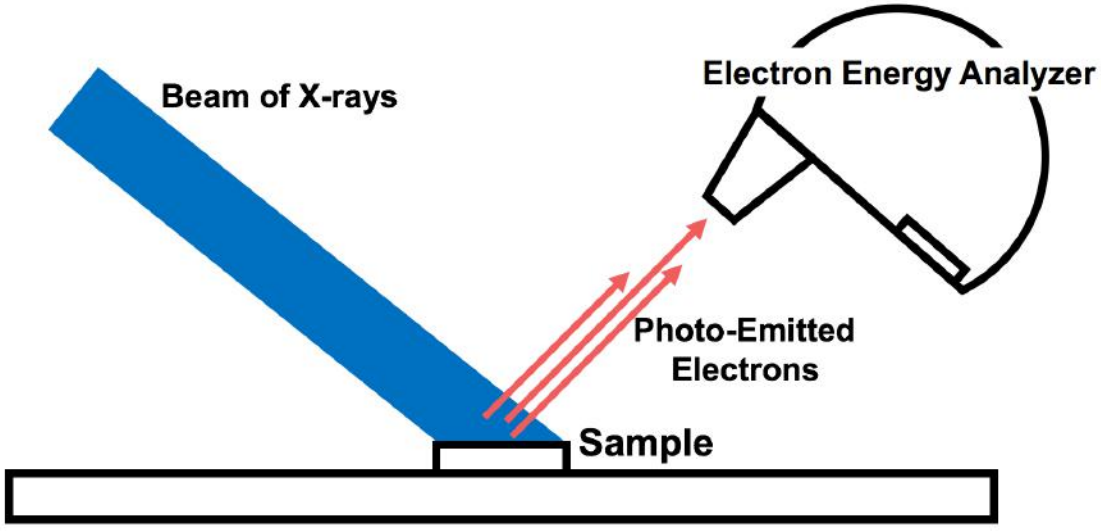

Figure 2.10. Schematic illustration of a XPS system.

In this dissertation study, a Kratos Axis Ultra XPS was used to carry out XPS measurements. Binding energies (BE) were determined using the C 1s peak at

284.8 eV as a charge reference. XPSpeak software was used to analyze the high-resolution spectra.

2.3.6 Inductively Coupled Plasma-Mass Spectrometry

As mentioned in **Section 2.3.3**, EDS is a semi-quantitative method and was used to determine only the approximate composition of the materials. Inductively coupled plasma-mass spectrometry (ICP-MS) is an analytical technique consisting of an ICP coupled to a mass spectrometer. It has low detection limits (parts per billion, ppb), high accuracy, high selectivity, and low interference between different elements, which makes it an ideal technique for elemental analysis. In the operation of ICP-MS, an Ar plasma is first formed inside the instrument. The sample is then exposed to the ICP torch as an aerosol to enable a conversion into gaseous atoms that are further ionized towards the end of the plasma. Ions that are generated are then sorted within the mass spectrometer based on the mass-to-charge ratio prior to reaching the detector.

In this dissertation, an Agilent 7700 ICP-MS instrument was used to determine the elemental compositions. The samples were digested in concentrated nitric acid and diluted with ultra-pure water. A series of external standards were used for calibration over the relevant concentration range.

2.3.7 Infrared Spectroscopy

Infrared (IR) spectroscopy is a tool mainly used to detect the interaction of infrared radiation with a molecule. It is normally used to identify functional groups by measuring the vibrational frequency of a bond, which is affected by the mode of vibration, bond strength, and mass of atoms. For an IR active vibration, the

dipole moment changes with the vibration. Typically, IR spectra are collected within a range of 4000-400 cm^{-1}.

In this dissertation, A Bruker Tensor 27 FTIR spectrometer was used to probe surface ligand groups. A powder of nanoparticles was ground with KBr to yield a uniform mixture and pressed into a transparent pellet by applying 2000 psi pressure using a Carver Hydraulic pellet press.

2.3.8 Cyclic Voltammetry

Cyclic Voltammetry (CV) is a technique that measures the electrochemical properties of the sample of interest. Normally, a CV is performed by cycling the potential and measuring the resulting current in a standard three electrode system. A standard three electrode system consists of a working electrode, reference electrode, and counter electrode (**Figure 2.11**). The working electrode, which directly touches the analyte, is normally used to apply a potential to the analyte. The reference electrode is a half cell with a known reduction potential and acts as reference in controlling and measuring the potential applied to the working electrode. The counter electrode balances the current observed at the working electrode by passing any current needed. In this way, both potential and current can be monitored to measure the electrochemical behavior of the analyte.

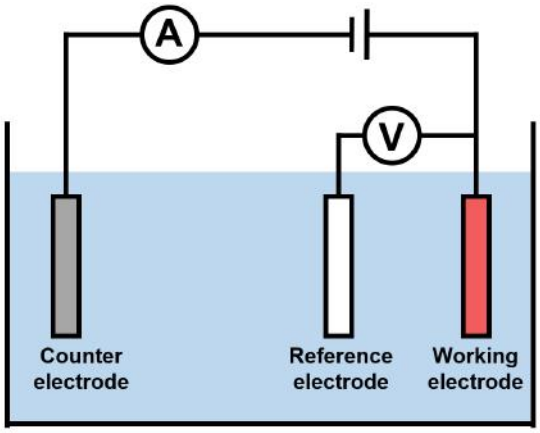

Figure 2.11. A standard three electrode system.

In this dissertation, all the cyclic voltammograms were recorded using an EC epsilon potentiostat equipped with a rotating disc electrode (RDE). In a typical experiment, a standard three electrode setup was employed using a Ag/AgCl reference electrode, Pt wire auxiliary electrode, and glassy carbon working electrode.

Portions of the text in this chapter were reprinted with permission from: Chemistry of Materials, 2017, 29, 3048-3054, Chemistry of Materials, 2016, 28, 3920-3927, Journal of the American Chemical Society, 2016, 138, 4006-4009, and Inorganic Chemistry, 2015, 54, 7968-7975.

CHAPTER 3. EFFECT OF SYNTHETIC LEVERS ON NICKEL PHOSPHIDE NANOPARTICLE FORMATION: Ni_5P_4 AND NiP_2

ABSTRACT

Due to their unique catalytic, electronic, and redox processes, Ni_5P_4 and NiP_2 nanoparticles are of interest for a wide-range of applications from the hydrogen evolution reaction to energy storage (batteries); yet synthetic approaches to these materials are limited. In the present work, a phase-control strategy enabling the arrested-precipitation synthesis of nanoparticles of Ni_5P_4 and NiP_2 as phase-pure samples using different Ni organometallic precursors and trioctylphosphine (TOP) is described. The composition and purity of the product can be tuned by changing key synthetic levers, including the Ni precursor, the oleylamine (OAm) and TOP concentrations, temperature, time and the presence or absence of a moderate temperature soak step to facilitate formation of Ni and/or Ni-P amorphous nanoparticle intermediates. Notably, the 230 °C intermediate step favors the ultimate formation of Ni_2P and hinders further phosphidation to form Ni_5P_4 or NiP_2 as phase-pure products. In the absence of this step, increasing the P/Ni ratio (13-20), reaction temperature (350-385 °C) and time (10-48 h) favors more P-rich phases, and these parameters can be adjusted to generate either Ni_5P_4 or NiP_2. The phase of the obtained particles can also be tuned between pure Ni_2P to Ni_5P_4 and NiP_2 by simply decreasing the OAm/TOP ratio and/or changing the nickel precursor (nickel acetylacetonate, nickel acetate tetrahydrate or Bis(cyclooctadiene)nickel). However, at high concentrations of OAm, the product formed is the same regardless of Ni precursor, suggesting formation of a uniform

Ni intermediate (an Ni-oleylamine complex) under these conditions that is responsible for product distribution. Intriguingly, under the extreme phosphidation conditions required to favor Ni_5P_4 and NiP_2 over Ni_2P (large excess of TOP), the 20-30 nm crystallites assemble into supraparticles with diameters of 100-500 nm. These factors are discussed in light of a comprehensive synthetic utilized to control P incorporation in nickel phosphides.

Li, D., Senevirathne, K., Aquilina, L., Brock, S. L. Inorganic Chemistry, **2015**, 54, 7968-7975. Reprinted with permission from Copyright (2015) American Chemical Society.

3.1 Introduction

Due to the wide range of unique magnetic, redox and catalytic properties exhibited by transition metal phosphides, the development of methods for their production on the nanoscale with control of size, shape and composition, is an important endeavor.[1-4] Because the magnetic and catalytic properties of transition metal phosphides depend on the size and shape (in the nano regime) as well as the composition,[5-9] it is important to establish the synthetic factors that enable access to different phase-pure transition metal phosphides. Metal-rich nickel phosphides such as Ni_2P are potent hydrotreating catalysts[1, 2, 5, 8, 10-12] while the more phosphorus-rich phases such Ni_5P_4 and NiP_2 are promising candidates for lithium ion battery electrode materials, due to their high gravimetric and volumetric capacity.[13, 14] Furthermore, all of these phases show considerable potential to be used in hydrogen evolution catalysis.[15-17] In order to be able to target desired phases on the more phosphorus-rich side of the Ni-P phase diagram, a detailed study of the parameters that govern phase formation is needed.

This chapter discusses a successful phase control strategy used for the more phosphorus-rich phases, Ni_5P_4-NiP_2. The role of the key synthetic levers on the phase-purity and morphology of the product, including the Ni precursor, the OAm and TOP concentrations, temperature, time and the explicit formation of Ni/amorphous Ni-P intermediate nanoparticles by a moderate temperature soak step are studied and a comprehensive synthetic scheme to control phosphorus incorporation in nickel phosphides prepared by arrested precipitation reaction is developed.

Early work was performed by Lance Aquilina and Keerthi Senevirathne to identify that Ni_5P_4 could be synthesized by standard arrested precipitation routes. I optimized the synthesis of Ni_5P_4 and NiP_2, elucidated the roles of synthetic parameters, and carried out all the synthesis and characterization of the materials.

3.2 Experimental

All materials used in the synthesis of nickel phosphide nanoparticles are given in Chapter 2.

3.2.1 Synthesis of Nickel Phosphide Nanoparticles

Safety warning: this procedure involves the usage of air-sensitive, flammable TOP and the generation of PH_3 as an intermediate product, all reactions should be carried out under an argon atmosphere using standard Schlenk line techniques in the fume hood following **Scheme 3.1**. The flasks were heated in mantles insulated with quartz wool and the temperature was monitored using a probe adjacent to the flask, and within the mantle.

Scheme 3.1. Synthesis of nickel phosphide nanoparticles.

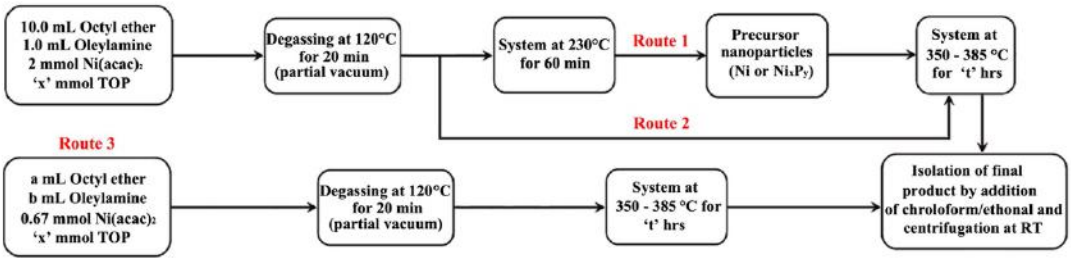

Route 1 and 2: The synthesis of Ni/Ni_xP_y precursor particles was performed by taking 0.514 g of $Ni(acac)_2$ (2.0 mmol), 12.0 - 30.0 mL (26.9 - 67.2 mmol) of TOP, 10.0 mL of octyl ether, and 1.0 mL of OAm (3.0 mmol) and heating at 230 °C for 60 min. The system temperature was then raised to 350-385 °C, kept for 1 - 24 h,

and then allowed to cool naturally to room temperature. In route 2, the intermediate 230 °C step was removed.

When $Ni(COD)_2$ or $Ni(OAc)_2{\cdot}4H_2O$ was used as metal precursor, all the reaction parameters were identical except using 0.550 g $Ni(COD)_2$ (2.0 mmol) or 0.498 g $Ni(OAc)_2{\cdot}4H_2O$ (2.0 mmol).

Route 3: A mixture of 0.172 g $Ni(acac)_2$ (0.67 mmol), 1-20 mL TOP (2.24 - 44.8 mmol) and 10 mL of a mixture of OAm and octyl ether ranging from 3.3% up to 100% OAm (1.0 – 30.0 mmol) by volume, was directly heated at 330-385 °C for 1-48 hours and then allowed to cool naturally to room temperature.

When $Ni(COD)_2$ or $Ni(OAc)_2{\cdot}4H_2O$ was used as metal precursor, all the reaction parameters were identical except using 0.183 g $Ni(COD)_2$ (0.67 mmol) or 0.166 g $Ni(OAc)_2{\cdot}4H_2O$ (0.67 b mmol).

The black precipitates from Routes 1-3 (nickel phosphide nanoparticles) were sonicated in chloroform and reprecipated by adding excess ethanol. This sonication-precipitation cycle was done at least three times to remove as much of the bound organics as possible from the system. The isolated black powder was then dried under vacuum.

3.2.2 Characterization

Transmission electron microscopy (TEM) and powder X-ray diffraction (PXRD) were operated as describe in **Chapter 2**.

3.3 Results and Discussion

At the outset, $Ni(acac)_2$ was used as the metal source and TOP as the P source to prepare nickel phosphide nanoparticles. Our previous work on nanoscale iron

phosphides clearly indicated that the choice of P/M (phosphorus/metal) precursor ratio, reaction temperature and heating time are key factors that determine the stoichiometry of the product.[6] A series of reactions were carried out following Route 1 (Scheme 1) to establish the independent effects of TOP/Ni ratio, heating temperature and reaction time. Relative to our prior work on $Ni_{12}P_5$ and Ni, we sought to use higher P/M ratios, temperatures and times in order to achieve increased phosphidation.

3.3.1 Effect of precursor ratio, temperature and time: Route 1.

Using a synthesis temperature of 370 °C and 3 mmol OAm, the ratio of P/Ni in the reaction was varied from 13.4 to 20.2 by changing the quantity of TOP (26.8 mmol to 40.4 mmol) used in the synthesis. As shown in **Figure 3.1**, when the P/Ni ratio was changed from 13.4 to 16.8, the phase of the final product changed from Ni_2P to a mixture of Ni_2P and Ni_5P_4. Further increasing the P/Ni ratio to 18.8 resulted in a mixture of Ni_2P, Ni_5P_4 and NiP_2; whereas for a P/Ni ratio of 20.2, NiP_2 was the major phase (with Ni_2P, NiP and Ni_5P_4 present as minor phases). These data suggest that higher concentration of TOP favors the incorporation of more P into the nickel phosphide nanoparticles.

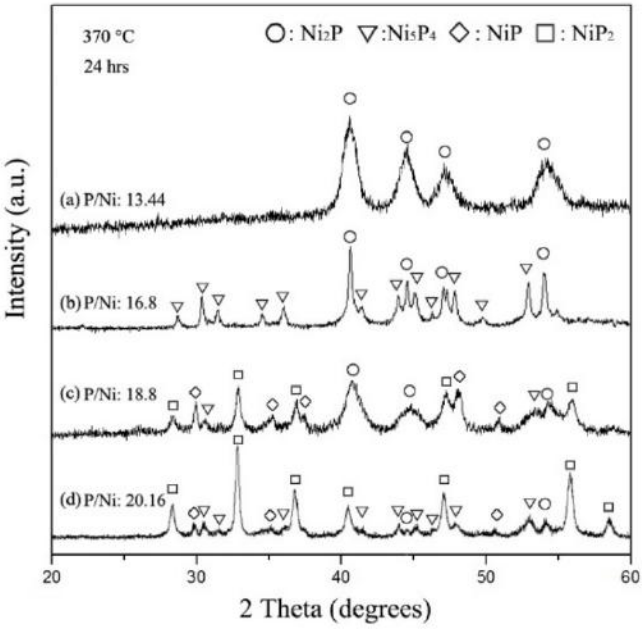

Figure 3.1. PXRD patterns of the product from Route 1 (Scheme 3.1) as a function of TOP quantity; reactions were carried out at 370 °C for 24 h with 2 mmol $Ni(acac)_2$ and 3 mmol OAm.

In order to assess how temperature affects the final phase, the intermediate P/Ni ratio (16.8) was chosen and the heating temperature was changed from 350 to 370 to 385 °C. As shown in **Figure 3.2a**, increasing temperature resulted in a shift in the product phase from Ni_2P (350 °C) to a mixture of Ni_2P, Ni_5P_4 (370 °C) and ultimately to a mixture of Ni_2P, Ni_5P_4, NiP_2 (385 °). Thus, the increase of heating temperature correlates with the appearance of more P-rich phases; presumably, by increasing the concentration of active phosphorus as well as the kinetics of P incorporation.

Finally, in order to assess how reaction time effects the final phase, the reaction time was varied from 10 to 24 to 48 h, holding the P/Ni ratio and heating temperature constant (16.8 and 370 °C, respectively). As shown in **Figure 3.2b**, the phase of the products changed from Ni_2P at 10 h to a mixture of Ni_2P and Ni_5P_4

at 24 h, and a mixture of Ni_2P, Ni_5P_4, NiP, NiP_2 at 48 h demonstrating that longer reaction times also facilitate P incorporation.

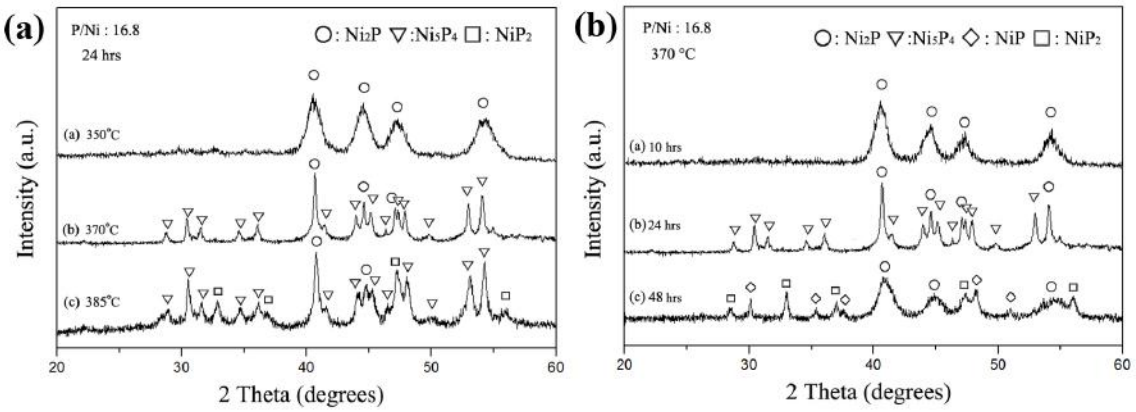

Figure 3.2. PXRD patterns of the products from Route 1 (Scheme 3.1) with 2 mmol $Ni(acac)_2$ and 33.6 mmol TOP (P/Ni=16.8): (a) As a function of heating temperature for 24 h; (b) as a function of heating time at 370°C.

The results clearly indicate that the higher P/Ni ratio, higher temperature, and the longer heating time favor the formation of P - rich phases. These observations are consistent with the behavior exhibited in the $Ni_{12}P_5$ – Ni_2P case in our previous study, although in the present case the quantity of TOP used in the synthesis is much higher.[32] However, despite a clear preference towards more P-rich phases, it was impossible to obtain phase pure products of Ni_5P_4 or NiP_2 by this approach. We hypothesized that Ni_2P, once formed, may be slow to convert and focused our study on the intermediate heating step.

3.3.2 Probing the intermediate heating step.

Previous studies showed that $Ni(acac)_2$ can be reduced by OAm ($0.1 \leq Ni/OAm \leq 0.33$) to Ni nanoparticles (without TOP or with low TOP/Ni ratio ($P/Ni < 2.24$)) or amorphous Ni_xP_y nanoparticles ($P/Ni > 2.24$) at 220-240 °C.[32, 61, 62] These nanoparticles then serve as templates for the formation of crystalline nickel

phosphide nanoparticles at elevated temperatures.[32, 63-65] As shown in **Figure 3.3**, we find that intermediate amorphous Ni_xP_y particles form in as little as 3 min at 230 °C (ca. 5.1 ± 0.6 nm, **Figure 3.3**), which means that whether or not there is an intermediate 230 °C step, this fast amorphous particle formation process may always occur during temperature ramp-up. At 60 min, the material remains amorphous but the average particle size increases to 9.7 ± 1.6 nm. Intriguingly, heating for 24 hours yields crystalline Ni_2P with a crystallite size diameter of 8.5 nm (calculated by applying the Scherrer equation to the (111) reflection), superimposed over an amorphous hump. This suggests that Ni_2P may be kinetically favored at lower T (230 °C), regardless of P/Ni ratio, and might be resistant to transformation to more P-rich phases, resulting in mixed phase products.

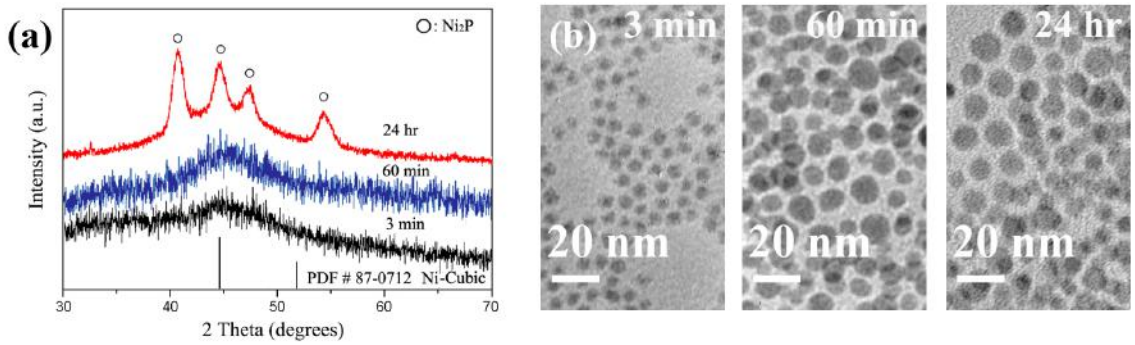

Figure 3.3. (a) PXRD patterns and (b) TEM images of intermediate Ni_xP_y particles prepared at different heating times at 230 °C (P/Ni = 16.8).

To test this premise, 0.5 mmol Ni_2P nanoparticles (74.2 mg, 10 nm, **Figure 3.4a**) were synthesized and reacted with a large excess of TOP (22.4 mmol) in 10 mL octyl ether at high temperature (380 °C) for a long reaction time (24 hours). Ni_2P was still the major phase of the final product along with some peaks attributed to Ni_5P_4 and NiP_2 determined by PXRD data (**Figure 3.4d** bottom). The former

work done by the Sanchez group has shown that Ni_2P is a favored phase on the nanoscale even at high P/Ni ratios.[63] The formation of Ni_2P in the intermediate step and the inaccessibility of the complete conversion from Ni_2P to the more P-rich nickel phosphides suggest that increasing the duration of the intermediate step may facilitate crystallization of the amorphous particles, resulting in stabilizing the formation of Ni_2P and hindering further phosphidation to achieve the more P-rich phases as single-phase products. The consequences of the extreme phosphidation conditions on the morphology are shown in **Figure 3.4b**, where the products are spherical clusters of 500 nm in diameter. High resolution TEM imaging of a selected area (**Figure 3.4c**) reveals that these clusters comprise a large amount of well crystallized 10 nm Ni_2P nanoparticles. As will be shown below, the combination of high TOP amount and high temperature favors large aggregates of discrete nanoparticles, reminiscent of supraparticles.[66]

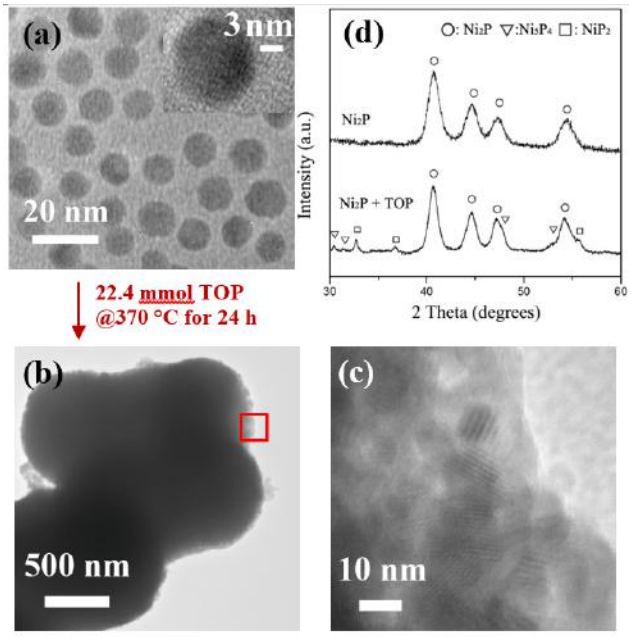

Figure 3.4. TEM images of Ni_2P nanoparticles (a) before and (b) after reaction with TOP; (c) HRTEM of a selected area in (b). (d) PXRD patterns of Ni_2P particles before (top) and after (bottom) reaction with TOP at 380°C for 24 hours.

3.3.3 Obtaining phase-pure Ni_5P_4 by Route 2.

In order to avoid Ni_2P formation at the intermediate step, the 230 °C step was eliminated as shown in Route 2 (**Scheme 3.1**). For a P/Ni ratio of 16.8, raising the reaction temperature directly to 370 °C for 24 h leads to a material wherein the detectable PXRD peaks could all be indexed to Ni_5P_4 (**Figure 3.5a**). Crystallite size calculated by applying the Scherrer equation to the (214) reflection of Ni_5P_4 nanoparticles yielded an average diameter of 25.3 nm. Transmission electron microscopy (TEM) images (**Figure 3.5b** and **c**) reveal that the Ni_5P_4 product forms as highly uniform spherical supraparticles of ca. 500 nm in diameter consisting of many small 20-30 nm nanocrystallites, similar to what was observed from forced phosphidation of Ni_2P. This phenomenon has also been observed in other systems with quite different chemistries, including Fe_3O_4, In_2O_3 and CdSe.[67-69] The

primary particles are presumed to aggregate into supraparticles in order to minimize the surface energy.

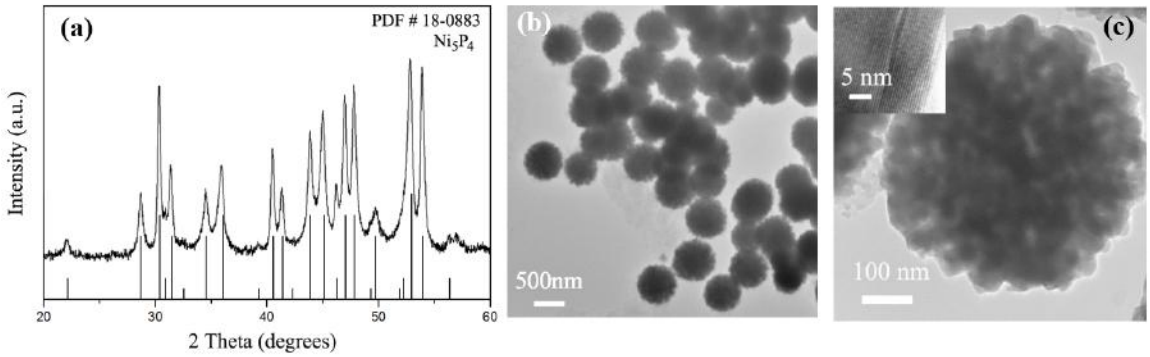

Figure 3.5. (a) PXRD pattern of Ni_5P_4 particles from Route 2. (b), (c) TEM images of Ni_5P_4 particles (inset: HRTEM showing lattice fringes)

3.3.4 Obtaining phase-pure NiP_2 by Route 2

In order to target a more P-rich phase (NiP or NiP_2), the P/Ni ratio and heating temperature were increased from 16.8 to 33.6 and 370 to 385 °C, respectively in Route 2 (without the 230 °C step). PXRD data acquired on the product is consistent with the formation of NiP_2 (**Figure 3.6**). From the Scherrer equation, the crystallite size of these NiP_2 particles is about 29.6 nm, whereas the particle size obtained from TEM micrographs is quite large (100's of nm), suggesting that particle aggregation and supraparticle formation is again operable. Intriguingly, these particles are less uniform than those obtained at 370 °C, suggesting that formation of discrete NiP_2 particles and aggregation into supraparticles may not be temporally isolated in this case.

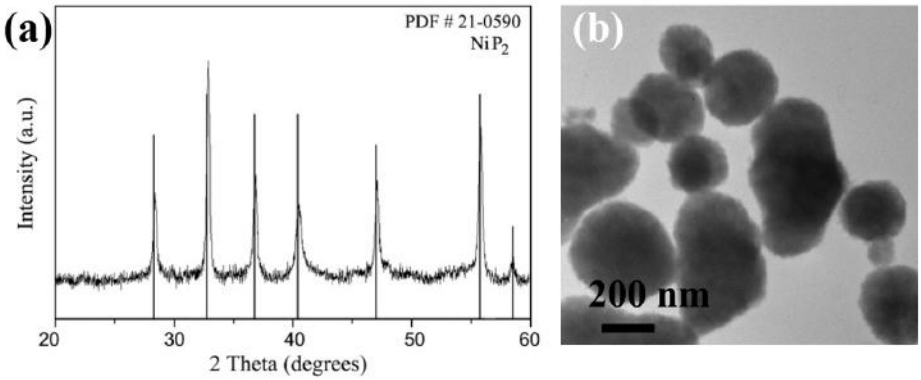

Figure 3.6. (a) PXRD patterns and (b) TEM images of NiP_2 particles prepared from Route 2.

3.3.5 Obtaining pure-phase Ni_2P by Route 2

We next tested whether the intermediate templating step was needed for routine Ni_2P particle formation and whether it has any role in dictating particle size or polydispersity. We synthesized Ni_2P nanoparticles according to both Route 1 and Route 2 with identical reagent parameters except one had the intermediate step and the other did not. There is no obvious difference between the crystallite size from PXRD or the size/morphology from TEM of the phase-pure Ni_2P nanoparticles prepared by these two routes (**Figure 3.7**). Therefore, for nanoscale nickel phosphide formation, the introduction of an explicit moderate temperature soak step to form intermediate precursor particles that template formation of the product is not necessary.

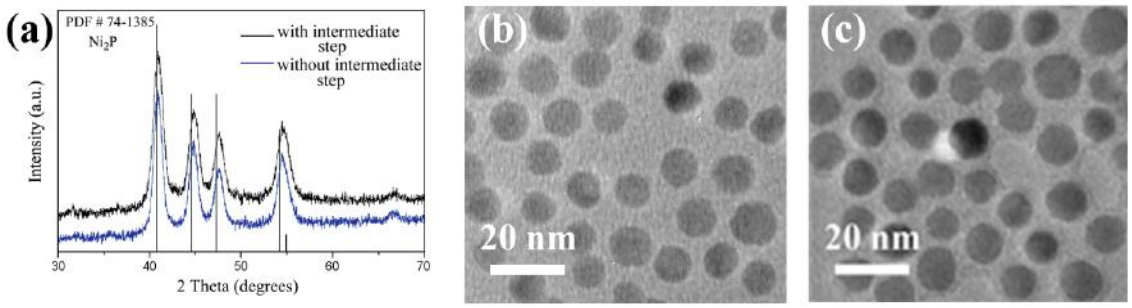

Figure 3.7. (a) PXRD patterns and (b), (c) TEM images of Ni_2P prepared with or without the 230°C intermediate step, respectively.

3.3.6 Effect of the nickel precursor on targeted phase

Based on the prior work showing the Ni precursor can affect the targeted phases, $Ni(acac)_2$, $Ni(COD)_2$ and $Ni(OAc)_2•4H_2O$ were used as Ni precursors in Route 2 targeting conditions for Ni_5P_4 formation (P/Ni ratio = 16.8, 370 °C, 24 h). As evidenced from PXRD, the final phases of the products were Ni_5P_4 ($Ni(acac)_2$), a mixture of Ni_5P_4, Ni_2P ($Ni(COD)_2$) and Ni_2P ($Ni(OAc)_2•4H_2O$) (**Figure 3.8**). We hypothesized that the precursor dependence may be due to the different Ni release rates, which will in turn affect the available Ni concentration. For the case of $Ni(acac)_2$, the strong chelating effect will cause Ni be reduced and released slowly, leading to a high P/Ni ratio in the early stages of the reaction relative to the weaker, coordinate bonded, $Ni(OAc)_2•4H_2O$ case. Therefore, the final product favors the more P-rich phase Ni_5P_4 for $Ni(acac)_2$ whereas $Ni(OAc)_2•4H_2O$ favors Ni_2P. For the organometallic precursor $Ni(COD)_2$, a combination of Ni_5P_4 and Ni_2P is produced, suggesting that this precursor is intermediate to $Ni(acac)_2$ and $Ni(OAc)_2•4H_2O$ in its rate of Ni release. Intriguingly our results are in direct contrast to those of the Tatsumisago group. In their study, when $Ni(OAc)•4H_2O$ was used as the precursor in the synthesis, the product favors the more P-rich product NiP_2

compared with Ni_2P produced by using $Ni(acac)_2$ as the precursor. One key difference between our work and that of the Tatsumisago group is the inclusion of OAm in our method, thus a series of reactions were done to further investigate the role the OAm plays in the synthesis.

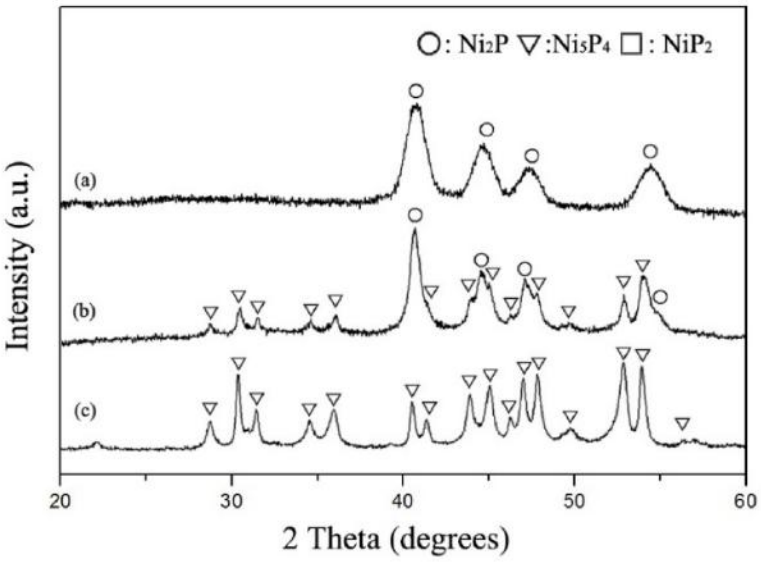

Figure 3.8. PXRD patterns of the product from Route 2 (Scheme 1) using different Ni precursors: (a) $Ni(OAc)_2•4H_2O$; (b) $Ni(COD)_2$ and (c) $Ni(acac)_2$.

3.3.7 Role of Oleylamine: Route 3

As mentioned above, without the existence of OAm in the system the phase formation trend ($Ni(OAc)_2•4H_2O$ favors the generation of NiP_2 and $Ni(acac)_2$ favors the generation of Ni_2P) is in direct contrast to what acquired from the system with OAm. Reactions with varied OAm/TOP ratio were carried out in order to understand the effect of OAm on the synthesis (Route 3, **Scheme 3.1**). Starting from conditions known to favor NiP_2, (i.e., a high TOP/Ni ratio (33.4) and low OAm/TOP ratio (0.045)) the amount of OAm was increased by replacing a portion of the octyl ether with OAm (decreasing a and increasing b, Route 3), thus increasing the ratio of OAm/TOP. When OAm/TOP is increased from 0.045 to 0.67

and 1.34, the product phase changed from NiP_2 to a mixture of Ni_5P_4, NiP_2 and then Ni_5P_4 (**Figure 3.9a**, **b** and **3.8c**). For the OAm/TOP ratio of 1.34, there was no octyl ether in the system; OAm was thus acting not only as a surfactant but also the sole solvent (a=0, b=10). Changing the reaction time from 1 to 48 h, the heating temperature from 350 to 385 °C and the P/Ni ratio from 21.6 to 61.6 had no effect; the obtained phase in every case was Ni_5P_4 (**Figure 3.8c** and **3.10**).

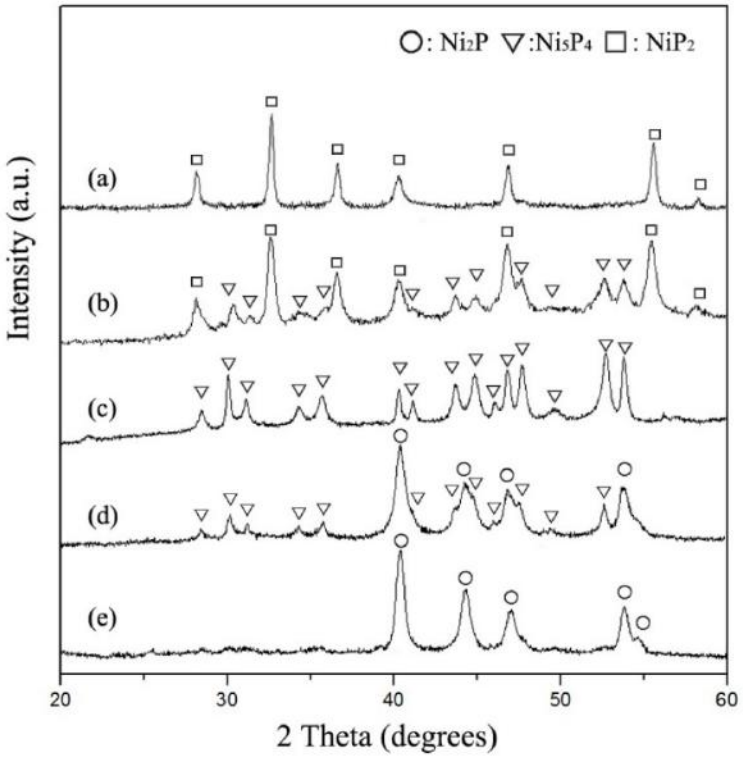

Figure 3.9. PXRD patterns of the products from Route 3 (Scheme 3.1) as a function of OAm/TOP ratio; reactions were carried out at 370 °C for 24 h with 0.73 mmol $Ni(acac)_2$.

We expect this observation reflects a balance between the high P/Ni ratio (>21.6) guaranteeing sufficient phosphidation of the final product to facilitate the formation of a P-rich phase, while at the same time, the high OAm/TOP ratio enables OAm to compete with TOP to bond with the particle surface, thereby

limiting the quantity of TOP participating in the reaction. The reducing nature of OAm may also be contributing to the balancing act. Thus, the intermediate phosphided phase Ni_5P_4 is stable relative to NiP_2, even when the P/Ni ratio reaches as high as 61.6. In contrast, Ni_2P can be accessed by decreasing the TOP amount. Thus, when the the OAm/TOP ratio was increased from 1.34 to 8.93 and to 13.4, the product phase changed from Ni_5P_4, to a mixture of Ni_5P_4, Ni_2P, and subsequently, Ni_2P (**Figure 3.9c**, **d**, and **e**, **Table 3.1c, d,** and **e**). Accordingly, much lower P/Ni ratios are needed to favor Ni_2P in Route 3 (high OAm/Ni; P/Ni = 3.34, **Figure 3.7a**) whereas in Route 2, Ni_2P is favored even at relatively large P/Ni ratios (lower OAm/Ni; P/Ni = 13.44, **Figure 3.1a**). Intriguingly, under conditions where the OAm amount is high (a=0, b=10) in Route 3, varying the Ni precursor ($Ni(acac)_2$, $Ni(COD)_2$ and $Ni(OAc)_2•4H_2O$) has no effect on the outcome (Ni_5P_4), indicating that dissolving the different Ni sources in OAm may form a single precursor "Ni(OAm)", which favors the formation of Ni_5P_4 (unless the TOP concentration is dramatically reduced).

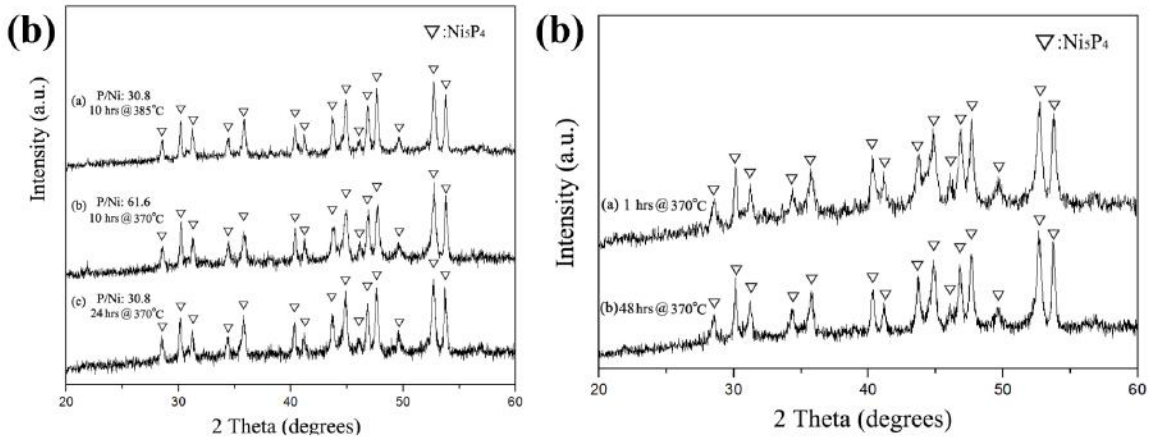

Figure 3.10 PXRD patterns of the product from Route 3 (a) as a function of heating temperature (370, 385 °C), P:Ni ratio (30.8, 61.6) and heating time (10, 24 h); (b) as a function of heating time (1, 48 h) at 370 °C.

Table 3.1. Reaction parameters and final product phase from Route 3

	OAm	TOP	OAm/TOP	TOP/Ni	Product phase
a	1.0 mmol	22.4 mmol	0.045	33.4	NiP_2
b	15.0 mmol	22.4 mmol	0.67	33.4	NiP_2, Ni_5P_4
c	30.0 mmol	22.4 mmol	1.34	33.4	Ni_5P_4
d	30.0 mmol	3.36 mmol	8.93	5.01	Ni_5P_4, Ni_2P
e	30.0 mmol	2.24 mmol	13.39	3.34	Ni_2P

3.4 Conclusions

The various roles of reaction parameters on the extent of phosphidation of Ni to produce crystalline nanoparticles of Ni_2P, Ni_5P_4 or NiP_2 from reaction of nickel complexes with TOP in OAm solutions are depicted in Scheme 3.2. With or without the 230 °C intermediate step, for a constant concentration of Ni precursor in the system, increasing the TOP/OAm ratio, reaction temperature and time favors the formation of more P-rich phases. However, the use of an intermediate 230 °C soak step, common to metal phosphide nanoparticle syntheses, was found to have no effect on the synthesis of Ni_2P nanoparticles, but dramatically reduced the extent of phosphidation possible, even at very high TOP/Ni ratios, producing Ni_5P_4 or NiP_2 samples that always had significant Ni_2P impurities. Particles of Ni_5P_4 and NiP_2 could be obtained as phase-pure products when the intermediate 230°C step was removed. The OAm/TOP ratio also has a strong effect on the system, enabling tuning from pure Ni_2P to Ni_5P_4 and NiP_2 by decreasing the OAm/TOP ratio. Additionally, large concentrations of OAm attenuate the behavior of different Ni reagents (COD, acac, or OAc complexes), likely by formation of a common intermediate, leading preferentially to Ni_5P_4 unless the TOP/Ni ratio is dramatically reduced, favoring Ni_2P. At low OAm/TOP ratio, the chelate complex $Ni(acac)_2$

favors Ni_5P_4 (i.e., less Ni available in the reaction) and $Ni(OAc)_2$ favors Ni_2P. Under the extreme phosphidation conditions required to favor Ni_5P_4 and NiP_2 (large excess of TOP), the 20-30 nm crystallites assemble into supraparticles with diameters of 100-500 nm. Overall, this work addresses a knowledge gap in the phase evolution for the P rich side of the Ni-P nanoparticle system. The strategy used to prepare more P-rich nickel phosphide nanoparticles should be applicable to other metal phosphide systems, thus facilitating the development of this important class of nanomaterials for energy storage and catalysis.

Scheme 3.2. Illustration of the roles played by various synthetic levers in controlling the phase in nickel phosphide nanoparticles. The crystal structures shown inside correspond to Ni_2P (hexagonal), Ni_5P_4 (hexagonal) and NiP_2 (cubic) as determined from XRD.

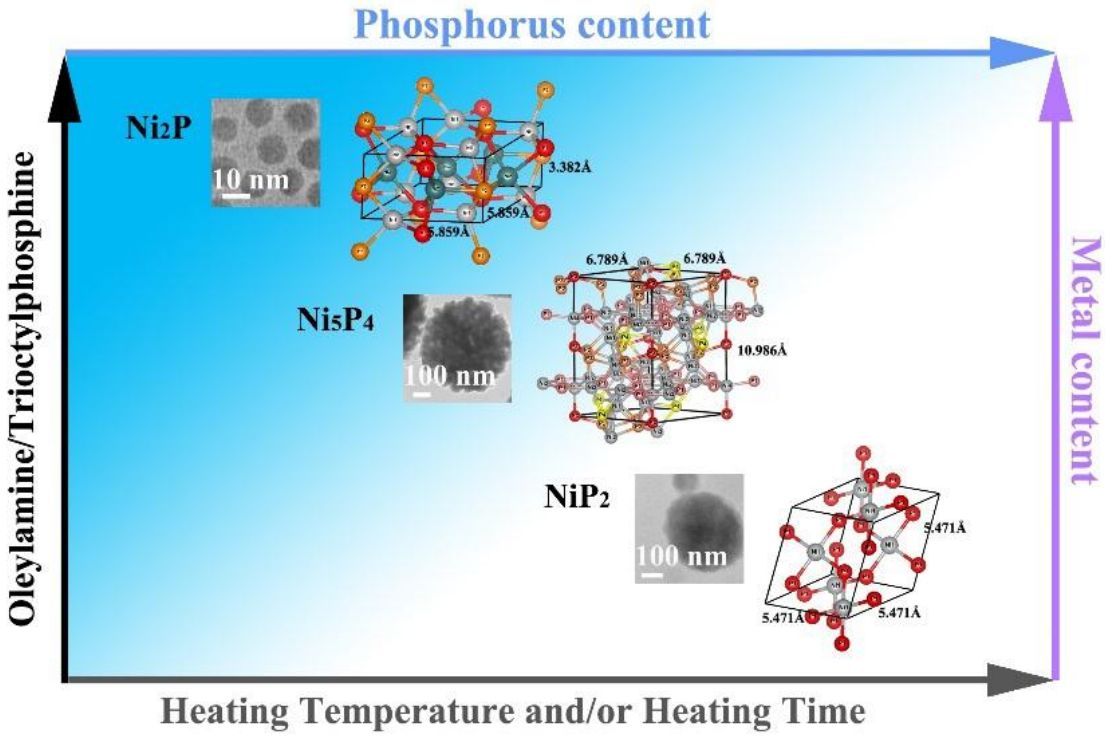

CHAPTER 4. CONTROL OF COMPOSITION AND SIZE IN DISCRETE $CO_XFE_{2-X}P$ NANOPARTICLES: CONSEQUENCES FOR MAGNETIC PROPERTIES

ABSTRACT

In this work, a solution-phase method was developed for the synthesis of $Co_xFe_{2-x}P$ nanoparticles over all x ($0 \leq x \leq 2$). The nanoparticles vary in size, ranging from 16.5 to 20 nm with standard deviations ≤14%. The synthesis involves preparation of CoFe alloy nanoparticles and high temperature conversion into crystalline ternary phosphide nanocrystals. The target composition can be controlled by the initial metal precursor ratio and the size of $Co_xFe_{2-x}P$ (from 12-22 nm) can be tuned by varying the OAm/metal ratio. Mössbauer data shows that Fe has a strong preference for the square pyramidal site over the tetrahedral site. Magnetic measurements on $Co_xFe_{2-x}P$ nanoparticles showed a strong compositional dependence of the Curie temperature (T_C); CoFeP and $Co_{0.7}Fe_{0.3}P$ have T_Cs > 340 K and are superparamagnetic at room temperature.

Li, D., Perera, M., Kulikowski, B., Lawes, G., Seda, T., Brock, S. L. Chemistry of Materials, **2016**, 28, 3920-3927.

4.1 Introduction

Nanostructured ternary transition metal phosphides have drawn increasing attention due to their catalytic and magnetic properties, which can be modified by changing the particle composition, structure, and size.[26, 70-73]

Due to the catalytic properties of cobalt phosphide and iron phosphide,[74-77] $Co_xFe_{2-x}P$ may not only be a highly effective OER catalyst but also a promising catalyst candidate for the hydrogen evolution reaction (HER). Indeed, the more P-rich phase $Co_{0.5}Fe_{0.5}P$ has already been demonstrated as an effective HER catalyst.[73] Moreover, by changing the amount of iron in cobalt phosphide bulk materials, the magnetic properties can be altered from paramagnetic Co_2P to ferromagnetic $Co_xFe_{2-x}P$ with a tunable Curie point close to or above room temperature,[54] which makes this material potentially suitable for magnetic imaging, therapies, refrigeration, or data storage.[55-57]

Despite their promise, comparatively little research has been done on ternary (relative to binary) nanoparticles of metal phosphides, including $Co_xFe_{2-x}P$.[26, 36] There are two major challenges in the synthesis of ternary phosphide nanoparticles: the first is the possibility of phase segregation due to the different reactivities of the two metal precursors and the second is the difficulty in controlling the stoichiometric phases of the final product because of the various oxidation states that the transition metals can adopt. Accordingly, to establish the comprehensive evolution of magnetic and catalytic properties for nanoparticles of $Co_xFe_{2-x}P$, a protocol that can control size and morphology over all compositions is needed.

In this chapter, a single-pot protocol to synthesize $Co_xFe_{2-x}P$ nanoparticles with different compositions ($0 \leq x \leq 2$), size and morphology is established and the mechanism of the nanoscale ternary phosphide formation process is ascertained. The composition dependent magnetic properties of $Co_xFe_{2-x}P$ nanoparticles are studied, with iron-rich samples exhibiting room-temperature superparamagnetism not previously realized in phosphide nanoparticles.

The synthesis and characterization of $Co_xFe_{2-x}P$ nanoparticles were carried out by myself and an undergraduate student I mentored, Bogdan Kulikowsiki at Wayne State University. Magnetic property measurements were carried out by Maheshika Perera (the Lawes Group) in the Department of Physics and Astronomy at Wayne State University. Mὸssbauer spectroscopy measurements were collected and the data was interpreted by Prof. Takele Seda in the Department of Physics and Astronomy at Western Washington University.

4.2 Experimental

All materials used in the synthesis of cobalt iron phosphide nanoparticles are given in Chapter 2.

4.2.1 Synthesis of Nickel Phosphide Nanoparticles

The synthesis is outlined in **Scheme 4.1** and comprises the synthesis of CoFe alloy nanoparticles and their in-situ conversion into phosphides by reacting them with TOP. First, 15.0 mL of octadecene was combined with 3.0 mL oleylamine in a 200 mL Schlenk flask with a condenser. The system was degassed at 120 °C for 20 min to remove any moisture or oxygen, followed by purging with argon for 30 min. The temperature was then increased to 200 °C. CoFe nanoparticles were

prepared by injecting a mixture of $Co_2(CO)_8$ and $Fe(CO)_5$ dissolved in 5.0 mL octadecene into the system. After 20 min aging, TOP was injected followed by aging at a temperature of 330 or 350 °C for 1.5 or 3 h ($x \geq 0.3$: T = 330 °C, t = 1.5 h; $x < 0.3$: T = 350 °C, t = 2.5 h). The black precipitate was sonicated in chloroform and reprecipitated by adding excess ethanol. This sonication-precipitation cycle was done at least three times to remove as much of the bound organics as possible from the system. The isolated black powder was then dried under vacuum.

Scheme 4.1. Synthesis of CoxFe2-xP ($0 \leqslant x \leqslant 2$) nanoparticles.

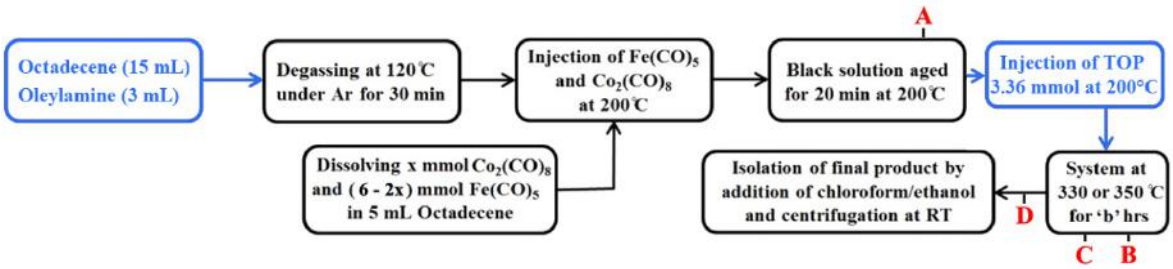

4.2.2 Characterization

Transmission electron microscopy (TEM), energy dispersive spectroscopy (EDS), scanning transmission microscopy (STEM) and powder X-ray diffraction (PXRD) were operated as describe in **Chapter 2**.

4.3 Results and Discussion

Based on our recent reports of $Ni_xM_{2-x}P$ (M = Co, Fe) nanoparticle syntheses employing acetylacetonate and carbonyl complexes,[70, 78] $Co(acac)_2$ and $Fe(CO)_5$ were chosen as metal precursors and a similar approach (inject $Fe(CO)_5$ into a Co-P solution at the intermediate 230 °C step followed by heating at 330 °C) was used to target $Co_xFe_{2-x}P$ nanoparticles (**Scheme 4.2**). However, CoO is present as a major secondary phase to $Co_xFe_{2-x}P$ (**Figure 4.1**), thus reducing the ability to

control the final phase and composition. The formation of oxide is attributed to the cleavage of the C-O bond in the actylacetonate ligand of $Co(acac)_2$.[79] Therefore, a new protocol was investigated to synthesize phase-pure $Co_xFe_{2-x}P$ without employing acac ligands.

Scheme 4.2. Reaction parameters when $Co(acac)_2$ and $Fe(CO)_5$ were used as metal precursors to prepare $Co_xFe_{2-x}P$ nanoparticles.

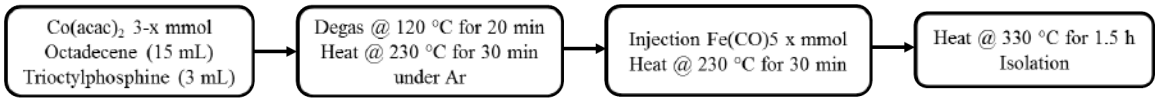

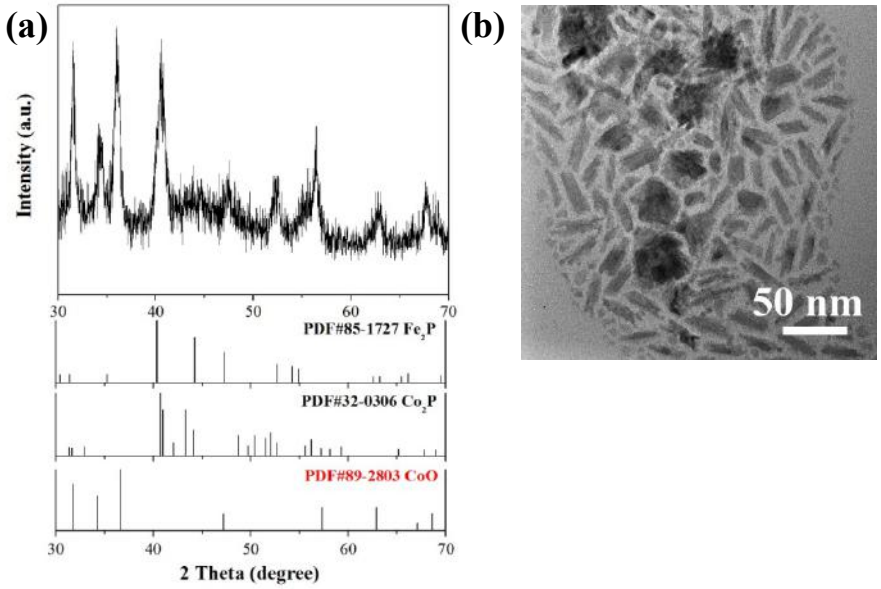

Figure 4.1 (a) PXRD patterns and (b) TEM image of product obtained using $Co(acac)_2$ and $Fe(CO)_5$ as metal precursors prepared by Scheme 4.2.

In order to develop a new approach to $Co_xFe_{2-x}P$ ($0 \leq x \leq 2$) nanoparticles, we opted to establish a set of reaction conditions under which both end points could be prepared. As $Co_2(CO)_8$ is expected to be more compatible with $Fe(CO)_5$, and it has also been used as a precursor to prepare cobalt phosphide,[9] we turned our

hand to this precursor. A protocol, developed by our group to synthesize Fe_2P phase pure nanoparticles,[6] was refined, as shown in **Scheme 4.1**, and enables the full range of compositions, $Co_xFe_{2-x}P$, to be synthesized, as discussed more fully below.

4.3.1 Synthesis of $Co_xFe_{2-x}P$ nanoparticles and their structural and morphological changes with composition.

A series of reactions was performed targeting a range of compositions by using different ratios of the metal precursors in the conditions shown in **Scheme 4.1**. At the Co-rich end of the spectrum ($x \geq 0.3$), formation of crystalline phases is attained at 330 °C, whereas a higher temperature (350 °C) is required for the most Fe-rich phases. The isolated particles were analyzed by PXRD to identify the phase (**Figure 4.2a**). Fe_2P and Co_2P adopt the hexagonal Fe_2P and orthorhombic Co_2P structure-types, respectively. Both have two metal sites, M(1) and M(2), with tetrahedral and square pyramidal geometries, respectively. However, the two structures differ in the packing of rhombohedral subcells containing M(1) and M(2) sites within the crystal (**Figure 4.2b**). As shown in Figure 1a, the patterns matched the expected line diagram for Co_2P or Fe_2P and no additional reflections were observed, suggesting an absence of significant (> 5%) crystalline impurities. The crystal structure of bulk $Co_xFe_{2-x}P$ transforms from orthorhombic Co_2P type ($x > 0.3$) to hexagonal Fe_2P type ($x \leq 0.3$).[54] However, due to the broad peaks associated with nanoscale crystalline dimensions, it is difficult to distinguish between Fe_2P and Co_2P structure types in these samples. Notably, the peaks in Co_2P around 40.7° and 55.6° are slightly shifted toward lower 2 theta values as

the content of the bigger volume atom Fe increased (**Figure 4.2b**), indicative of solid-solution formation.

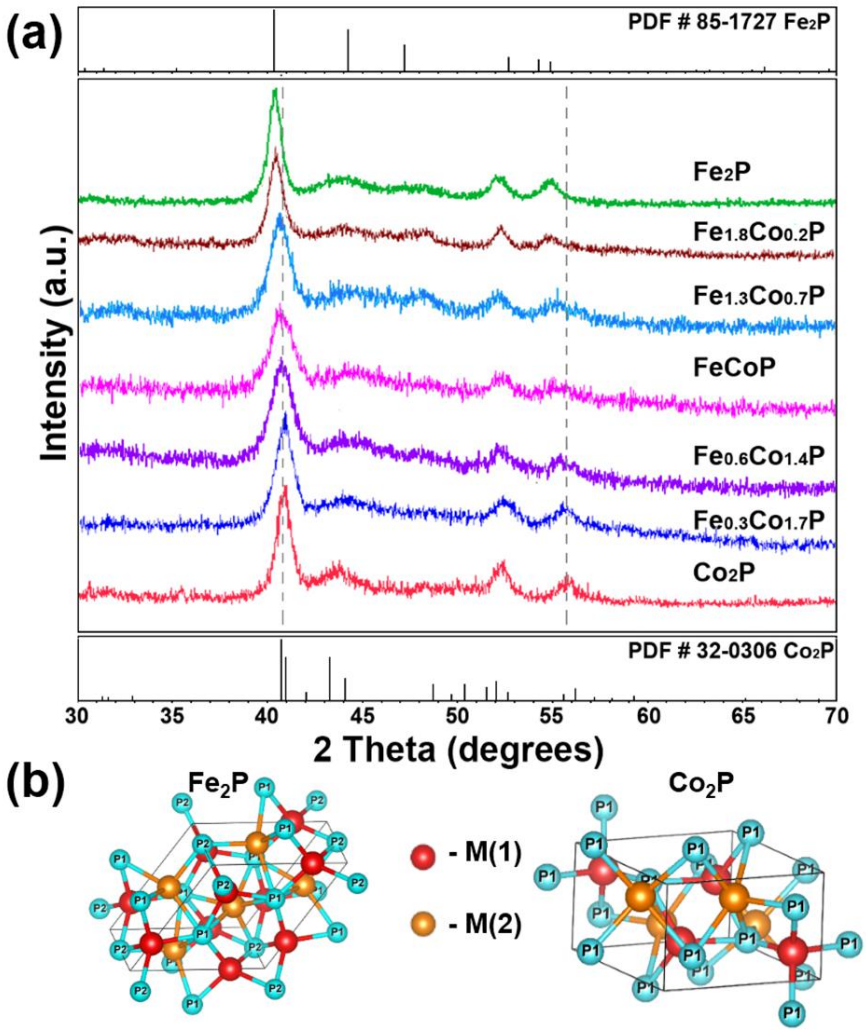

Figure 4.2. (a) PXRD patterns of different compositions of $Co_xFe_{2-x}P$ prepared with the conditions shown in Scheme 4.1. Reference patterns for Co_2P (PDF # 32-0306) and Fe_2P (PDF # 85-1727) are shown; droplines correspond to expected peak position for Co_2P. (b) Hexagonal Fe_2P structure-type (left) and orthorhombic Co_2P type (right).

As assessed by TEM (**Figure 4.3**), the particle diameters are in the range of 17-20 nm with ± 9.6-14% standard deviations (histograms shown in **Figure 4.4**). This is considerably smaller than particles produced by other methods[4,15] (~100's of nm) and theoretically results in a significant increase in external surface area.

From the EDS and ICP-MS analysis the compositions of the materials were calculated and the metal ratio was found to be close to the ratio employed in the synthesis, as shown in **Table 4.1**. The formation of hollow spheres (**Figure 4.3** inset) may be attributed to the different diffusion rates between metal ions and P ions according to the Kirkendall effect.[80]

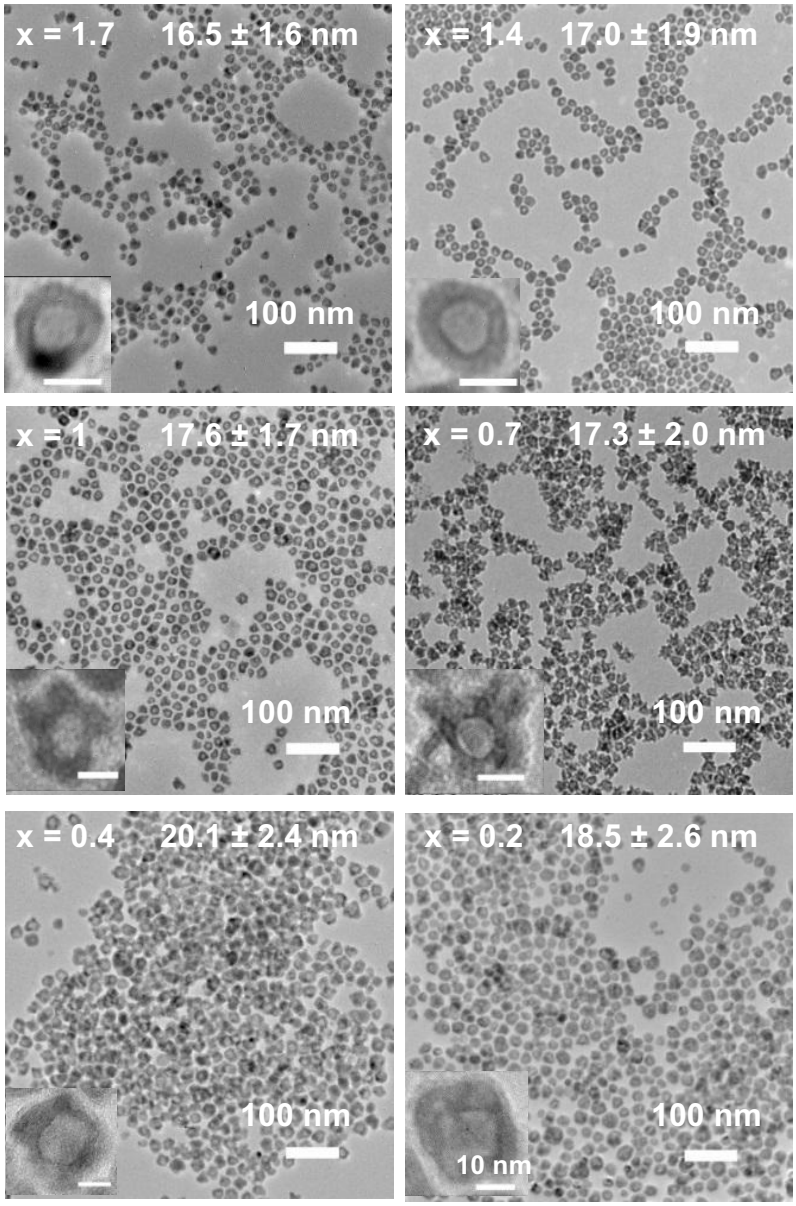

Figure 4.3. TEM images of different compositions of $Co_xFe_{2-x}P$ prepared by Scheme 4.1 (inset: HRTEM images, scale bars equal 10 nm).

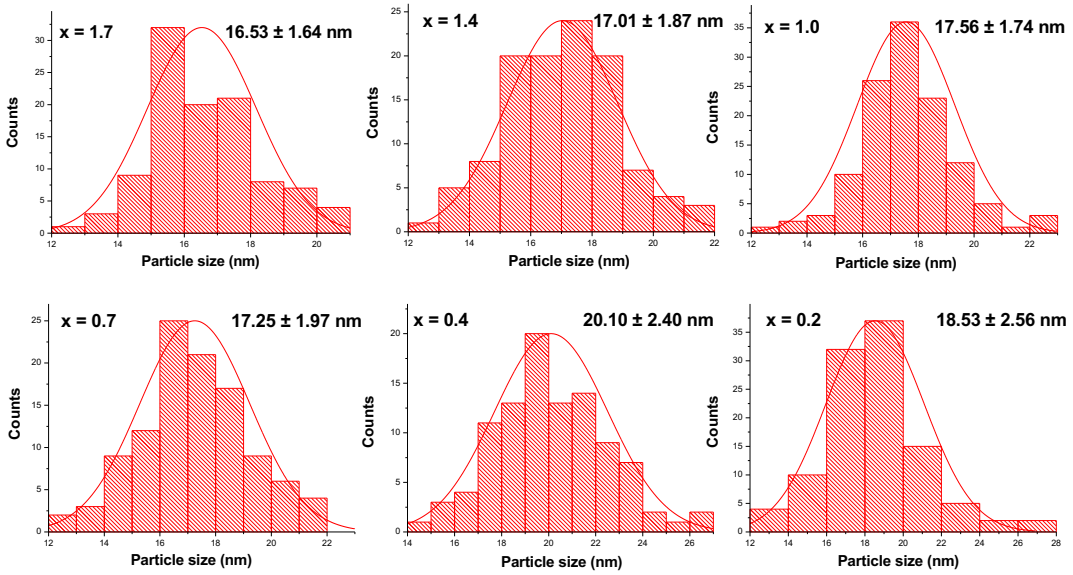

Figure 4.4. Histograms for the particle size distribution (measured from TEM) for different compositions of $Co_xFe_{2-x}P$ prepared by Scheme 4.1.

Table 4.1. Targeted and actual compositions (from EDS and ICP analysis) of $Co_xFe_{2-x}P$ nanoparticles.

Target ratio (Co : Fe)	Actual ratio from EDS (Co : Fe)	Actual ratio from ICP (Co : Fe)
1.70 : 0.30	1.72 : 0.28	1.69 : 0.31
1.45 : 0.55	1.40 : 0.60	1.41 : 0.59
1.00 : 1.00	1.04 : 0.96	1.03 : 0.97
0.75 : 1.25	0.71 : 1.29	0.70 : 1.30
0.30 : 1.70	0.33 : 1.67	0.33 : 1.67
0.20 : 1.80	0.22 : 1.78	0.21 : 1.79

STEM images and elemental mapping data for CoFeP nanoparticles are consistent with solid-solution formation (**Figure 4.5a**). The two metals (Co and Fe) are homogeneously distributed within each particle, suggesting phase-segregation is not occurring. It should be noted that while other compositions were not studied, we expect that they are similarly homogeneous based upon the bulk phase diagram, and the magnetic behavior of the materials (vide infra). The line scan (**Figure 4.5b**) confirms the low contrast region in the center of the particles is due

to hollow formation, as all three elements dip together. Moreover, the low contrast shell also has equal representation of all three elements, which suggests formation of an amorphous phosphate or phosphite layer due to surface oxidation. Overall the developed protocol is ideal to synthesize $Co_xFe_{2-x}P$ nanoparticles over the composition range ($0 \leq x \leq 2$). Samples prepared from ≥ 5 independently reactions all have similar morphologies and sizes with compositional variation limited to ± 5%, revealing the reproducibility of the synthetic method.

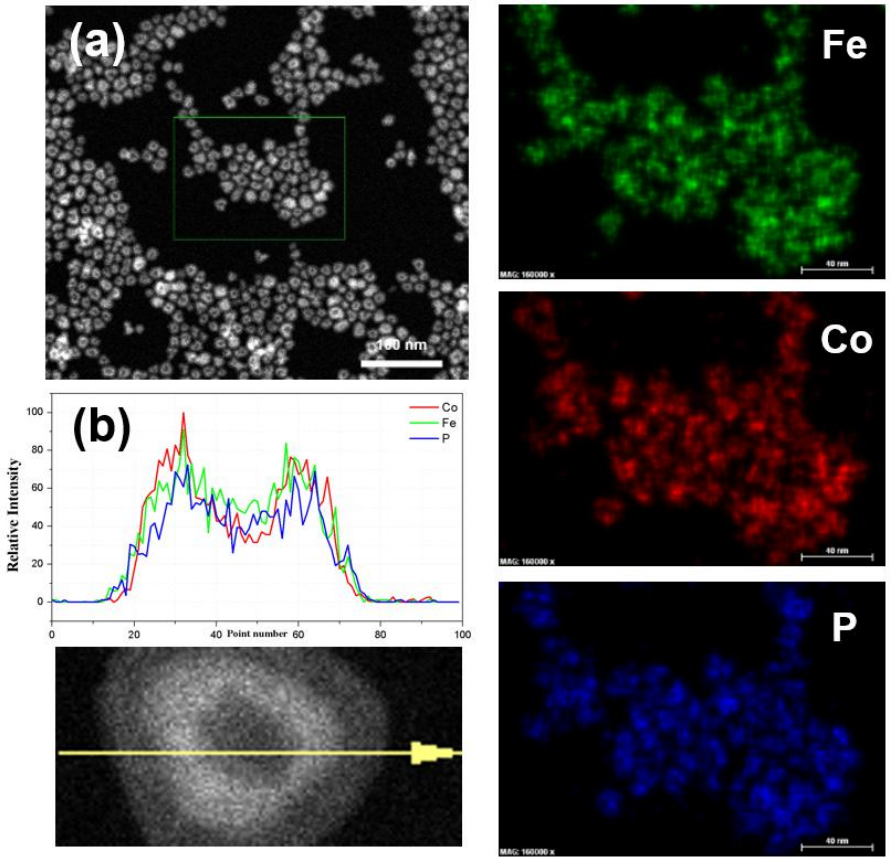

Figure 4.5. (a) HAADF image (left) and STEM elemental mapping data (right) corresponding to the rectangular region outlined in the HAADF image for a CoFeP sample. (b) Line scan for one CoFeP nanoparticle. In the plot of intensity versus point number, Fe is shown in green, Co in red, and P in blue.

As shown in the TEM micrographs (**Figure 4.3**), at both the Co-rich and Fe-rich end, the shape of the $Co_xFe_{2-x}P$ nanoparticles is spherical, which can be explained

by previous studies that showed that the final metal phosphide nanoparticles adopt a similar spherical shape and size to the metal nanoparticles that formed at the intermediate step of the reaction. Thus, the spherical metal particles act as templates for further growth.[9, 32] Intriguingly, the middle range ($0.8 < x < 1.4$) $Co_xFe_{2-x}P$ nanoparticles are roughly spherical but have a scalloped edge, reminiscent of many small particles aggregating in the course of phosphidation. We hypothesize that the precursor particles for intermediate compositions may be smaller than those of the end-products and that the higher surface energy associated with the small size leads to aggregation and the aggregate serves as a template for the final phosphide. A series of reactions was conducted to study the mechanism of particle formation in order to ascertain the validity of this hypothesis.

4.3.2 Mechanistic studies on particle formation.

The mechanism of the $Co_xFe_{2-x}P$ nanoparticle formation process was investigated by TEM and XRD analysis of products obtained at different points in the reaction (**Scheme 4.1**, A, B, C and D). CoFeP was chosen as a representative composition. XRD data of sample A (**Figure 4.6**, diffractogram A) indicated the formation of CoFe alloy nanoparticles (ANPs) after injecting the mixture of $Fe(CO)_5$ and $Co_2(CO)_8$ dissolved in octadecene into a degassed mixture of octadecene and OAm maintained at 200℃. These irregular shaped CoFe ANPs have an average size of 5.2 ± 1.3 nm (**Figure 4.6**, micrograph A) with the two metals distributed homogeneously within each particle (**Figure 4.7**) and are strongly attracted to the magnetic stir bar, consistent with the formation of a ferromagnetic phase.

Compared with single metal precursors (Co nanoparticle: 12 nm,[9] Fe nanoparticle: 15 nm[6]), these alloy nanoparticles have a much smaller size, presumably due to more facile nucleation. This may reflect a greater reactivity between Fe and Co relative to reactivity between Fe-Fe or Co-Co. Sample B was collected after injecting 3.36 mmol TOP into CoFe ANPs and increasing the reaction temperature to 330℃. In diffractogram B (**Figure 4.6**), the CoFe alloy is still the majority phase. The peak at 44.6° becomes broader, suggesting the crystallinity of the ANP decreased, presumably due to a reaction with the injected TOP. Additionally, a shoulder at 41° was observed, which corresponds to the (112) reflection of Co_2P type CoFeP. While the average size of particles in sample B increased to 13.0 ± 2.2 nm (**Figure 4.6**, micrograph B) and the shape became irregular, suggesting several CoFe ANPs fusing together to form relatively large $(CoFe)_xP_y$ nanoparticles upon injection of TOP and increase of temperature. After heating for 0.5 hour at 330℃, this shoulder at 41° evolved into the most intense peak and two additional peaks at 52° and 56° emerged, indicating that a significant portion of $(CoFe)_xP_y$ has converted into CoFeP (**Figure 4.6**, diffractogram C). Nanoparticles with an average size of 14.8 ± 4.0 nm are evident in the corresponding micrograph. Some hollow structures started to appear in the center of the nanoparticles, which may be attributed to the diffusion rate differences between metal ions moving out and P diffusing inside, indicating the ongoing progression of the Kirkendall effect. Finally, at the completion of the reaction, the XRD pattern of D (**Figure 4.6**, diffractogram D) matches that for Co_2P, suggesting formation of CoFeP is complete. Nanoparticles in sample D adopt a completely hollow structure. The

crystallite size of CoFeP nanoparticles, as determined by application of the Scherrer equation to the (112) reflection, is 9.2 nm, consistent with what is observed by TEM when the void space is accounted for (17.6 ± 1.7 nm with avoid diameter of ~ 8 nm), suggesting well-crystallized particles. The particles are not spherical, but have a scalloped edge, which is a consequence of nanoparticle aggregation during the initial state of phosphidation, presumably a consequence of surface energy minimization. Note that the scalloped edge increases the theoretical surface area relative to a sphere, potentially enhancing surface-dependent properties such as catalytic activity.

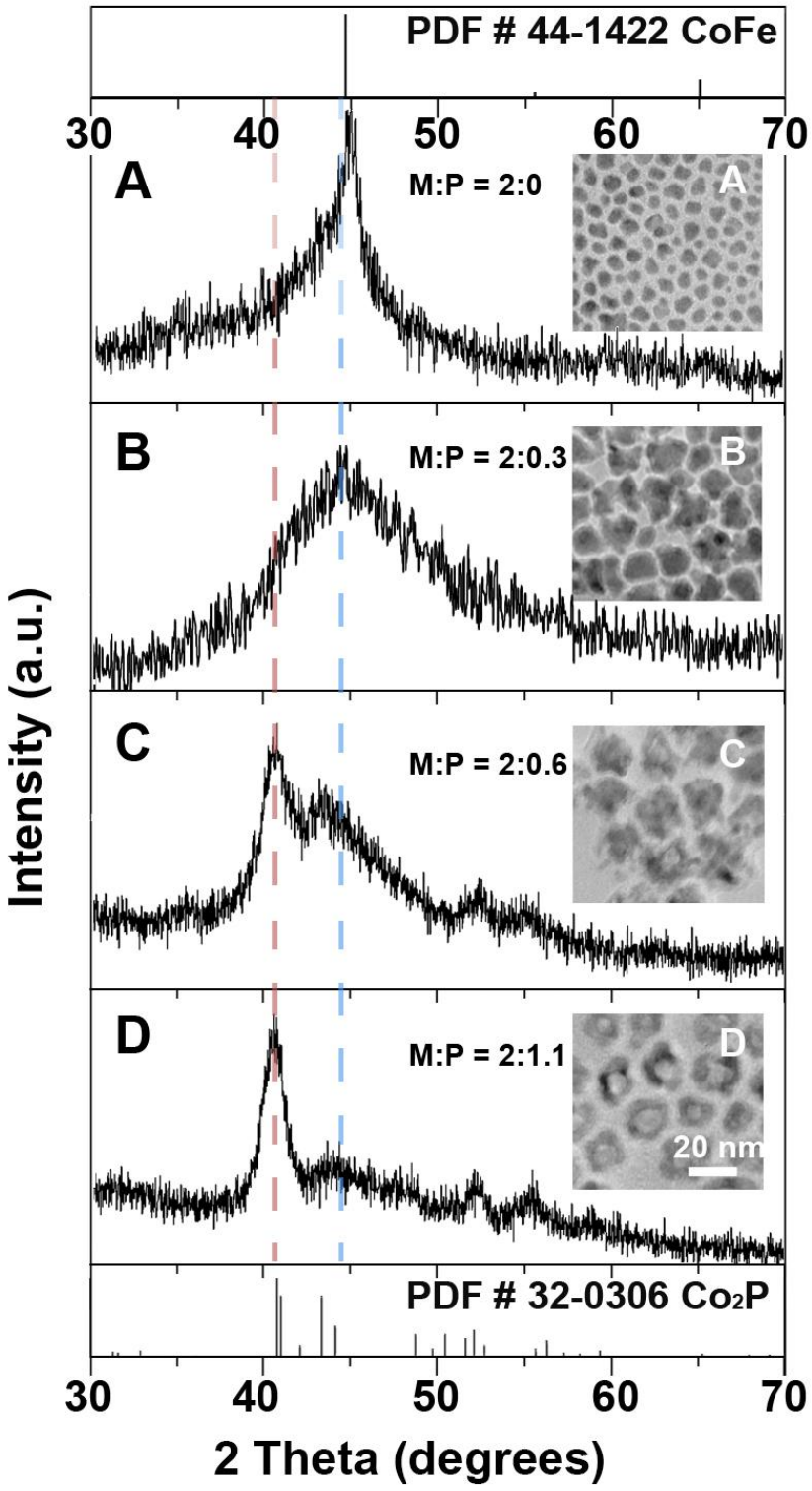

Figure 4.6. PXRD patterns of the samples A-D; the insets show the corresponding TEM images (M:P ratios were acquired from EDS spectra). The scale bar (20 nm) is the same for all micrographs.

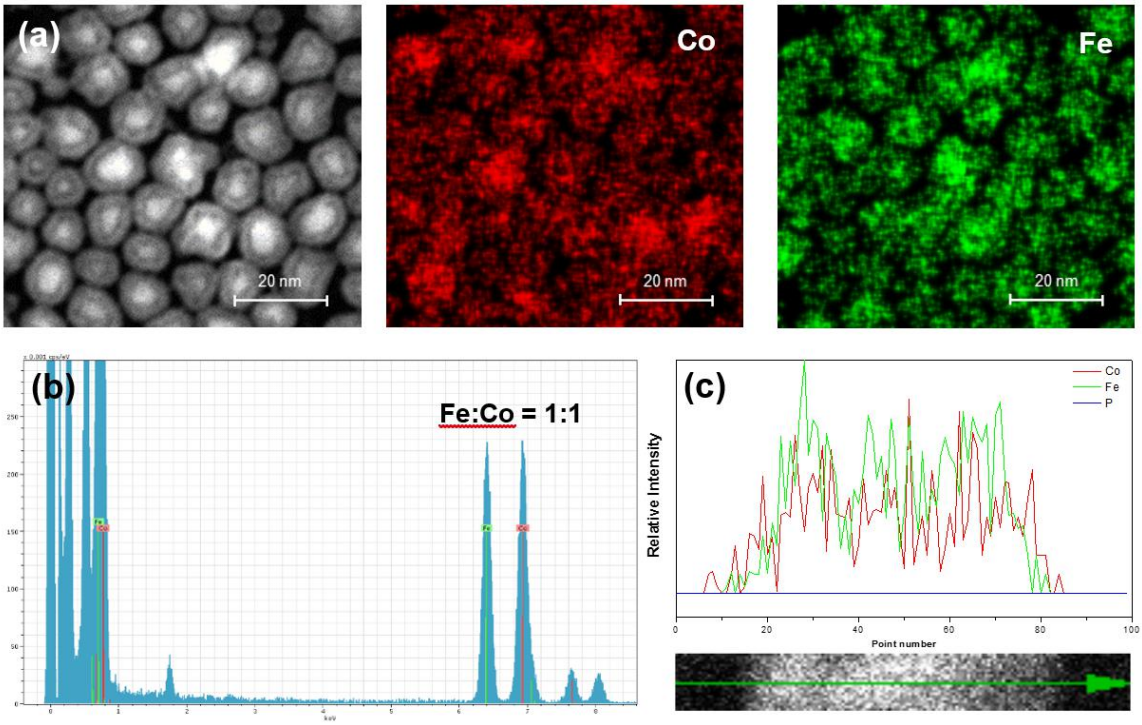

Figure 4.7. (a) HAADF image (left) and STEM elemental mapping data (right) and (b) EDS spectra for CoFe alloy nanoparticles (sample A). (c) Line scan for one CoFe alloy nanoparticle. In the plot of intensity versus point number, Fe is shown in green, Co in red.

4.3.3 Size control of the ternary phase.

Previous studies showed that the distribution of metal in M(1) and M(2) sites may be sensitive to the size of the phosphide nanoparticles,[81] which will influence the magnetic and catalytic properties of metal phosphides.[70, 81] Thus, it is advantageous to control the size of $Co_xFe_{2-x}P$ nanoparticles. It is known that generally increasing the initial TOP/metal ratio favors the formation of smaller sized metal phosphide nanoparticles.[32, 78] However, as shown in **Figure 4.8**, in the CoFeP case, either increasing or decreasing the P/M ratio (changing the quantity of TOP added into the system) leads to impurities (incompletely converted CoFe or overreacted CoP-type $CoFeP_2$) generated as the final product. In order to

control the size, and in the meantime maintain the phase purity of the final product, different quantities of OAm were used in the synthesis.

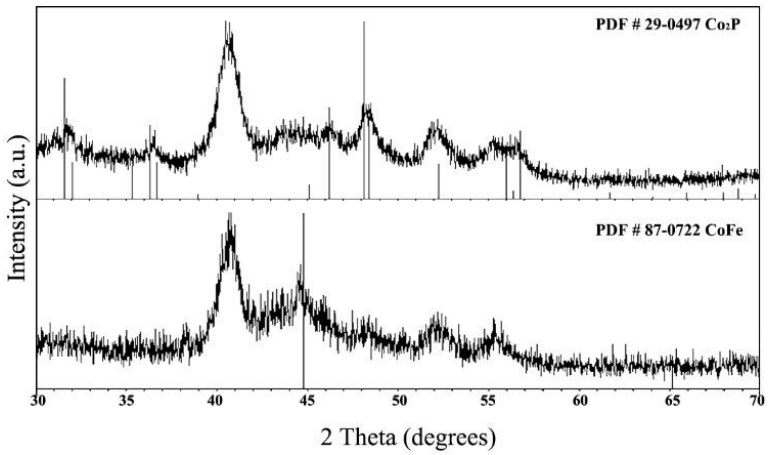

Figure 4.8. PXRD patterns of the CoFeP nanoparticles from Scheme 4.1 as a function of TOP/metal ratio: (a) TOP/metal = 0.75 (b) TOP/metal = 0.45.

The reactions were carried out under conditions optimized for Co_2P, Fe_2P and CoFeP (P:M = 0.56, 1.5 h; 330 °C for Co_2P and CoFeP, 350 °C for Fe_2P). The ratio of OAm/metal used in the reaction was varied from 0.25 to 3. As shown in **Figure 4.9**, the average size of Co_2P and Fe_2P nanoparticles changed from 14.0 ± 2.1 to 17.7 ± 2.2 and 13.0 ± 1.5 nm to 24.9 ± 3.5 nm, respectively when the OAm/metal ratio changed from 1.5 to 3. Correspondingly, for ternary phase CoFeP nanoparticles, the average size changed from 12.2 ± 1.7 to 17.5 ± 1.7 to 21.4 ± 2.6 nm when the OAm/metal ratio increased from 0.5 to 1.5 to 3 (**Figure 4.10**). This is consistent with what is observed in the nickel and nickel phosphide nanoparticle system (**Chapter 3**): the presence of excess OAm favors formation of larger nanocrystals.[5, 61, 82] Presumably, the increasing amount of oleylamine decreases the binding ability and reaction rate of TOP with the alloy precursor nanoparticles.[83] This slows the generation of metal-P nuclei and results in larger particle formation (fewer nuclei can grow larger due to the excess growth reagent).

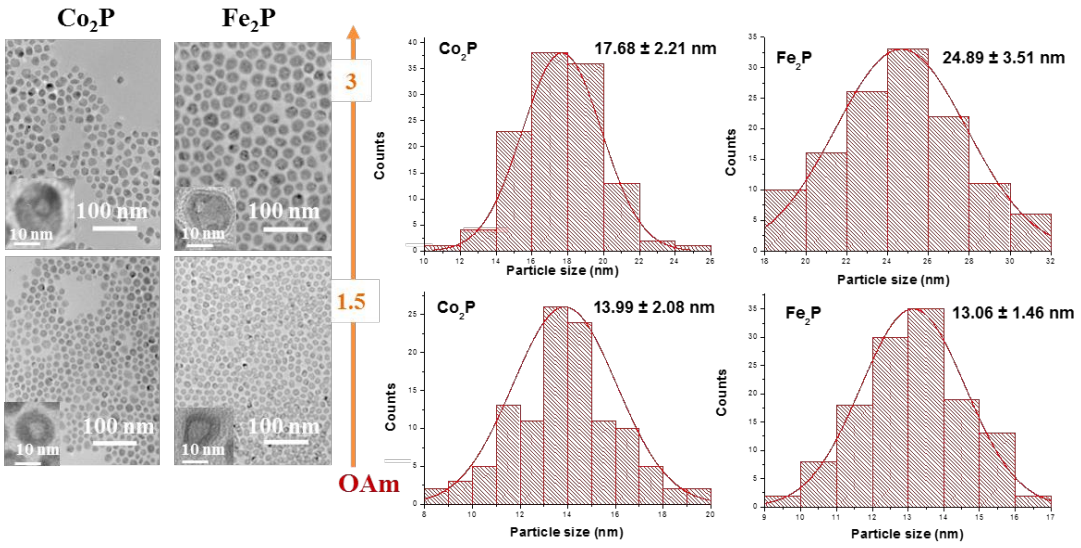

Figure 4.9. TEM images of Co_2P and Fe_2P nanoparticles prepared in Scheme 4.1 as a function of OAm.

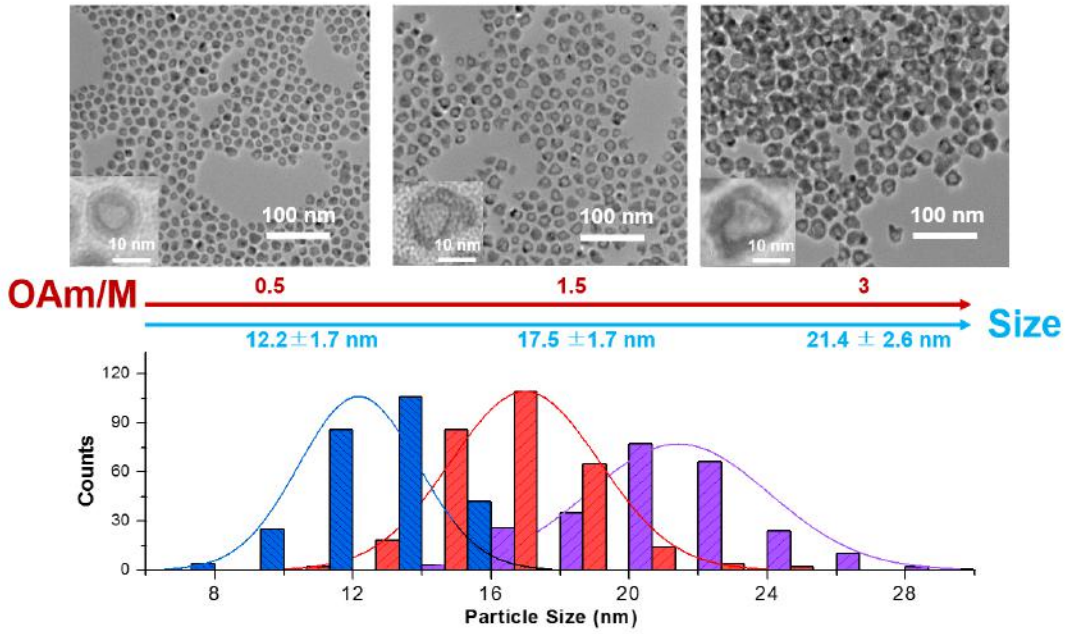

Figure 4.10. TEM images of CoFeP nanoparticles prepared in Scheme 1 as a function of OAm.

4.3.4 Magnetic Properties of $Co_xFe_{2-x}P$ Nanoparticles.

Fe_2P is ferromagnetic and exhibits a weak first-order magnetoelastic phase transition associated with the Curie transition at T_C = 217 K. It is well-established

that T_C can be driven up to 459 K with the incorporation of Co into Fe_2P system (x = 0.76, $Co_{0.76}Fe_{1.24}P$) in the bulk.[54] Due to the partial antiferromagnetic coupling caused by the overlap of the bottom of the β-spin band with the top of the α-spin band at the Fermi level, Fe_2P has a moment that is suppressed below the expected value. Similar to what happens when Ni is substituted into the Fe_2P series,[70] substitution of Co raises the ordering temperature and strengthens ferromagnetic ordering due to the addition of β-spin electrons to σ-bond orbitals, which eliminates the antiferromagnetic component.[54, 84, 85] With an increase of Co in the system, the moment at the Fe(2) atoms increases first ($0.32 < x < 0.8$) and saturates for $x > 0.8$ while the moment at the Fe(1) atoms increase slowly without saturating. Initially, Co atoms prefer to occupy the M(1) sites and thus the overall moment and T_C increase to the maximum value due to the boost of the moment at Fe(2) atoms ($0.32 < x < 0.8$). With further addition of Co, more Co atom occupation of M(2) sites, along with the moment saturation of Fe(2) atoms, results in an overall moment decrease and consequently, a drop in T_C ($x > 0.8$). [84]

Motivated by the composition dependent T_C of $Co_xFe_{2-x}P$ shown in the bulk (first increasing to a maximum of 459 K for x = 0.76, followed by a decrease to 219 K at x = 0), and the possibility of achieving room temperature superparamagnetic or ferromagnetic nanoparticles, $Co_xFe_{2-x}P$ nanoparticles with different compositions (x=0.2, 0.7, 1, 1.4, 1.7) and similar sizes (18 - 20 nm) were studied. The temperature (T) dependence of the magnetization (M) was determined under zero-field-cooled (ZFC) and field-cooled (FC) conditions in the temperature range 10-350 K under an applied magnetic field of 100 Oe. All samples showed maxima

in their ZFC curves near the intersection of the FC with the ZFC, corresponding to their blocking temperature (T_B), which occurred between 30 and 235 K (**Figure 4.11** and **Table 4.2**).

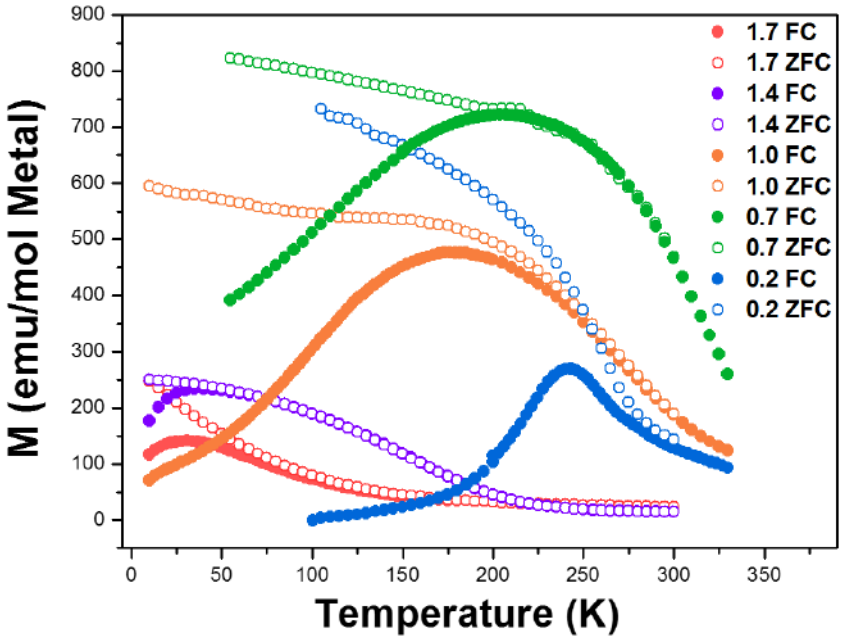

Figure 4.11. ZFC and FC plots of $Co_xFe_{2-x}P$ nanoparticles (x = 1.7, 1.4, 1.0, 0.7, 0.2).

Table 4.2. Reaction parameters and final product phase from Route 3

Sample composition	Size (nm)	T_B (K)	T_C (K)	$T_{C\ bulk}$ (K)
$Co_{1.7}Fe_{0.3}P$	17.34±2.91	30	145	140
$Co_{1.4}Fe_{0.6}P$	16.22±2.47	50	230	275
CoFeP	18.51±2.22	179	>340	425
$Co_{0.7}Fe_{1.3}P$	19.38±2.06	210	>340	458
$Co_{0.2}Fe_{1.8}P$	21.79±3.58	235	285	365

To determine the exact Curie temperature (T_C) of the $Co_xFe_{2-x}P$ samples, Arrott plots (M^2 vs. H/M, **Figure 4.12**) were collected at temperatures around the expected T_C. Arrott plots yield a set of parallel lines with the curve corresponding to T = T_C passing through the origin. For x = 1 and 0.7 there is no curve passing through the origin below 340 K, indicating that the T_c for CoFeP and $Co_{0.7}Fe_{1.3}P$

are above 340 K (the limit of the instrument). However, the 340 K plot for CoFeP is much closer to linearity than $Co_{0.7}Fe_{1.3}P$, suggesting that the latter will have a higher Tc than the former, in line with predictions based on bulk phases. The T_c's of different compositions of $Co_xFe_{2-x}P$ nanoparticles are shown in **Table 4.2** and the T_C plot of both bulk materials and nanoparticles are shown in **Figure 4.13**. The $Co_xFe_{2-x}P$ nanoparticles and bulk materials exhibit a similar compositional dependence of T_C: the T_C increases with the increasing incorporation of Fe at the Co-rich side while at the Fe-rich side, the T_C decreases with the increasing incorporation of Fe amount. For bulk materials, the T_C exhibits the highest value of 459 K for x = 0.76.

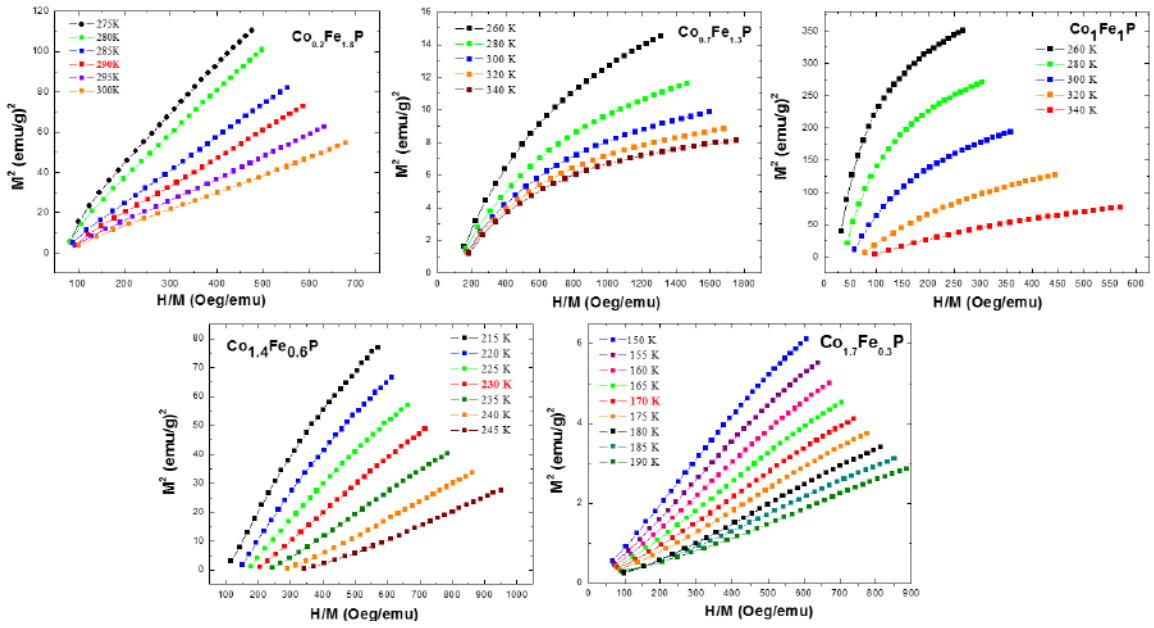

Figure 4.12. Arrot plots of different compositions $Co_xFe_{2-x}P$ nanoparticles. The T_c for $Co_{0.7}Fe_{1.3}P$ appears to be greater than the T_c for CoFeP, based on the greater deviation from linearity in the former for the 340 K data.

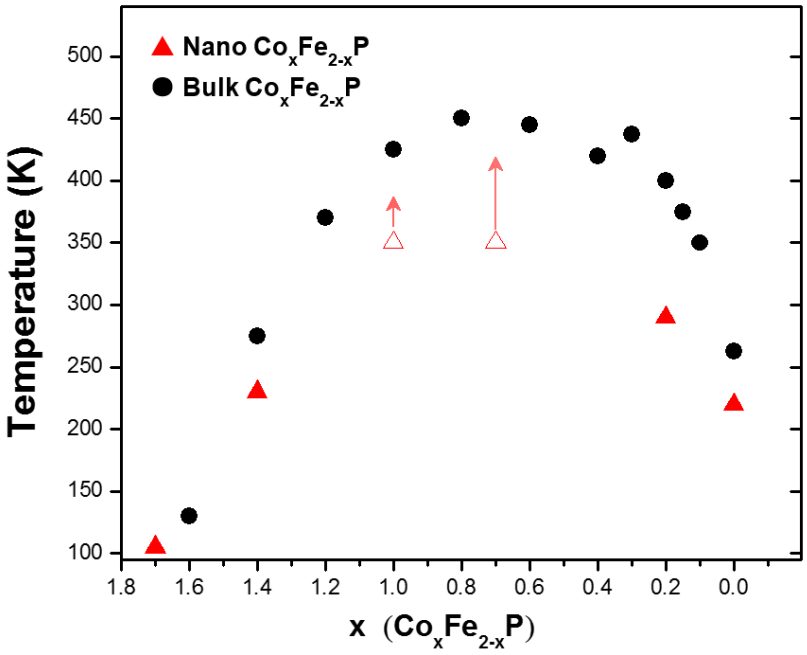

Figure 4.13. T_C value of $Co_xFe_{2-x}P$ nanoparticles (triangle) and bulk samples (circle, reported in ref[54]) as a function of x. The Tc for nanoscale Fe_2P was taken from ref[6]. The open triangles correspond to the upper limit of the instrument. The arrows reflect the relative magnitude as a function of x based on qualitative analysis of Arrott plots (Figure 4.12).

Our related study of $Fe_xNi_{2-x}P$ revealed that the strong site-preferences obtained in the bulk-phase were less pronounced at the nanoscale, and we observed an anomalous trend in the T_C as a function of composition, with the maximum of the observed value at x=1.8 ~250 K instead of ~350 K as obtained in bulk.[70] Likewise, x – 1.4 had a higher than expected T_C of 265 K. We hypothesized that the nanoscale preparation may result in weaker preferences, and thus a more random distribution of metals. Accordingly, we performed Mössbauer studies on $Co_xFe_{2-x}P$ nanoparticles to ascertain whether the relaxation of site preferences is a general phenomenon for these systems.

Mössbauer data collected on the $Co_xFe_{2-x}P$ nanoparticles (**Figure 4.14**) shows that Fe has a strong preference for the M(2) site and occupation of the M(1) site does not become apparent until the M(2) site is nearly full. Likewise, the Co atoms initially occupy the M(1) site, and only start occupying M(2) sites when x is close to 1.0. When x = 1.0, ~12% of Co atoms occupy the M(2) sites, which is in agreement with the findings of Fruchart et al. for the bulk phase.[54] Interpretation of Mössbauer data for Fe-rich samples proved problematic due to the presence of an Fe-containing impurity. The identity of this impurity remains unknown, as no unindexed peaks are present in the PXRD data. However, given the small crystallite sizes and the limitations of the XRD technique, it is not surprising that it is not detected.[6] Overall, the strong M(2) preference for Fe is consistent with what is observed in the bulk $Co_xFe_{2-x}P$ system, that the less d-electron rich Fe atom would normally prefer the larger site M(2) (243 pm vs. M(1) 223 pm).[54, 86] Thus, as the distribution of Fe and Co on the two sites is not affected by formation on the nanoscale, the parallels between the bulk and nanoparticle magnetic data are perhaps not surprising.

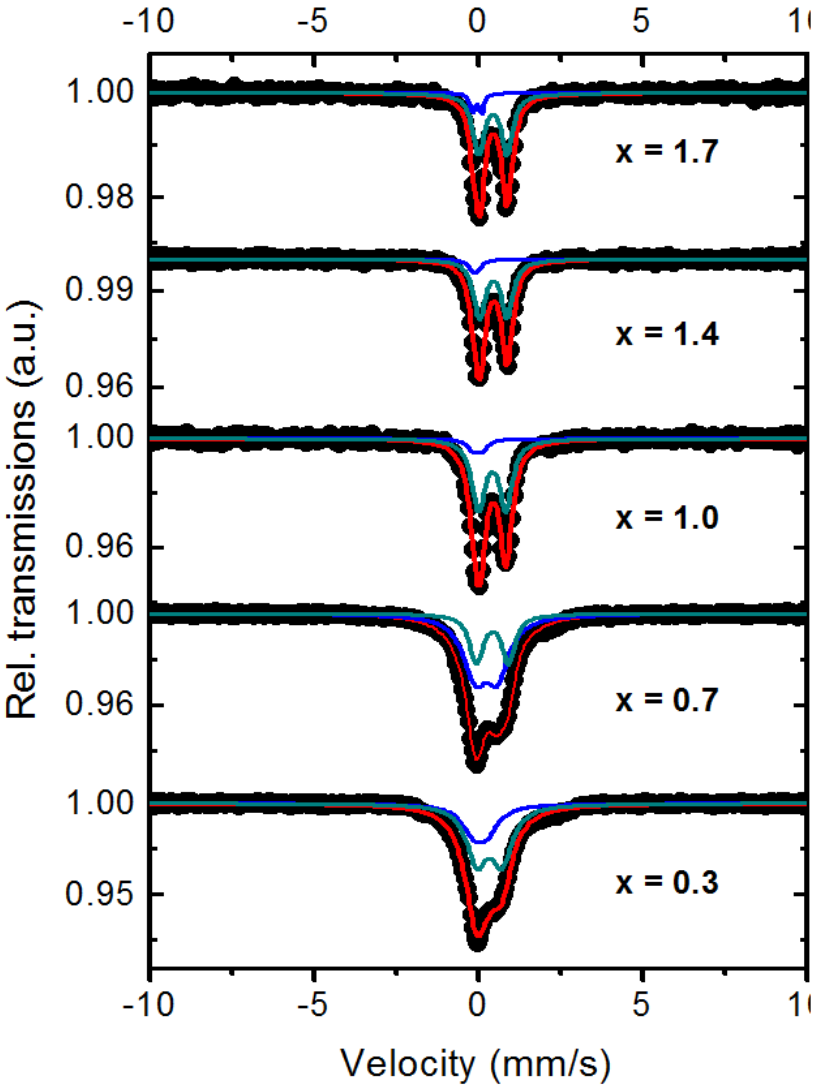

Figure 4.14. ^{57}Fe Mössbauer data and fitting for $Co_xFe_{2-x}P$ (x = 1.7, 1.4, 1, 0.7, 0.3) nanoparticles. For the samples x = 0.7 and 0.3, Γ is fixed to compensate for a Fe-containing impurity that becomes more prevalent at low x and results in unrealistic values for site occupation (see Table 4.3).

Table 4.3. Fe site occupancies (%) and fractional compositions (Fe(1) + Co(1) = Fe(2) + Co(2) = 1) for $Co_xFe_{1-x}P$ as determined from ^{57}Fe Mössbauer. The enhanced Fe content in the Fe-rich sample (x = 0.3) that gives rise to an apparent site occupancy >1.0 is due to broadening of the peak, ascribed to an impurity phase. M(1) is the tetrahedral site and M(2) the square pyramidal site. (* Indicates a fixed parameter)

Sample	δ (mm/s)	ΔE_Q (mm/s)	Γ (mm/s)	Fe site occupancy (%)	Assignment	Fe	Co
$Co_{1.7}Fe_{0.3}P$	0.05(2) 0.527(2)	0.27(2) 0.869(4)	0.17(3) 0.418(5)	4.9 95.1	M(1) M(2)	0.015 0.285	0.985 0.715
$Co_{1.4}Fe_{0.6}P$	0.05(3) 0.539(3)	0.25(6) 0.860(7)	0.32(6) 0.424(6)	8.2 91.8	M(1) M(2)	0.049 0.551	0.951 0.449
$Co_{1.0}Fe_{1.0}P$	0.04(1) 0.522(2)	0.25(1) 0.839(4)	0.44(4) 0.471(8)	11.2 88.8	M(1) M(2)	0.112 0.888	0.888 0.112
$Co_{0.7}Fe_{1.3}P$	0.24(8) 0.44(4)	0.5(2) 0.89(8)	0.73(5) 0.78*	25.5 74.5	M(1) M(2)	0.332 0.969	0.668 0.031
$Co_{0.3}Fe_{1.7}P$	0.482(5) 0.251(6)	0.88(1) 0.56(1)	0.60* 0.87*	31.6 68.4	M(1) M(2)	0.537 1.163	0.393 0

All of the nanoparticles produced here exhibit superparamagnetism below T_C and above the blocking temperature (T_B). T_B depends on the time-scale of the experiment and represents the temperature above which the oriented spins can flip during measurement due to thermal fluctuations. As such, it is a sensitive function of particle volume, extrinsic (shape) anisotropy, intrinsic (magnetocrystalline) anisotropy and T_C ($T_B<T_C$). As the particle sizes and shapes are similar for the samples presented here, the dominant effects are the magnetocrystalline anisotropy and the strength of the ferromagnetic ordering (with the latter reflected in T_C). As Co atoms do not contribute to the moment, Co-rich phases have lower T_C's and the magnetocrystalline anisotropy is diluted, as reflected in the low T_B values (30-50 K). The more Fe-rich phases have considerably higher T_B's (179-235K) reflecting in part the strength of the

ferromagnetic interactions. Thanks to the high T_C values for CoFeP and $Co_{0.7}Fe_{1.3}P$, these nanoparticles exhibit superparamagnetism at room temperature, a phenomenon commonly realized in iron oxides or metal alloys, but not (to our knowledge) previously realized in phosphides.

4.4 Conclusions

A synthetic route for $Co_xFe_{2-x}P$ nanoparticles enabling synthesis over the entire composition range as low-polydispersity samples with diameter tunability between 10-25 nm is established. The method employs CoFe alloy particles as precursors that are phosphided with TOP, and the resultant nanoparticles are hollow due to diffusion differences between the metal and phosphorus (Kirkendall effect). At intermediate x, the mechanism involves the fusion of small alloy particles into a larger particle, which then acts as a template for the further phosphidation, giving rise to particles with scalloped edges. The target composition is controlled by the initial metal precursor ratio and the size of $Co_xFe_{2-x}P$ can be tuned by varying OAm/metal ratio. The Curie temperature of $Co_xFe_{2-x}P$ nanoparticles shows a clear composition dependence that is reflective of the behavior of the bulk: it first increases and then decreases with the increase of Fe substitution. The high T_C attained in CoFeP and $Co_{0.7}Fe_{1.3}P$ render these nanoparticles superparamagnetic at room temperature enabling consideration of transition metal phosphides for applications including magnetic imaging, and therapies. The ability to control composition in $Co_xFe_{2-x}P$ is further expected to contribute to the development of phosphides for catalysis, given the promise already demonstrated by their binary end-products. Moreover, the fact that alloy particles prepared from mixed-metal

carbonyl are also amenable to conversion to oxides suggests that these,[30] and other metal alloy nanoparticles, may serve as flexible synthons for a range of nanoparticle materials beyond oxides and phosphides, including chalcogenides and heavier pnictides.

CHAPTER 5. EFFICIENT WATER OXIDATION USING COMNP NANOPARTICLES

ABSTRACT

The development of efficient water oxidation catalysts based on inexpensive and Earth-abundant materials is a prerequisite to enabling water splitting as a feasible source of alternative energy. In this work, we report the synthesis of ternary cobalt manganese phosphide nanoparticles from the solution-phase reaction of manganese and cobalt carbonyl complexes with trioctylphosphine. The CoMnP nanoparticles (*ca.* 5 nm in diameter) are nearly monodisperse and homogenous in nature. These CoMnP nanoparticles are capable of catalyzing water oxidation at an overpotential of 0.33 V with a 96% Faradaic efficiency when deposited as an ink with carbon black and Nafion. A slight decrease in activity is observed after five hundred cycles, which is ascribed to the etching of P into solution as well as the oxidation of the surface of the nanoparticles. Manganese-based ternary phosphides represent a promising new system to explore for water oxidation catalysis.

Li, D., Baydoun, H., Verani, C. N., Brock, S. L. Journal of the American Chemical Society, **2016**, 138, 4006-4009.

5.1 Introduction

Splitting water into hydrogen and oxygen represents an ideal source of clean renewable energy.[87] However, water oxidation ($2H_2O \rightarrow O_2 + 4H^+ + 4e^-$), the first step in the overall water splitting reaction, has a high activation barrier that, coupled with the need for transfer of four electrons and four protons, presents a bottleneck in the transformation of water into O_2 and H_2.

Ruthenium and iridium oxides are well-known water oxidation catalysts.[42, 43] Nevertheless, the scarcity of Ru and Ir pose serious limitations to the widespread adoption of water splitting as a green approach to renewable energy. In order to address this problem, research has focused on the synthesis of novel materials composed of stable, Earth-abundant metals capable of efficient catalytic water oxidation. Inspired by the oxygen-evolving center of Photosystem II, manganese-based materials (oxides and phosphates) have garnered considerable attention as water oxidation catalysts. [45-49]

At the same time, transition metal phosphide nanoparticles are emerging as a new class of water oxidation catalysts with reports of high activity in Ni_2P,[19, 88] CoP,[24, 25, 89-91] and CoFeP.[92, 93] While manganese-based phosphides may be natural catalyst candidates, such materials have yet to be investigated. This gap is at least in part due to a lack of synthetic methodologies for manganese phosphide nanoparticles.

This chapter describes the synthesis of nearly monodisperse ternary cobalt manganese phosphide nanoparticles from the solution-phase reaction. The catalytic OER activity of CoMnP nanoparticles is also evaluated. I performed all

the synthesis and characterization of the discussed materials. The electrochemical measurements were performed and interpreted by Habib Baydoun (the Verani Group) in the Department of Chemistry at Wayne State University and myself.

5.2 Experimental

All materials used in the synthesis of manganese based phosphide nanoparticles are given in Chapter 2.

5.2.1 Synthesis of CoMnP Nanoparticles

0.75 mmol $Co_2(CO)_8$ (0.257 g) and 0.75 mmol $Mn_2(CO)_{10}$ (0.292 g) were dissolved in 5 mL octadecene and then injected into a degassed system comprising 10.0 mL of octadecene and 1.5 mL OAm at 200 °C. After 20 min aging, TOP was injected, followed by aging at 350 °C for 3 h. The black precipitate was sonicated in hexane to remove organics bound to the surface of the nanoparticles and reprecipitated by adding excess ethanol. This sonication-precipitation cycle was done at least three times to remove as much of the bound organics as possible from the system. The isolated black powder is then dried under vacuum.

5.2.2 Synthesis of MnP Nanoparticles

MnP was synthesized by modification of a published procedure.[38] 1.5 mmol $Mn_2(CO)_{10}$ (0.584 g) was dissolved in 5 mL octadecene and then injected into a degassed system comprising 10.0 mL of octadecene and 1.5 mL OAm at 200 °C. After 20 min aging, TOP was injected, followed by aging at 350 °C for 10 h. The nanoparticles were isolated as described for CoMnP.

5.2.3 Synthesis of Co_2P Nanoparticles

Co_2P was synthesized by modification of a published procedure.[94] 1.5 mmol $Co_2(CO)_8$ (0.514 g) was dissolved in 5 mL octadecene and then injected into a degassed system comprising 10.0 mL of octadecene and 1.5 mL OAm at 200 °C. After 20 min aging, TOP was injected, followed by aging at 350 °C for 1.5 h. The nanoparticles were isolated as described for CoMnP.

5.2.4 Synthesis of $CoMnO_2$ Nanoparticles

0.75 mmol $Co_2(CO)_8$ (0.257 g) and 0.75 mmol $Mn_2(CO)_{10}$ (0.292 g) were dissolved in 5 mL octadecene and then injected into a degassed system comprising 10.0 mL of octadecene and 1.5 mL OAm at 200 °C. After 20 min aging, the system is raised to 280 °C under slow and steady air flow and maintained at that temperature for 3 h. The nanoparticles were isolated as described for CoMnP.

5.2.5 Characterization

Transmission electron microscopy (TEM), energy dispersive spectroscopy (EDS), scanning transmission microscopy (STEM) and powder X-ray diffraction (PXRD) were operated as describe in **Chapter 2**.

5.2.6 Electrochemical Characterization

Ink Preparation: The as synthesized nanoparticles (NPs, 100 mg) were mixed with Ketjen-300J carbon (C) (mass ratio, 1:1) in hexane and ultrasonicated for 30 min. The C-NPs were washed with hexane and reprecipitated by adding excess ethanol. 20 mg of C-NPs and 1 mL 5 wt% Nafion solution were dispersed in a mixture of 2 mL ethanol, 1 mL isopropanol, and 1 mL nanopure water, followed by sonicating for at least 30 min. 10 µL of the catalyst ink was deposited on the glass carbon working electrode (loading: 0.284 mg/cm^2) and dried at room temperature.

Electrochemical Measurements: An EC epsilon potentiostat equipped with an RDE2 rotating disc electrode was used to record all the cyclic voltammograms. In a typical experiment a standard three electrode setup was employed using an Ag/AgCl reference electrode, a Pt wire auxiliary electrode, and a glassy carbon working electrode (surface area = 0.07 cm^2) using a 1 $mol \cdot L^{-1}$ KOH solution as the solvent. The surface of the glassy carbon electrode was modified by depositing 10 µL of nanoparticle ink onto the surface and followed by drying under an infrared heat lamp for five minutes. The cyclic voltammograms were measured at a scan rate of 10 mV/S and 1600 rpm. The potentials were measured versus Ag/AgCl and converted to the reversible hydrogen electrode (RHE) by using **equation 5.1**. The resistivity of the solution was determined using the iR compensation feature of the epsilon software and corrections were performed manually according to **equation 5.2**.

$$E_{RHE} = E_{Ag/AgCl} + 0.197 + 0.059*pH \qquad \text{Equation 5.1}$$

$$E_{RHE} = E_{Ag/AgCl} + 0.197 + 0.059*pH - iR \qquad \text{Equation 5.2}$$

5.3 Results and Discussion

We have previously reported the synthesis of MnP nanoparticles.[38] However, attempts to use these particles as water oxidation catalysts revealed that MnP is not stable under oxidizing conditions, which we attribute to the highly oxophilic nature of manganese. As shown in **Figure 5.1**, the presence of a broad irreversible preoxidation peak at ~1.4 V_{RHE} is observed in the first oxidation sweep. The following sweeps revealed a large drop in the current density consistent with an irreversible oxidative transformation of MnP during water oxidation. Accordingly,

we sought to moderate the activity of Mn by the inclusion of a second metal, namely, cobalt.

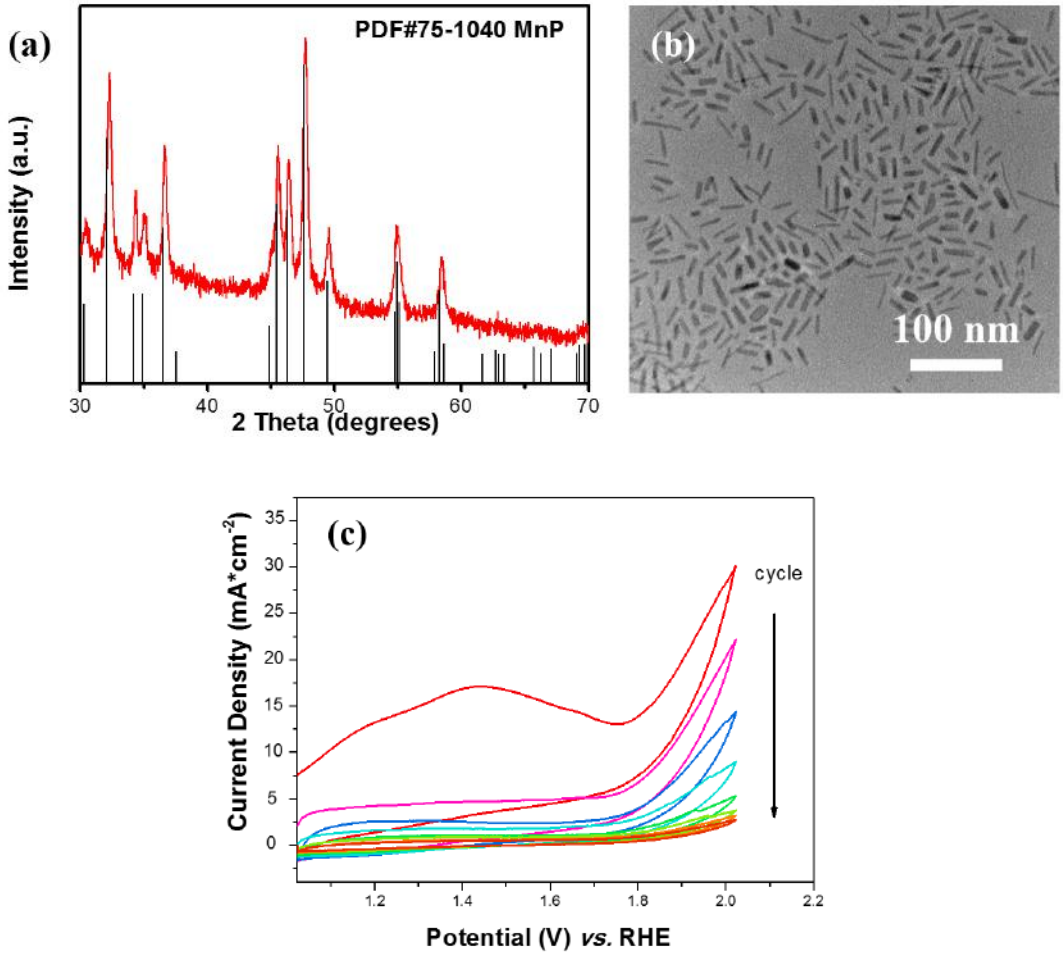

Figure 5.1. (a) Powder XRD pattern and (b) TEM image of MnP nanorods; (c) CV scans of MnP measured in 1 M KOH with a sweep rate of 10 mV s^{-1}. The reference XRD pattern for MnP (PDF # 75-1040) is shown in panel (a).

5.3.1 Synthesis and Characterization of CoMnP Nanoparticles

The initial target of our investigation was the phase $Co_{0.5}Mn_{0.5}P$, which we expected to be feasibly attained as discrete nanoparticles based on the facts that (1) MnP and CoP are isostructural and (2) it is possible to synthesize the entire solid solution by solid-state methods in the bulk phase.[95-97] Adapting known methods for MnP and CoP nanoparticle synthesis, $Co_2(CO)_8$ and $Mn_2(CO)_{10}$ were

injected into a solution of hot 1-octadecene and oleylamine, followed by injection of trioctylphosphine (TOP) and elevation of the solution temperature to 350 °C. However, the X-ray diffraction (XRD) pattern of the product showed that the peaks correspond to orthorhombic CoMnP and not the expected $Co_{0.5}Mn_{0.5}P$ phase (**Figure 5.2a**). Intriguingly, we have not been successful preparing the Mn_2P phase (the Mn end-product of $Co_{1-x}Mn_xP$); producing only MnP or no isolable product. We hypothesize that incorporating Co favors the inclusion of low-valent Mn, thus facilitating the formation of the "M_2P" phase. Transmission electron microscopy (TEM) images reveal the formation of spherical nanoparticles with an average diameter of 4.59 ± 0.76 nm (**Figure 5.2b, c**). The corresponding energy dispersive X-ray spectrum indicates that the atomic ratio of Co, Mn and P is close to 1:1:1.3. The composition of the nanoparticles was further confirmed from ICP-MS measurements which show a ratio of Co:Mn:P of 1:1:1.1. The slight excess of P is attributed to the presence of residual TOP as surface binding groups.

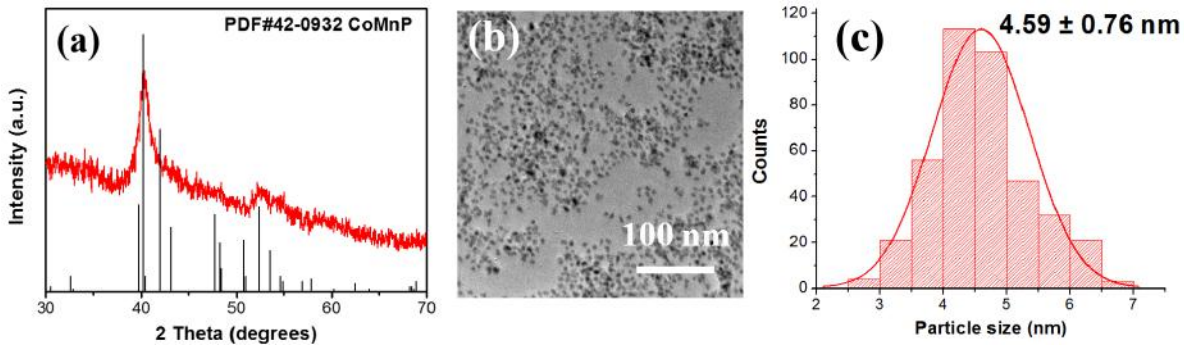

Figure 5.2. Powder XRD (a) and TEM (b) of CoMnP nanoparticles. The reference pattern for CoMnP (PDF # 42-0932) is shown. (c) Histogram for the particle size distribution (measured from TEM) for CoMnP nanoparticles.

The homogenous nature of the synthesized nanoparticles was verified by performing scanning transmission electron microscopy (STEM) measurements

combined with elemental mapping and line scans (**Figure 5.3**). The data show that Co, Mn and P are homogeneously distributed within the nanoparticles, thus suggesting the formation of a solid solution.

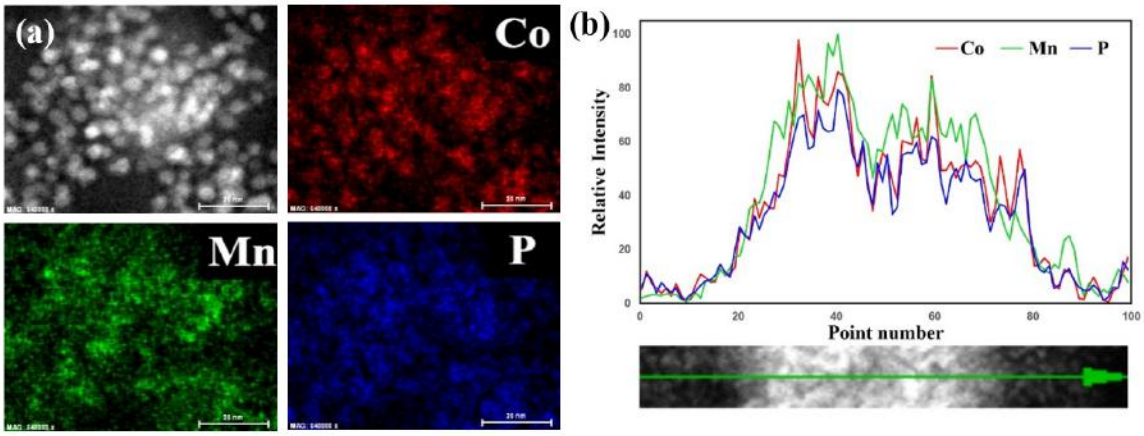

Figure 5.3. STEM image and elemental mapping data (a), and line scan compositional data (b) of CoMnP nanoparticles. Co is shown in red, Mn in green, and P in blue.

5.3.2 Water Oxidation Catalysis

Based on prior work with CoFeP, which exhibits higher activity than the corresponding ternary oxide or the binary Co or Fe phosphide materials,[92] $CoMnO_2$ and Co_2P nanoparticles were prepared for comparison to CoMnP (loading: 0.284 mg/cm^2, **Figure 5.4**). The catalytic behavior of the different nanoparticles was determined by preparing an ink composed of the nanoparticles, carbon black and Nafion. The overpotential, defined as the potential by which the current density reaches 10 mA/cm^2, is commonly used as a figure of merit for heterogeneous water oxidation catalysts.[42, 98] For CoMnP the overpotential was 0.33 V at a current density of 10 mA/cm^2 (**Figure 5.5**). This overpotential places this CoMnP catalyst among the top tier of water oxidation catalysts, and on par with iridium oxide (**APPENDIX A, Table A1**).[19, 24, 25, 42, 49, 88-90, 92, 93, 99, 100] For comparison, Co_2P

nanoparticles showed a higher overpotential of 0.37 V and the overpotential of $CoMnO_2$ was higher still at 0.39 V. The Tafel plots in **Figure 5.5b** are derived from the polarization curves and they show the plots of overpotential *vs.* the log of the current density. While $CoMnO_2$ and Co_2P have a Tafel slope of 95 and 128 mV/dec, respectively; CoMnP has a slope of 61 mV/dec, close to the ideal value of 59 mV/dec (equivalent to 2.3 x RT/F) associated with a one-electron transfer prior to the rate-limiting step.[101, 102]

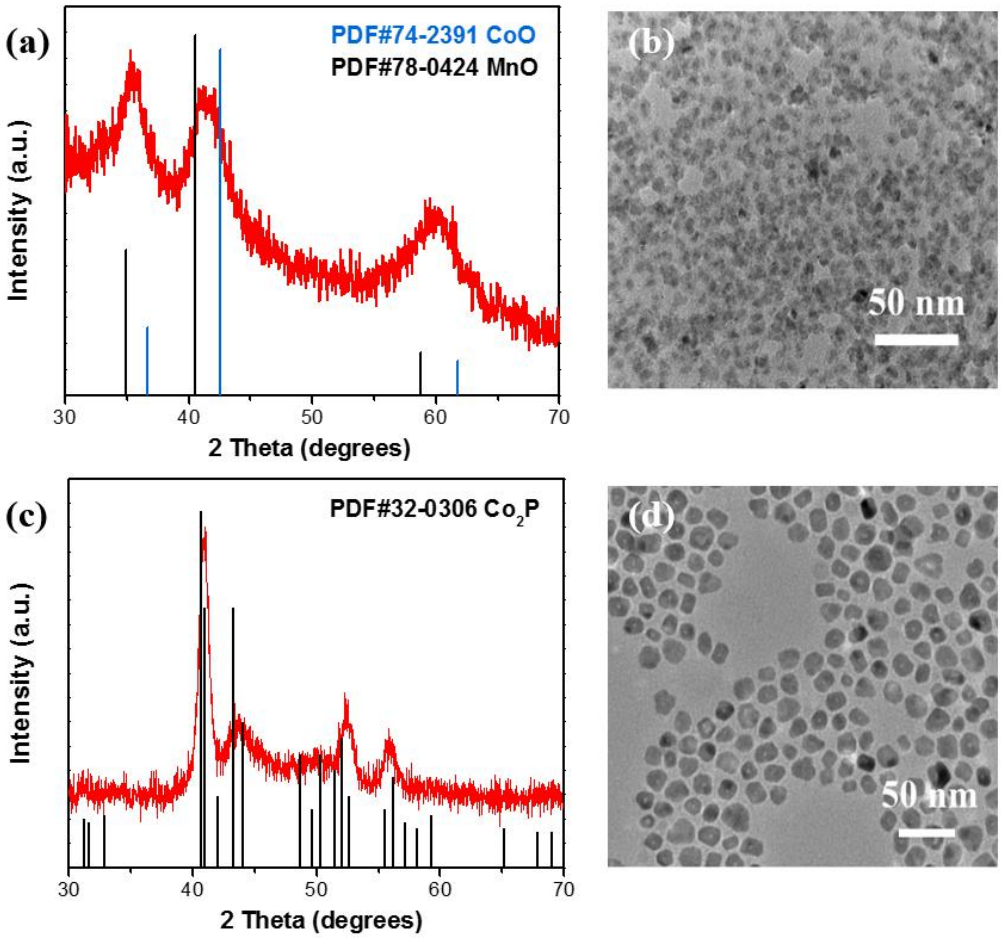

Figure 5.4. (a), (c) Powder XRD patterns and (b), (d) TEM images of $CoMnO_2$ and Co_2P nanoparticles, respectively.

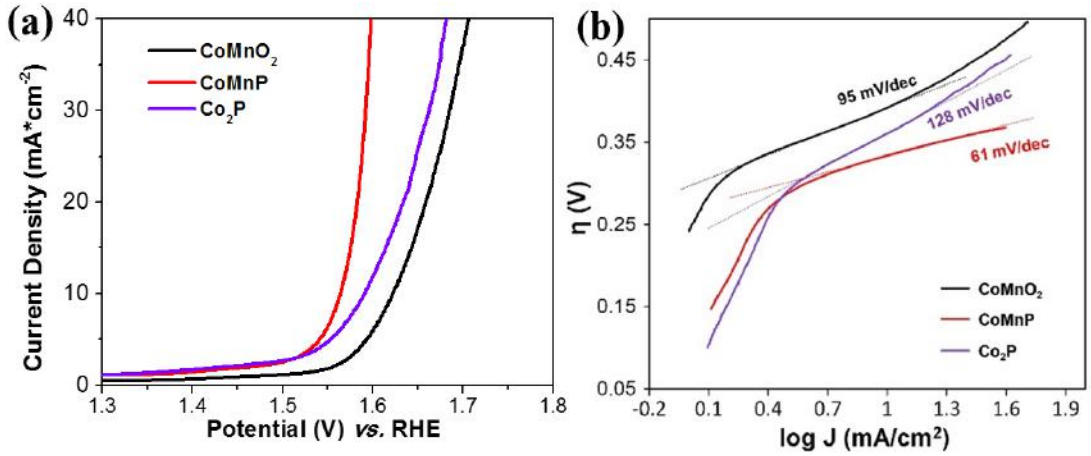

Figure 5.5. (a) Polarization curves for nanoparticles of CoMnP, $CoMnO_2$ and Co_2P in 1.0 M KOH; (b) Tafel plots derived from the polarization curves.

The decrease in overpotential for CoMnP relative to Co_2P is associated with synergism between the two metal centers. It has been suggested that the insertion of a second metal may help lower the thermodynamic barrier of a proton-coupled electron transfer (PCET) pre-equilibrium while facilitating O-O bond formation, leading to enhanced catalytic activity.[101] Most proposed mechanisms for CoO_x species suggest the need to form vicinal high-valent oxo species.[101, 103-105] While the formation of Co=O is energetically demanding and the product is unstable, the formation of Mn=O species is relatively facile.[106] As such it is expected that the presence of an Mn center in close proximity to a Co center would lower the activation barrier needed for catalysis, thus explaining the decrease in overpotential in CoMnP compared to Co_2P. Likewise, we posit that the high oxophilicity of Mn is moderated by Co, facilitating catalyst turnover. The lower activation barrier of phosphides over oxides is likely due to the intrinsic electric conductivity of the phosphides relative to corresponding oxides. The consequence of these reaction barrier variations appears to be distinct mechanisms in the three

materials, as reflected in the widely different Tafel slopes. Further investigation will be necessary to ascertain the validity of these suggestions.

The Faradaic efficiency was determined by performing a controlled potential electrolysis (CPE) experiment using an airtight H-type cell, and analyzing the head space gas by gas chromatography (**Figure 5.6**). The experimentally determined oxygen quantity was compared to the expected amount of oxygen based on the charge consumed. The Faradaic efficiency reached 96 % after ten hours of catalysis.

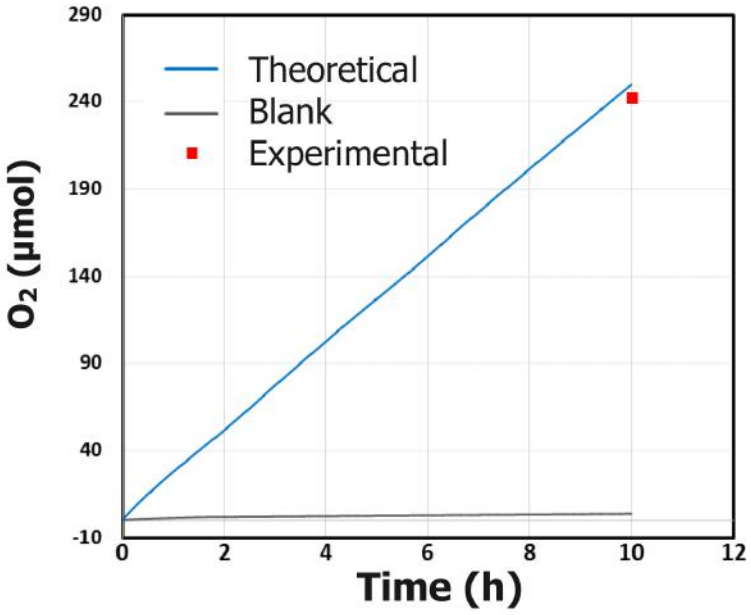

Figure 5.6. Faradaic efficiency: experimental vs. theoretical amount of O_2 produced.

The stability of the materials under catalytic conditions was determined by collecting polarization curves between 1.03 and 2.23 V (vs RHE) over 500 cycles. Upon cycling, an increase in the overpotential was observed from 0.33 to 0.37 V (**Figure 5.7**). Interestingly, after intermediate cycling (200 cycles) the overpotential increased to 0.35 V, which was accompanied by a nominal increase in the Tafel

slope (**Figure 5.7**, inset). However, after continued cycling (**Figure 5.7**) the Tafel slope increased to 76 mV/dec. These observations suggest that as the catalyst is cycled, the nature of the catalyst, and consequently the mechanism of operation, is changing.

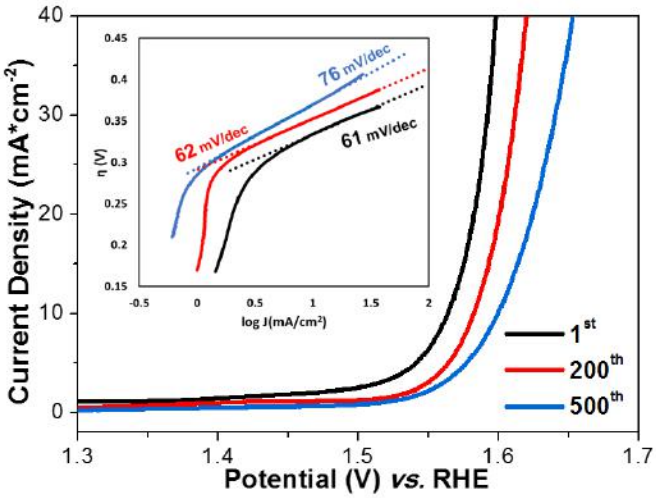

Figure 5.7. Polarization curves for CoMnP nanoparticles, in 1.0 M KOH initially (black), after 200 (red) and 500 CV sweeps (blue) vs. RHE. Inset: Tafel plots derived from the cycling experiments.

In an effort to understand the deactivation, we performed X-ray photoelectron spectroscopy (XPS) analysis on the samples before and after a ten-hour CPE experiment (**Figure 5.8**). Before catalysis the high resolution XPS spectrum of Co ($2p_{3/2}$) comprises a peak at 777.8 eV assigned to the binding energy of Co in Co_2P,[107] the Co^{2+} peaks at 780.9 eV, as well as a satellite peak (787.1 eV), corresponding to CoO, which presumably formed due to surface oxidation. The XPS spectrum of Mn ($2p_{3/2}$) exhibited a peak at 641.0 eV, corresponding to oxidized manganese species such as MnO or Mn_2O_3. The absence of low-valent Mn peaks in the spectrum is attributed to the high oxophicility of Mn, resulting in surface oxide formation.[72] The XPS spectrum of P ($2p_{3/2}$) showed two peaks

assigned to phosphide at 129.7 eV and phosphate or phosphite (PO_x or P-O species) at 133.4 eV. In contrast, the high-resolution XPS patterns of Co, Mn, and P after catalytic cycling show the disappearance of low energy peaks of Co (777.8 eV) and P (129.7 eV), as well as a shift towards higher binding energies for Mn (from 641.0 eV to 641.9 eV). These observations are in accordance with nanoparticle surface oxidation during the catalytic process to form MPO_x and MO_x species and are in line with a recent report in which Ni_2P nanomaterials were oxidized during the course of the water oxidation reaction to form NiO_x and phosphate species.[19, 88] Moreover, the P signal after catalytic cycling appears very weak (barely discernible above the noise, **Figure 5.8**), suggesting that the surface-bound phosphates are being etched. In order to probe the possibility of leaching during catalysis ICP-MS analysis was performed on a solution following a fifteen-hour CPE experiment (**Figure 5.9**, **Table 5.1**). The results show the presence of Co, Mn, and P in solution with a ratio of 1:7:234 thus suggesting that P is leaching into solution at a significant rate, whereas metal leaching is marginal, with Mn dominating Co. Because surface-bound phosphates have been reported to mediate water oxidation *via* proton-coupled electron transfer,[46] the loss of surface phosphate combined with metal oxidation may account for the decrease in activity and shift in the mechanism.

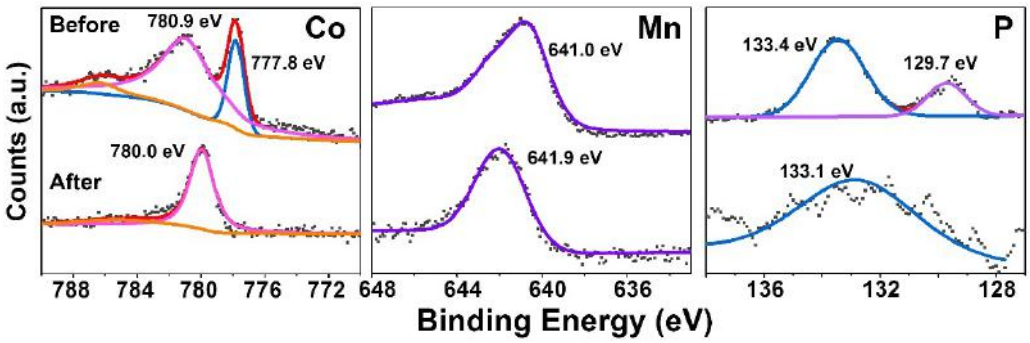

Figure 5.8. High-resolution XPS patterns for CoMnP nanoparticles before (top) and after (bottom) electrolysis for 10 h: (a) Co ($2p_{3/2}$), (b) Mn ($2p_{3/2}$), and (c) P ($2p_{3/2}$).

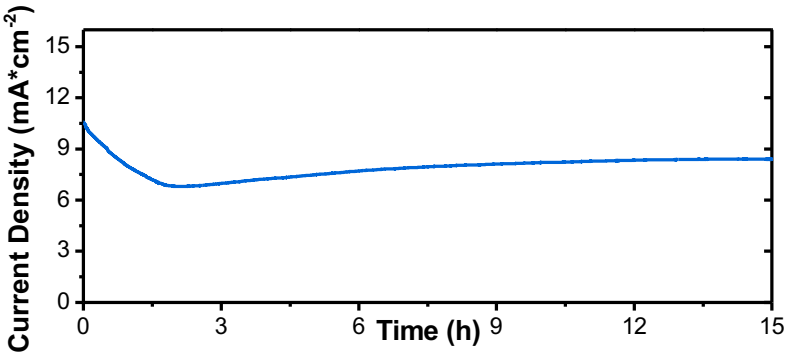

Figure 5.9. High-resolution XPS patterns for CoMnP nanoparticles before (top) and after (bottom) electrolysis for 10 h: (a) Co ($2p_{3/2}$), (b) Mn ($2p_{3/2}$), and (c) P ($2p_{3/2}$).

Table 5.1. ICP-MS data of solution before and after a fifteen-hour CPE experiment.

Element	Before (5 h soak) Concentration (ppb)	After CPE Concentration (ppb)	After CPE (Mole ratio x : Co)
P K	2.26	327.39	234
Mn K	0.01	17.32	7
Co K	0.13	2.66	1

5.4 Conclusions

We have reported the successful synthesis of homogenous, nearly monodisperse CoMnP nanoparticles. This new material is an active and efficient

water oxidation catalyst that can operate at an overpotential of 0.33 V and 96% Faradaic efficiency. After five hundred cycles, the overpotential for catalysis increased to 0.37 V, likely due to surface oxidation and phosphorus etching from the nanoparticles. In addition, the TEM images, PXRD patterns, and compositional dependent electrocatalytic oxygen evolution properties of $Co_{2-x}Mn_xP$ nanoparticles are included in **Appendix B**.

CHAPTER 6. BOOSTING THE CATAYTIC PERFORMANCE OF IRON PHOSPHIDE NANORODS FOR THE OXYGEN EVOLUTION REACTION BY INCORPORATION OF MANGANESE

ABSTRACT

The lack of efficient and stable oxygen evolution reaction (OER) catalysts comprising inexpensive Earth-abundant materials limits the viability of water splitting as a clean and renewable source of energy. In this work, we report the synthesis of homogenous ternary $Fe_{2-x}Mn_xP$ nanorods with control of Mn incorporation ($0 \leq x \leq 0.9$) from the solution-phase reaction of manganese and iron carbonyl complexes with trioctylphosphine. The OER activity of $Fe_{2-x}Mn_xP$ nanorods dramatically increases with the incorporation of Mn (overpotential as low as 0.44V at 10 mA/cm^2 for $x = 0.9$) and the overpotential can be further decreased (by nearly 0.1 V) by post-deposition annealing. The enhanced OER activity and stability, along with the abundance and availability of Fe and Mn, make bimetallic manganese-iron phosphides a promising class of materials for more cost-effective and efficient water oxidation catalysis.

Li, D., Baydoun, H., Kulikowski, B., Brock, S. L. Chemistry of Materials, **2017**, 29, 3048-3054.

6.1 Introduction

Due to the high activation barrier and the need to transfer four electrons and four protons, the oxygen evolution reaction (OER) is considered to be the rate limiting step for the entire water splitting reaction. Therefore, the development of efficient materials capable of catalyzing the OER remains one of the major hurdles to overcome before water splitting can be utilized as a practical source of renewable energy.[87, 108] Some of the more efficient OER catalysts are based on noble metals such as iridium and ruthenium.[42, 109, 110] However, as a result of the scarcity and the expense of these metals, recent efforts have focused on the development of catalysts based on Earth-abundant metals.

Transition metal phosphide nanoparticles are emerging as a new class of water oxidation catalysts with reports of high activity in binary metal phosphides such as Ni_2P,[18-20] Co_2P,[21, 22] and CoP.[23-25] Recently, the ternary metal phosphides CoFeP, NiCoP, and NiFeP have shown improved OER activity over the binary phases (Co_2P, Fe_2P or Ni_2P), attributed to synergism between the two metals.[22, 26-29] Inspired by the oxygen-evolving tetra-manganese cluster of Photosystem II, manganese-based materials such as oxides and phosphates have been studied for water oxidation in both neutral and alkaline solution.[48, 111] Naturally, the interest in manganese-based materials has moved to phosphides. Our group reported CoMnP nanoparticles as efficient water oxidation catalysts, demonstrating a decrease in overpotential from 0.37 for Co_2P to 0.33 V (at 10 mA/cm^2) for CoMnP (**Chapter 5**).[112] However, after prolonged stability testing, the overpotential of CoMnP was observed to increase to 0.37 V, correlated to surface oxidation and

phosphorus etching from the nanoparticles. Here we investigate the synergism between Fe and Mn in $Fe_{2-x}Mn_xP$ towards oxygen evolution catalysis with an eye to enhance stability without compromising activity. Notably, due to the abundance and availability of Fe and Mn compared to Ir, Ru or even Co, catalyst preparation becomes more cost-effective.

While the $Fe_{2-x}Mn_xP$ bulk materials have been widely studied as potential functional magnetocaloric materials,[50-53] only one report has emerged on the synthesis of nanoscale FeMnP. Whitmire and coworkers reported a synthesis of Fe-rich $Fe_{2-x}Mn_xP$ nanoparticles using $FeMn(CO)_8(\mu\text{-}PH_2)$ as a single-source molecular precursor.[113] However, the need to prepare the single molecule precursor increased the complexity of this synthesis and Mn incorporation was limited and unpredictable. The potential of nanoscale $Fe_{2-x}Mn_xP$ for catalytic processes, such as water splitting, emphasizes the need for a protocol that enables access to more Mn-rich phases and with greater control over final product composition.

The synthesis and characterization of $Fe_{2-x}Mn_xP$ nanorods were carried out by myself and an undergraduate student I mentored, Bogdan Kulikowsiki at Wayne State University. The electrochemical measurements were performed and interpreted by Habib Baydoun (the Verani Group) in the Department of Chemistry at Wayne State University and myself.

6.2 Experimental

All materials used in the synthesis of manganese based phosphide nanoparticles are given in Chapter 2.

6.2.1 Synthesis of Fe_2P nanorods

$Fe(CO)_5$ (2 mmol) was dissolved in 5 mL TOP at 90 °C for 1 h. At the same time, 10.0 mL of oleylamine was placed in a 200 mL Schlenk flask with a condenser. The system was degassed at 120 °C for 20 min to remove any moisture or oxygen, followed by purging with argon for 30 min. The temperature was then increased to 320 °C and the mixture of iron carbonyl in TOP was injected into the system. The system was maintained at 320 °C for 2 h and cooled down naturally. The black precipitate was sonicated in hexane and reprecipitated with ethanol. This sonication-precipitation cycle was done at least two times to remove as much the bound organics as possible from the system. The isolated black powder was then dried under vacuum.

6.2.2 Synthesis of $Fe_{2-x}Mn_xP$ nanorods ($x \leq 0.7$)

A mixture of $Fe(CO)_5$ (1.5 mmol) and $Mn_2(CO)_{10}$ (1.25 mmol Fe/Mn = 0.75/1.25) was dissolved in 5 mL TOP at 90 °C for 1 h. At the same time, 10.0 mL of oleylamine was placed in a 200 mL Schlenk flask with a condenser. The system was degassed at 120 °C for 20 min to remove any moisture or oxygen, followed by purging with argon for 30 min. The temperature was then increased to 320 °C and the mixture of metal carbonyls in TOP was injected into the system. The system was maintained at 320 °C for y ($0.5 \leq y \leq 10$) h and cooled down naturally. Specific values of y are indicated in **Table 6.1**. The product was isolated as described for Fe_2P. For a fixed reaction time of 2 h, ratios of Fe/Mn were changed to values indicated in **Table 6.2**.

6.2.3 Synthesis of $Fe_{1.1}Mn_{0.9}P$ nanorods

The synthesis was performed as described above, except after 3 h, a second mixture of $Mn_2(CO)_{10}$ (0.77 mmol) and TOP (3 mL) was injected. The system was maintained at 320 °C for another 2 hours. Isolation of nanorods was performed as described previously.

6.2.4 Size selective isolation process

To separate the nanorods from small, spherical MnO nanoparticles evident in 10 h samples, the product was dispersed in hexane and centrifuged. The supernatant containing MnO nanoparticles was discarded.

6.2.5 Post-deposition annealing

Carbon-nanorods (mass ratio, 1:1) were dried under vacuum and then in a furnace under active flow of 5% H_2/Ar at 673 K for 1 h.

6.2.6 Characterization

Transmission electron microscopy (TEM), energy dispersive spectroscopy (EDS), scanning transmission microscopy (STEM) and powder X-ray diffraction (PXRD) were operated as describe in **Chapter 2**.

6.2.7 Electrochemical measurements

All electrochemical measurements operated in this section are same as described in **section 5.2.4**.

6.3 Results and Discussion

Despite our inability to access Mn_2P as discrete, crystalline nanoparticles by arrested precipitation reaction,[20, 37, 114] we found that up to 45% Mn can be incorporated into Fe_2P ($Fe_{1.1}Mn_{0.9}P$) by a single-pot solution-phase synthesis. The discrete, uniform $Fe_{2-x}Mn_xP$ nanorods ($0 \leq x \leq 0.9$) were evaluated as OER

catalysts and the activity was found to dramatically increase with the incorporation of Mn into the system. Notably, the overpotential can be further decreased (by nearly 0.1 V) by post-deposition annealing.

6.3.1 Synthesis and Characterization of $Fe_{2-x}Mn_xP$ Nanorods ($x \leq 0.7$)

Initially, the more Mn-rich end of the phase diagram was targeted, $Fe_{0.75}Mn_{1.25}P$. A mixture of dimanganese decacarbonyl (1.25 mmol), iron pentacarbonyl (0.75 mmol), and trioctylphosphine (TOP) was injected into a degassed system of oleylamine (OAm) at 325 °C. Within a few seconds, the solution changed from orange to black, indicating the start of nucleation. After maintaining the solution at 325 °C for 2 hours, the solution was cooled to room temperature and the final product was isolated by dispersing in hexane and precipitating with ethanol. Transmission electron microscopy (TEM) (**Figure 6.1a**) indicated the sample consisted of rod-shape particles with a composition determined by the energy-dispersive X-ray spectroscopy (EDS) and inductively coupled plasma-mass spectrometry (ICP-MS) to be $Fe_{1.5}Mn_{0.5}P$ (**Table 6.1**, 2h), suggesting Mn incorporation is limited. The average length of the rods was 74.7 ± 10.0 nm and the average width was 5.5 ± 0.4 nm (**Figure 6.2**, 2h). High-resolution TEM (HRTEM) images (**Figure 6.1b**) of single rods revealed them to be single crystalline, exhibiting lattice fringes of 1.73 and 2.24 Å, corresponding to the (002) and (111) planes of hexagonal Fe_2P (**Figure 6.1d**), respectively. The orientation of these fringes relative to the long axis, along with the sharpness of PXRD reflections with *l* components relative to *hk0* reflections, suggests that the nanorods grow along the *c* direction (**Figure 6.1d** and **e**). The high angle annular

dark field (HAADF) image (**Figure 6.1c**) is consistent with highly-crystalline products, as evidenced by high diffraction contrast. Elemental mapping data for these $Fe_{1.5}Mn_{0.5}P$ nanorods are consistent with solid solution formation (**Figure 6.1f**); the three elements (Fe, Mn, and P) are homogeneously distributed within each rod, suggesting phase segregation is not occurring.

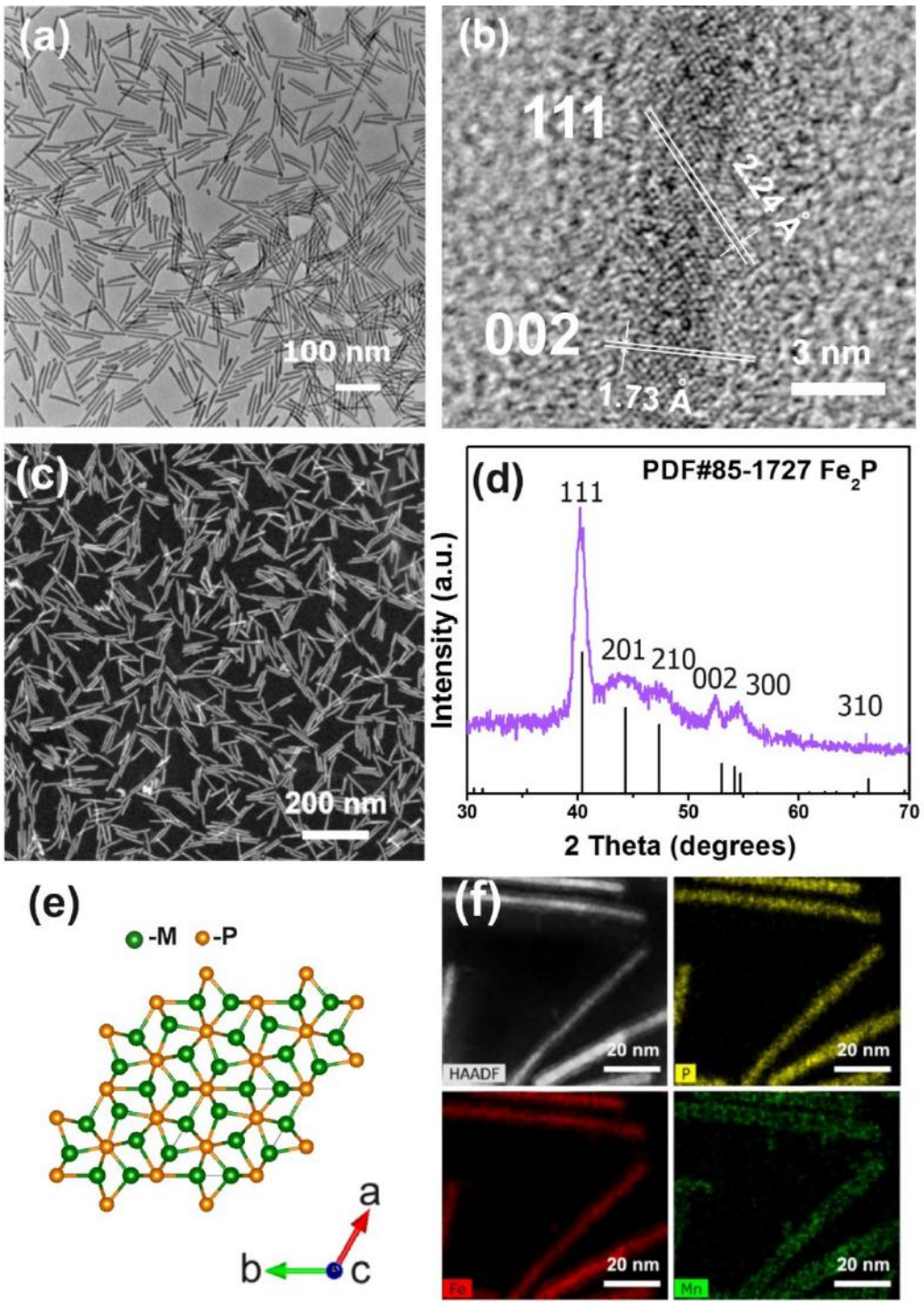

Figure 6.1. (a) TEM image, (b) HR-TEM image showing lattice fringes attributed to (111) and (002) planes, (c) HAADF image (d) PXRD pattern and (f) HAADF image and its corresponding STEM elemental mapping data of $Fe_{1.5}Mn_{0.5}P$ nanorods obtained from targeting the composition $Fe_{0.75}Mn_{1.25}P$ at a 2 h reaction time. (e) Top-down view of the Fe_2P (002) surface.

Table 6.1. Target compositions and product compositions (from EDS) of $Fe_{2-x}Mn_xP$ nanoparticles after 2 h reaction.

Reaction time (h)	Actual ratio from EDS (Mn : Fe)	Actual ratio from ICP (Mn : Fe)
0.5	0.21 : 1.79	0.20 : 1.80
1	0.31 : 1.69	0.32 : 1.68
2	0.48 : 1.52	0.49 : 1.51
3	0.70 : 1.30	0.71 : 1.29
6	0.71 : 1.29	0.73 : 1.27
10	0.69 : 1.31	0.71 : 1.29
5 (2^{nd} injection)	0.92 : 1.08	0.91 : 1.09

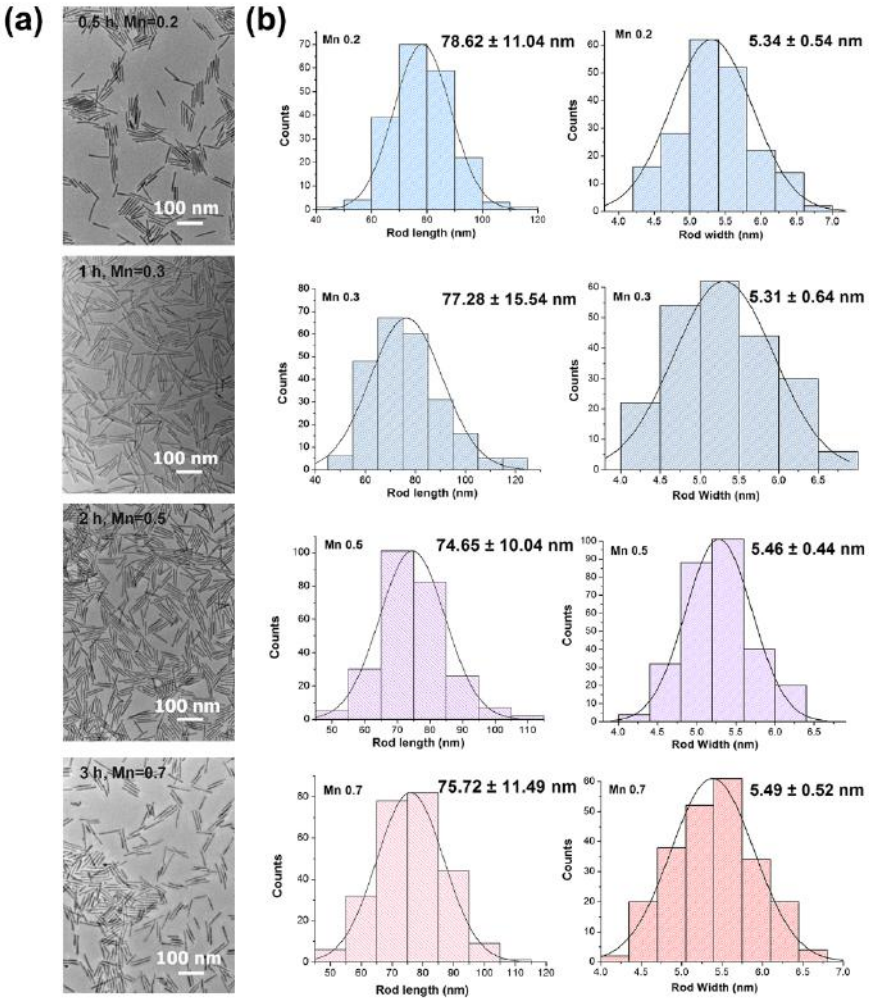

Figure 6.2. (a) TEM images of $Fe_{2-x}Mn_xP$ nanorods as a function of time (targeted ratio Fe/Mn = 0.75/1.25). (b) Histograms for the rod length and width distribution (measured from TEM) for different compositions of $Fe_{2-x}Mn_xP$. The Mn composition indicated was determined by ICP-MS (Table 6.1).

In an attempt to augment Mn incorporation, the initial ratio of Fe/Mn was decreased from 0.75/1.25 to 0.5/1.5, but only a marginal increase in Mn uptake was obtained (**Table 6.2**). Indeed, for a range of ratios evaluated, the Mn incorporation did not exceed 40% of the target (**Table 6.2**). The Whitmire group observed the same phenomenon, and suggested preferential removal of manganese atoms by solvent was occurring.[113] Intriguingly, when only injecting $Mn_2(CO)_{10}$ into the system, it takes nearly 3 hours for the solution to change color from yellow to black, indicating a slow reaction rate for manganese alone with phosphorus. Thus, we hypothesized that after injecting a mixed metal precursor into the solution, the majority of the manganese monomer may still remain in the solution, and manganese monomer incorporation into the rods would increase as a function of time.

Table 6.2. Target compositions and product compositions (from EDS) of $Fe_{2-x}Mn_xP$ nanoparticles after 2 h reaction.

Starting ratio (Mn : Fe)	Actual ratio from EDS (Mn : Fe)
1.0 : 1.0	0.36 : 1.64
1.25 : 0.75	0.48 : 1.52
1.4 : 0.6	0.48 : 1.52
1.5 : 0.5	0.55 : 1.45

In order to determine the validity of this hypothesis, we isolated and characterized the product using the same initial metal precursor ratio (Fe/ Mn = 0.75/ 1.25, x = 1.25) but at different reaction times (t = 0.5, 1, 2, 3, 6, and 10 h). TEM images show that these nanorods have similar sizes (**Figure 6.2**), but the composition varies from x = 0.2 to x = 0.7 when the reaction time is increased from

0.5 to 3 h (**Figure 6.3a**), thus indicating the incorporation of Mn into nanorods is increasing with time. Nonetheless, when the reaction time increases beyond 3 h, the Mn incorporation does not increase further but remains saturated. The fate of the excess Mn is discerned by TEM and XRD of the 10 h product, which indicates that small, spherical MnO nanoparticles are being formed along with $Fe_{2-x}Mn_xP$ nanorods (**Figure 6.4a** and **b**). The XRD peaks corresponding to MnO, as well as the spherical nanoparticles, disappear after size-selective precipitation leaving $Fe_{1.3}Mn_{0.7}P$ nanorods as single–phase product (**Figure 6.4b** and **c**). As we ascertained above, the majority of manganese monomers remain in solution and the quantity that incorporates into the rods can be increased as a function of time. However, because of the highly oxophilic nature of manganese, some manganese monomers may react with adventitious oxygen in the system to form oxide,[58] which cannot be converted into phosphide.[115] Thus saturation is attributed to competition between manganese incorporation and manganese oxidation, with the latter serving to remove monomers from the reaction.

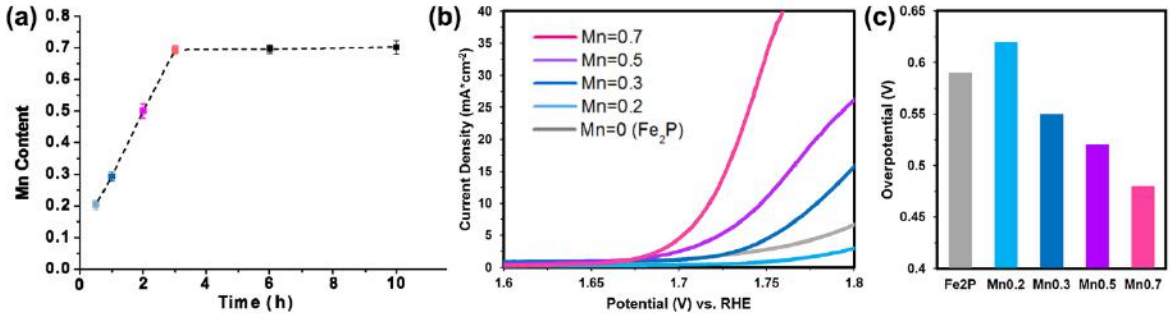

Figure 6.3. (a) Mn uptake in $Fe_{2-x}Mn_xP$ as a function of reaction time; (b) polarization curves as a function of composition, x, in 1.0 M KOH; (c) overpotentials required at j = 10 mA/cm^2.

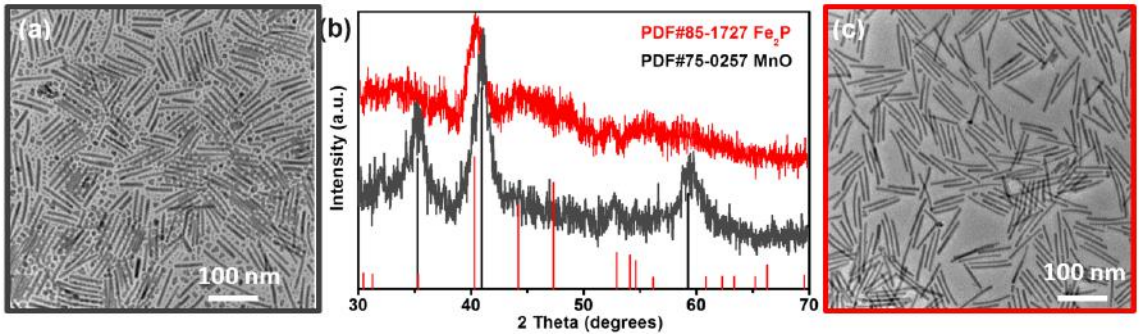

Figure 6.4. (a) TEM image and (b) PXRD pattern of the product after 10 h reaction (grey) and the product after size-selective precipitation (red). (c) TEM image of the product after size-selective precipitation to remove the small, spherical MnO nanoparticles.

The incorporation of Mn is reflected in the PXRD patterns (**Figure 6.5**) where peaks (most obviously, the (111)) shift to lower 2θ with increasing Mn content, reflecting the larger size of Mn relative to Fe. Intriguingly, the structure in all cases appears to be hexagonal Fe_2P-type, despite the fact that the crystal structure of bulk $Fe_{2-x}Mn_xP$ adopts an orthorhombic structure in the range $0.62 \leq x \leq 1.24$ (and the hexagonal Fe_2P-type structure for all other x).[53] We compared simulated orthorhombic and hexagonal structures to the observed diffraction pattern for the x = 0.7 phase (**Figure 6.6**) and the latter appears to be a better match. Thus, consistent with what the Whitmire group reported,[113] nanoscale $Fe_{1.3}Mn_{0.7}P$ adopts a metastable structure. This is likely due to the relatively gentle methods, such as the low reaction temperature, or more active precursors used.[116-120]

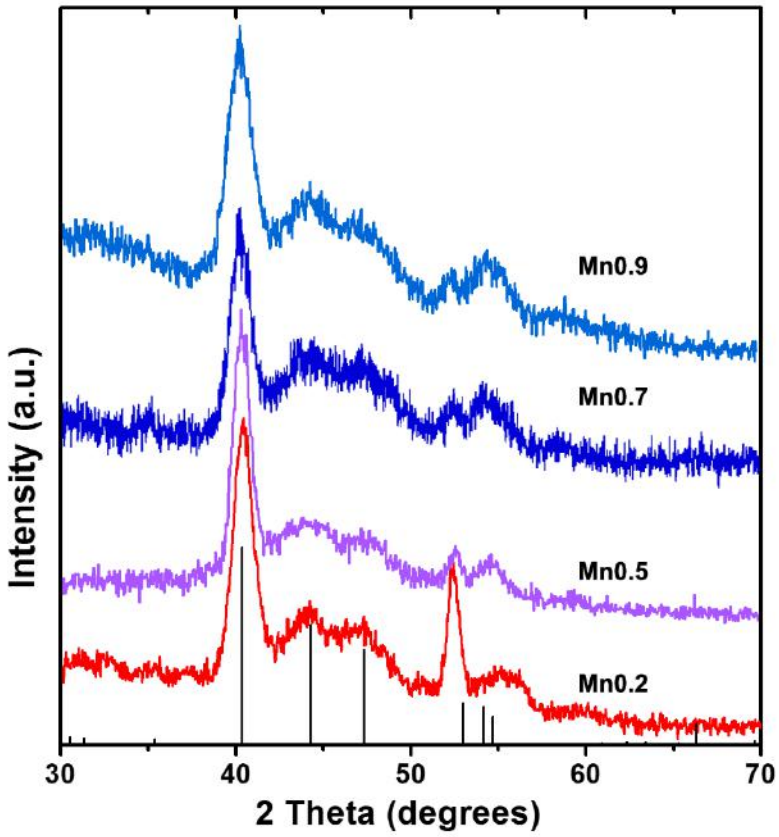

Figure 6.5. PXRD pattern of different compositions of $Fe_{2-x}Mn_xP$ nanorods, revealing a shift in the (111) reflection (ca 40° 2θ) to lower angle with increasing x.

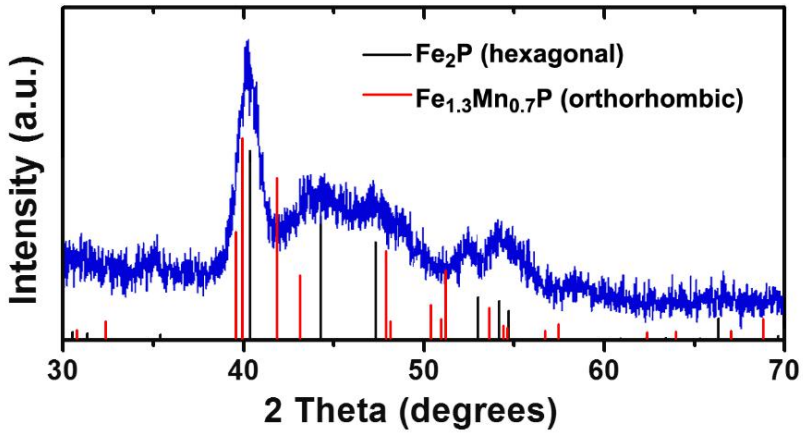

Figure 6.6. PXRD pattern of $Fe_{1.3}Mn_{0.7}P$ nanorods. Reference patterns are for hexagonal Fe_2P (PDF # 85-1727) and orthorhombic $Fe_{1.3}Mn_{0.7}P$ (simulated).[54]

6.3.2 Electrocatalytic Water Oxidation by $Fe_{2-x}Mn_xP$ Nanorods ($x \leq 0.7$)

The catalytic behavior of the synthesized materials towards OER in an alkaline medium was tested by preparing an ink containing the as-prepared $Fe_{2-x}Mn_xP$ nanorods and carbon black suspended in Nafion, ethanol, isopropanol, and water. When first adding manganese (x = 0.2), the overpotential slightly increased from 0.59 V (Fe_2P) to 0.62 V. However, there was a significant improvement in the catalytic performance when $x \geq 0.2$, exhibited by a decrease in overpotential for water oxidation from 0.62 V for $Fe_{1.8}Mn_{0.2}P$ to 0.48 V for $Fe_{1.3}Mn_{0.7}P$ at a current density of 10 mA/cm^2 (**Figure 6.3b** and **c**). The origin of the increase in overpotential for x = 0.2 is not clear, but may be a function of the morphological changes that ensue when Mn is introduced (i.e., Fe_2P nanorods are twice as long as $Fe_{2-x}Mn_xP$ nanorods) rather than an electronic effect.

6.3.3 Synthesis and Characterization of $Fe_{2-x}Mn_xP$ Nanorods (x =0.9)

In an effort to increase catalytic efficiency, we attempted to increase Mn loading in the sample. Introducing more manganese precursor after saturation can shift the equilibrium toward incorporation and result in a more Mn-rich phase. Therefore, we introduced a second injection of $Mn_2(CO)_{10}$ into the system after 3 h of reaction. This allowed us to achieve x=0.9, $Fe_{1.1}Mn_{0.9}P$ (from EDS and ICP-MS, **Table 6.1**). TEM images (**Figure 6.7a**) show the $Fe_{1.1}Mn_{0.9}P$ nanorods have the same width but have undergone a decrease in average length to 48.9 ± 7.3 nm, relative to lower values of x (ca 75 nm in length). High-resolution STEM imaging shows the rod is growing along (002) direction (observed lattice fringes have 1.74 Å spacing corresponding to the (002) plane of hexagonal Fe_2P), as expected. The

homogenous nature of the synthesized nanorods was verified by performing an elemental mapping and a line scan (**Figure 6.7c**, **d**). The data show that Mn, Fe and P are homogeneously distributed within the nanorods. XRD data (**Figure 6.5**) shows the formation of the metastable hexagonal phase for $Fe_{1.1}Mn_{0.9}P$, in lieu of the thermodynamic orthorhombic phase that is expected for this composition. As predicted, the increase in x did lead to a further reduction in overpotential by 40 mV, to 0.44 V (**Figure 6.8a**, **b**)

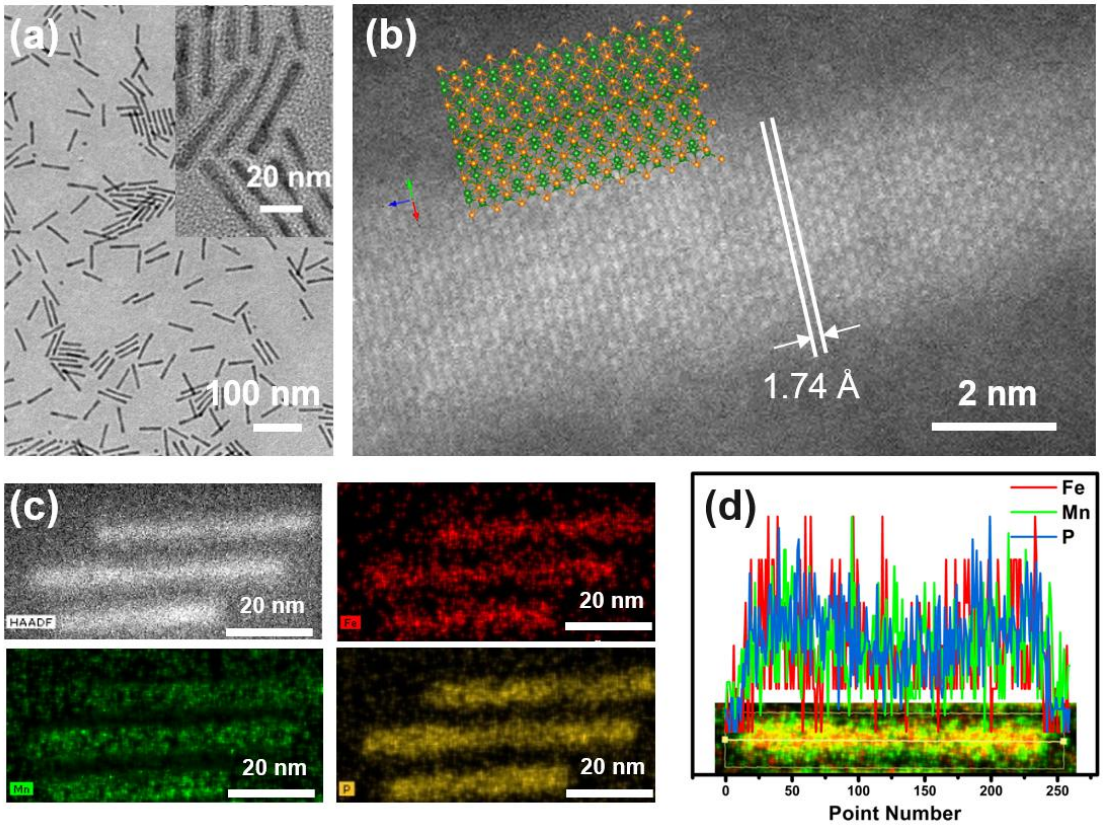

Figure 6.7. (a) TEM image (inset: HRTEM image) of $Fe_{1.1}Mn_{0.9}P$ nanorods; (b) HR-HAADF image of a portion of one $Fe_{1.1}Mn_{0.9}P$ nanorod (inset: structural model of the $Fe_{1.1}Mn_{0.9}P$ nanorods); (c) HAADF image and its corresponding STEM elemental mapping data for $Fe_{1.1}Mn_{0.9}P$ nanorods; (d) line scan for one $Fe_{1.1}Mn_{0.9}P$ nanorod.

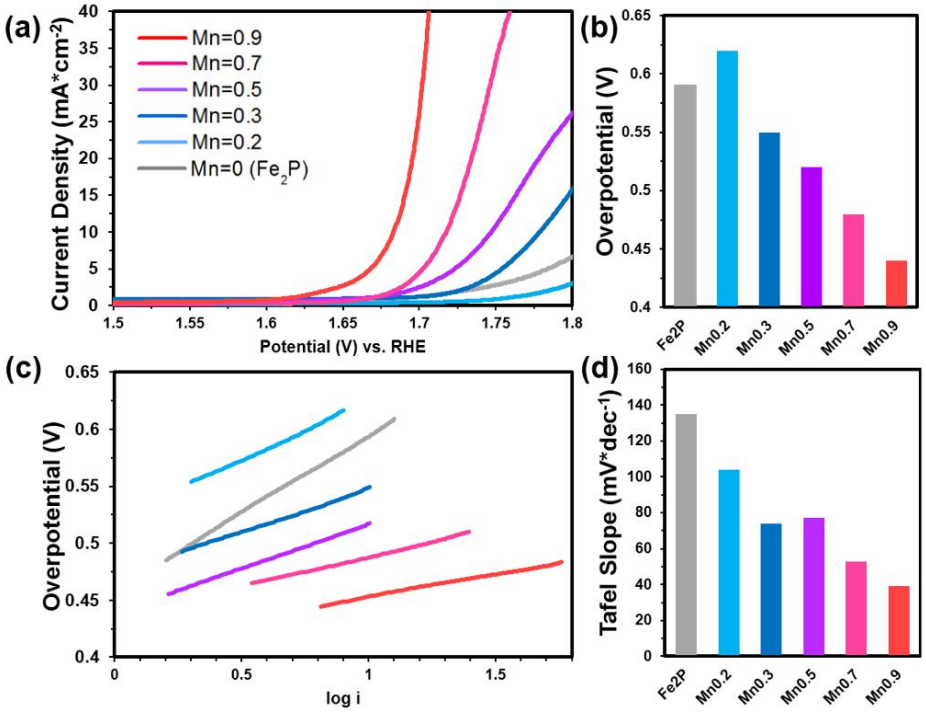

Figure 6.8. Electrocatalytic oxygen evolution properties of $Fe_{2-x}Mn_xP$ nanorods. (a) Polarization curves of the $Fe_{2-x}Mn_xP$ nanorods in 1.0 M KOH; (b) overpotentials required at j = 10 mA/cm^2; (c) the corresponding Tafel plots of the polarization curves of $Fe_{2-x}Mn_xP$; (d) plot of Tafel slopes as a function of x.

6.3.4 Effect of Mn Concentration and Annealing on Electro-catalytic Performance of $Fe_{2-x}Mn_xP$ nanorods

Interestingly, depending on the Mn loading in the sample, we observe different Tafel slopes (**Figure 6.8c**, **d**). For $Fe_{1.75}Mn_{0.25}P$ we observe a Tafel slope equal to 100 mV/dec. However, when the Mn loading was increased to x = 0.3 or 0.5, the Tafel slope decreased to 81 mv/dec; for $Mn_{0.7}$ the Tafel slope decreased to 53 mV/dec; and for x = 0.9 the Tafel slope is 39 mV/dec. These results suggest that changing the manganese loading greatly influences the mechanism by which the OER reaction proceeds. These results are in line with our recent observations, which have shown that the inclusion of manganese into cobalt phosphide materials decreases the overpotential and Tafel slope. This may be attributed to a decrease

in the energy barrier for the proton coupled electron transfer processes and the facilitation of O-O bond formation process due to synergism between Mn and Fe sites.[101, 103]

IR spectroscopy (**Figure 6.9a**) suggests that the nanorod surfaces are ligand-coated, with clear signals indicative of oleylamine, which can block active sites and thus lower the OER activity of $Fe_{2-x}Mn_xP$ nanorods. In an attempt to further reduce the overpotential, we hypothesized that removing the surface bound ligands can facilitate oxygen evolution. Therefore, samples of x = 0.5 and x = 0.9 were annealed in the presence of carbon black under a reducing atmosphere (5% H_2 in Ar), to yield a product with a similar morphology, composition and crystallite size to the unannealed samples (**Figure 6.9b** and **c**). However, the FTIR spectrum shows the disappearance of the peaks associated with oleylamine (**Figure 6.9a**). After annealing, the overpotentials for $Fe_{1.5}Mn_{0.5}P$ and $Fe_{1.1}Mn_{0.9}P$ decreased from 0.52 to 0.43 V and 0.44 to 0.35 V, respectively (**Figure 6.10**), with the latter having comparable performance to CoMnP and other non-noble metal phosphide materials before deactivation (**APPENDIX C, Table C1**).[19-21, 23, 25, 26, 42, 121-124] Moreover，it is lower than a commercially available RuO_2 specimen run under similar experimental conditions (0.37 V, **Figure 6.10**). The Faradaic efficiency of $Fe_{1.1}Mn_{0.9}P$ nanorods was also measured and was found to reach 95% after 2 h of catalysis, suggesting that the catalyst is highly selective towards the oxygen evolution reaction. Therefore, $Fe_{1.1}Mn_{0.9}P$ nanorods can be considered among the more active catalysts reported in the literature for water oxidation.

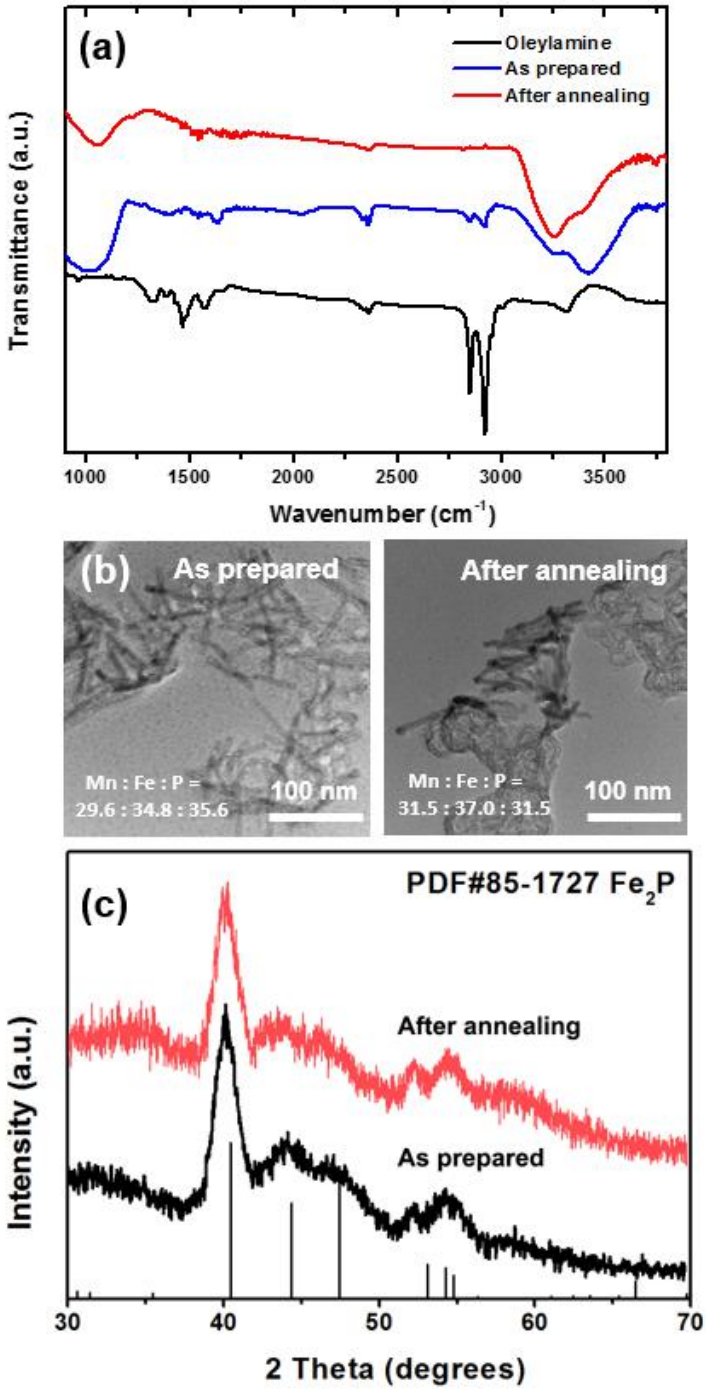

Figure 6.9. (a) FT-IR spectra of oleylamine and $Fe_{1.1}Mn_{0.9}P/C$ nanorods, revealing the existence of both oleylamine ligand and phosphate on the surface of FeMnP nanorods (C-H stretch: 2852 and 2924 cm^{-1}; C-N stretch: 1385 cm^{-1}; N-H stretch: 3250-3450 cm^{-1}; P=O stretch: 1000-1050 cm^{-1}); (b) TEM images (element ratios measured from EDS) and (c) XRD patterns of $Fe_{1.1}Mn_{0.9}P/C$ nanorods before and after annealing. The low-contrast curved features in the annealed sample (b) are ascribed to residual carbon black.

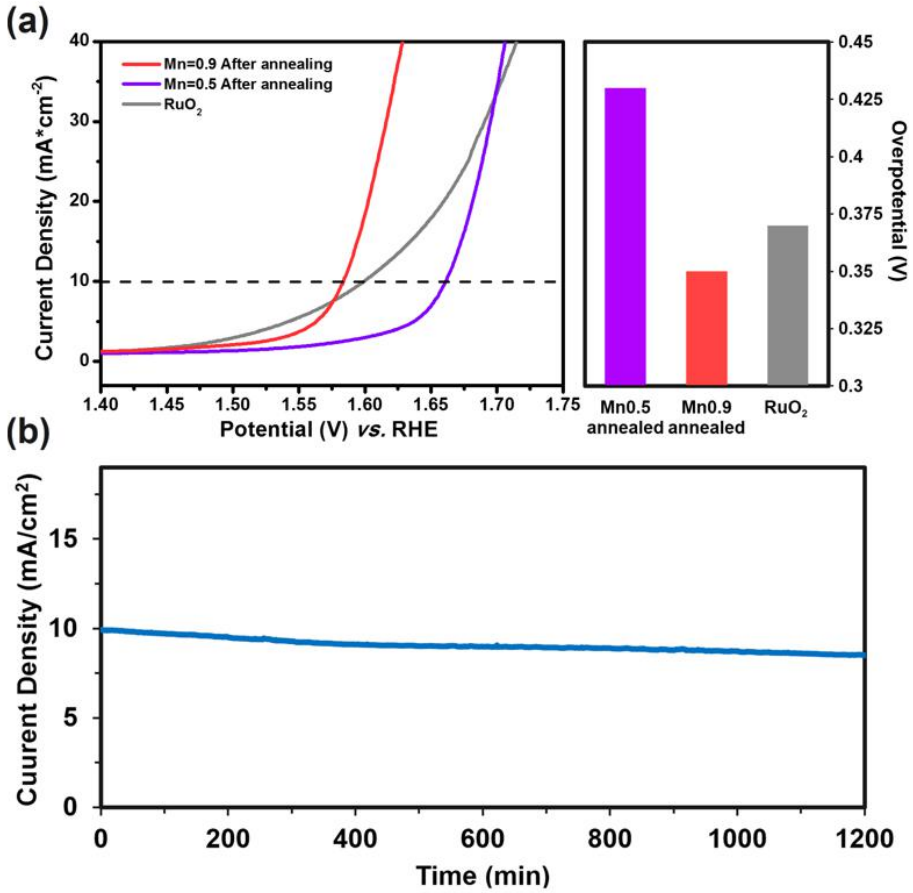

Figure 6.10. Electrocatalytic oxygen evolution properties of $Fe_{2-x}Mn_xP$ nanorods vs. RuO_2. (a) Polarization curves of the $Fe_{1.5}Mn_{0.5}P$, $Fe_{1.1}Mn_{0.9}P$ nanorods after annealing, and RuO_2 in 1.0 M KOH; (b) controlled potential electrolysis on the $Fe_{1.1}Mn_{0.9}P$ nanorods in 1.0 M KOH at 1.58 V (vs. RHE) over 20 hours.

6.3.5 Stability Testing of $Fe_{2-x}Mn_xP$ (x = 0.9) nanorods for Electro-Catalytic Water Splitting

In order to evaluate the stability of the $Fe_{2-x}Mn_xP$ catalysts, controlled potential electrolysis (CPE) was carried out on annealed $Fe_{1.1}Mn_{0.9}P$ samples in 1.0 M KOH, by applying a constant potential of 1.58 V (vs RHE). After 20 hours, the current density was relatively stable and 91% of the initial value was retained (**Figure**

6.10b). This new class of metal phosphides shows enhanced stability compared to CoMnP, where only 80% of the initial current density was retained (**Chapter 5**).

To better understand the nature of the catalyst, X-ray photoelectron spectroscopy (XPS) analyses were performed on the samples before and after a 2 h CPE experiment (**Figure 6.11**). Before catalysis, the high resolution XPS spectrum of Fe exhibited two peaks assigned to reduced Fe in Fe_2P (706.9 eV) and Fe^{2+} (710.4 eV),[125, 126] with the latter ascribed to surface oxidation. The XPS spectra of Mn showed a peak at 641.0 eV, which is corresponding to Mn^{2+}, indicating that the surface Mn atoms were predominately oxidized due to the high oxophicility of Mn.[20, 113] The XPS spectra of P showed two peaks, one assigned to phosphide (resolved doublet: $2p_{2/3}$ at 129.6 eV and $2p_{1/2}$ at 130.4 eV) and phosphate or phosphite (unresolved doublet centered at 133.5 eV).[125] The presence of phosphate in these samples is also evident in FT-IR spectra (**Figure 6.9a**). After 2 h CPE, the intensity of the low energy peaks of Fe (706.9 eV) and P (129.7 eV) had signficantly decreased in intensity and the peaks corresponding to oxidized Mn and Fe species shifted to higher binding energies (Mn: from 641.0 eV to 642.0 eV, Fe: from 710.4 eV to 711.2 eV), indicating that further surface oxidation occurred resulting in the formation of M^{3+} species (M = Fe or Mn) such as M_2O_3, M(O)OH or MPO_4 during catalysis.[127-130] Consistent with this interpretation, post-CPE TEM images of $Fe_{1.1}Mn_{0.9}P$ nanorods (**Figure 6.12a**) reveal an amorphous layer has formed around the crystalline rod, likely composed of metal phosphate and hydroxide/oxo-hydroxide moieties generated in-situ on the surface under OER catalytic conditions as previously noted for other

phosphides.[19-21, 88, 122, 131, 132] These moieties are expected to be highly active species toward water oxidation catalysis.

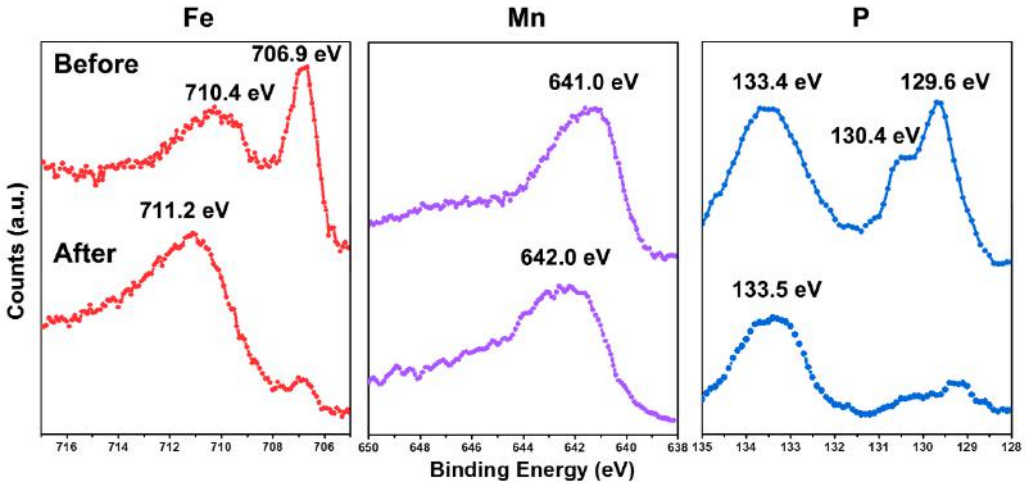

Figure 6.11. High-resolution XPS patterns for $Fe_{1.1}Mn_{0.9}P$ nanorods before (top) and after (bottom) electrolysis for 2 h: Fe (2p3/2), Mn (2p3/2), and P (2p).

EDX studies (**Figure 6.12b**) showed Mn, Fe, and P remain in nanorods after the CPE study, but with a significant decrease in P content when compared to the nanorods before catalysis. Loss of phosphorus was confirmed by the analysis of the electrolyte post-CPE by ICP-MS (**Table 6.3**), suggesting that P is being leached from the catalyst into the electrolyte, likely as phosphate, over time, whereas the metal leaching rate is much lower (by a factor of 10) and roughly equivalent for Fe and Mn. As surface phosphates have been reported to assist in water oxidation catalysis via proton coupled electron transfer,[20, 21, 46, 101, 122] the decrease in activity over time may be ascribed to the surface-bound phosphate loss.

(a)

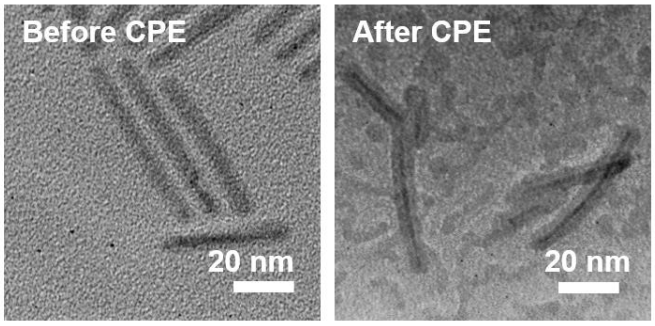

(b)

EDS	Mn	Fe	P
Before CPE	27.4	33.4	39.2
After CPE	38.4	46.0	15.6

Figure 6.12. TEM images of $Fe_{1.1}Mn_{0.9}P$ nanorods before and after CPE.

Table 6.3. ICP-MS data of the electrolyte solution before and after a fifteen-hour controlled potential electrolysis (CPE) experiment, which was carried out in 1.0 M KOH, by applying a constant potential of 1.58 V (vs RHE).

Element	Before (5 h soak) Concentration (ppb)	After CPE Concentration (ppb)	After CPE (Mole change ratio x : Mn)
P K	11.60	208.84	24.27
Mn K	2.08	16.50	1.00
Fe K	22.32	42.51	1.38

6.4 Conclusions

The synthesis of homogenous $Fe_{2-x}Mn_xP$ nanorods with control of Mn incorporation has been demonstrated. Under OER catalytic condition, an oxidative transformation occurred on the surface of these nanorods and the in-situ generated oxidized species are likely responsible for the high activity toward water oxidation catalysis. After an initial increase between x = 0 (Fe_2P) and x = 0.2, the OER overpotential decreases with the incorporation of Mn into the system, up to the highest value of x prepared (x = 0.9). These data suggest the stoichiometry of bimetallic phosphides is a key determiner of activity, either reflecting electronic modulation of the active site or the participation of multiple metal sites to achieve water oxidation and O_2 formation/release. Augmented access to the surface

(perhaps accompanied by surface reconstruction) via annealing to remove surface ligands is shown to further decrease the overpotential by nearly 0.1 V, resulting in overpotentials as low as 0.35 V. Modest decreases in activity occur over time, ascribed to loss of phosphate from the catalyst surface.

CHAPTER 7. VISIBLE LIGHT INDUCED PHOTOCATALYTIC HYDROGEN EVOLUTION USING A NI_2P-CDS HYBRID AEROGEL SYSTEM

Due to the increasing global energy demand and the climate change impact of CO_2 from energy production, it is essential to construct clean energy production and storage systems. Photocatalytic evolution of hydrogen from water utilizing visible light is a promising and appealing pathway. CdS nanoparticles are good visible light absorbers but not efficient hydrogen evolution catalysts, while Ni_2P is shown to be an outstanding electrocatalyst for the hydrogen evolution reaction (HER). Integration of CdS nanoparticles with Ni_2P nanoparticles using a sol-gel approach is expected to yield a hybrid system in which photo generated carriers on CdS are transferred to catalytically active Ni_2P sites. In this work, the assembly of preformed nanoparticles to make Ni_2P-CdS hybrid aerogels will be described and photocatalytic HER data will be presented. The performance of these novel architectures will be compared to CdS nanoparticles and CdS aerogels and the role of interparticle coupling, porosity, and surface passivation on catalytic efficiency will be discussed.

Li, D., Whisnant K. G., Brock, S. L. “Visible Light Induced Photocatalytic Hydrogen Evolution Using a Ni_2P-CdS Hybrid Aerogel System.” *In preparation*

7.1 Introduction

In order to meet growing global energy demand and reduce CO_2 emission from traditional energy resources, it is essential to find an abundant and renewable energy system to supplement (or supplant) current resources. Splitting water utilizing visible light is a promising and appealing pathway because it can provide chemically stored energy from solar energy. As an ultra-clean and renewable energy source, hydrogen (H_2) obtainable from water through the reduction half reaction serves as a feasible source of alternative energy.

Cadmium sulfide (CdS), due to the correspondence of its band gap to visible light, is considered to be one of the promising candidates for visible light driven photocatalytic water splitting. However, CdS alone doesn't exhibit high photocatalytic activity due to its fast electron–hole recombination and photocorrosion. Therefore, CdS is generally paired with a co-catalyst on the surface to improve photoactivity and stability.[133] Nickel phosphide (Ni_2P) nanoparticles are not active photocatalysts, but have emerged as stable electrocatalysts for hydrogen evolution, capable of lowering the activation barrier of the hydrogen evolution reaction due to their ability to bond with hydrogen reversibly.[134-136] Moreover, both CdS and Ni_2P are noble-metal-free materials, which can lower the cost of catalyst preparations and facilitate their practical applications compared to previous systems that utilize noble-metal catalysts for H_2 evolution.[137]

Accordingly, different systems based on CdS and Ni_2P materials have been constructed to achieve efficient performance for the photocatalytic hydrogen

evolution reaction (HER). The Fu group combined Ni_2P particles with CdS nanorods in a lactic acid solution and achieved efficient light-driven hydrogen evolution activity with an initial turnover frequency (TOF) of 2110.[138] Sun and his coworkers reported a method, in which Ni_2P nanoparticles were deposited on CdS rods though solvothermal reactions, achieving a H_2 evolution rate of 553.7 $\mu mol*h^{-1}*mg^{-1}$.[137] However, the light harvesting compound CdS are relatively large (~1 μm rods), limiting catalytically active site availability.

Aerogels composed of semiconductors that absorb visible light are appealing materials for catalytic applications because of their high specific surface areas (100– 300 m^2/g) and interconnected pore structures. The high surface area increases the accessibility of reactive sites, while the continuous meso/macroporous structure enables fast transfer of reactants to, and products from, the reactive sites.[139] Previous photocatalytic studies of organic dye degradation, as well as photocurrent studies proved that by assembling semiconductor nanoparticles into a highly porous network via dichalcogenide bonding facilitates the charge carrier separation, which in turn reduces the electron-hole recombination and enhances catalytic performance.[140, 141] In this work, we established a protocol for assembly of preformed nanoparticles to form Ni_2P-CdS hybrid aerogels for photocatalytic HER. Under optimal conditions, the H_2 evolution rate of the hybrid aerogel can reach as high as 778.2 $\mu mol*h^{-1}*mg^{-1}$ with a TOF of 23090 based on per mole of Ni_2P, indicating the superior photocatalytic activity for HER.

7.2 Experimental

All materials used are given in Chapter 2.

7.2.1 Synthesis of CdS nanoparticles

A mixture of 0.06 g cadmium oxide (CdO), 0.23 g tetradecylphosphonic acid (TDPA), and 3.0 g trioctylphosphonic oxide (TOPO) was first heated to 150 °C under vacuum. The solution was then heated to 320 °C under argon flow until it become colorless. 2.0 mL trioctylphosphine (TOP) was injected and the resultant solution was heated to 370 °C. At 370 °C, a solution of 2.3 mL TOP and 90 µL bis trimethylsilane (TMS) was injected. The yellow precipitate was sonicated in toluene and reprecipitated with ethanol. This sonication-precipitation cycle was done at least two times to remove as much the bound organics as possible from the system.

7.2.2 Synthesis of Ni_2P nanoparticles

A mixture of 0.514 g of nickel (II) acetylacetonate ($Ni(acac)_2$) and 5.0 mL n-octyl ether was heated to 110 °C under argon flow. The solution was then injected into a degassed solution containing 5.0 mL n-octyl ether, 2.0 mL oleylamine, and 12 mL TOP heated at 350 °C. The combined solution was then held at 350 °C for 1 hour. The black precipitate was sonicated in chloroform and reprecipitated with ethanol. This sonication-precipitation cycle was done at least two times to remove as much the bound organics as possible from the system.

7.2.3 Ligand Exchange

1.6 mmol of MUA (0.3678 g) or thioglycolic acid (0.11 mL) was dissolved in 10 mL of methanol. Tetramethylammonium hydroxide (TMAH) was added until the pH of the solution reached 10.

7.2.3.1 Separate Ligand Exchange of CdS and Ni_2P nanoparticles

As-prepared CdS and Ni_2P nanoparticles were dispersed in the ligand exchange solution, precipitated with ethyl acetate, and centrifuged to remove the original organic solvents and ligands. Excess thiolate ligands were removed by washing with ethyl acetate. 2 mL methanol was added to disperse the thiolate capped nanoparticles creating the sols. CdS and Ni_2P sols were then mixed proportionally and sonicated, creating the mixed sol for gelation.

7.2.3.2 Combined Ligand Exchange of CdS and Ni_2P nanoparticles

80 mg Ni_2P nanoparticles were first dispersed in 5 mL methanol to prepare a stock solution. A fraction of the Ni_2P stock solution (volume depends on the target composition) was then added to CdS nanoparticles. The mixed solution was sonicated for 10 min and then added into the ligand exchange solution. The resultant solution was sonicated for 20 min, then precipitated with ethyl acetate, and centrifuged to remove the original organic solvents and ligands. Excess thiolate ligands were removed by washing with ethyl acetate. 2 mL methanol was added to disperse the thiolate capped nanoparticles, creating the sol for gelation.

7.2.4 Gel Formation & Aerogel Preparation

Wet gels of Ni_2P-CdS were formed thorough the oxidative induced gelation method[142] by adding 30 µL 3.0% tetranitromethane (TNM) solution containing 30 µL TNM and 1.0 mL acetone into the sol. Following the addition of 3.0% TNM, the solutions were left to age for 1 week under ambient conditions to form opaque uniform wet gels. Wet gel solvent was exchanged 6-8 times with acetone over 3-4 days to remove the byproducts from oxidation. The resulting gels were washed with acetone and dried through a critical point process as described previously.[142]

7.2.5 Photocatalytic Hydrogen Evolution

The photocatalytic hydrogen evolution experiments were carried out in a 20 mL vial with stirring at ambient temperature using a 300 W xenon lamp equipped with a UV cut-off filter. Monolithic aerogels were crushed to from a powder. 0.2 mg of the photocatalyst was dispersed in 10 mL of aqueous solution containing Na_2S and Na_2SO_3 as sacrificial reagents, and then the suspension was stirred and purged with nitrogen for 20 min to remove air. Hydrogen gas was measured by gas chromatography using a thermal conductivity detector (TCD). The hydrogen evolution rate was calculated based on the mass of photocatalysts. The turnover frequency (TOF) was calculated by using the following equations:

$$\text{TON} = \text{moles of } H_2/\text{moles of } Ni_2P \text{ on photocatalyst}$$

$$\text{TOF} = \text{TON/reaction time (hours)}$$

7.2.6 Characterization

Transmission electron microscopy (TEM), energy dispersive spectroscopy (EDS) and powder X-ray diffraction (PXRD) were perfomed as describe in **Chapter 2**.

7.2.6.1 Surface Area Analysis

The surface area of samples was determined by obtaining nitrogen physisorption isotherms on samples at 77 K by using a Micromeritics TriStar II 3020 surface area analyzer. All samples were degassed for 24 h at 423 K under N_2 flow before the analysis. The Brunauer-Emmett-Teller (BET) multimolecular adsorption method was used to calculate surface areas and Barrett-Joyner-Halenda (BJH) method was used to measure pore size distributions.

7.2.6.2 UV-vis Diffuse Reflectance Spectroscopy

A JASCO V-570 UV/VIS/NIR Spectrometer with integrating sphere was used to measure the UV-vis diffuse reflectance spectra. The solid samples were mixed with barium sulfate to form homogeneous solids. The mixture was then placed in the sample holder.

7.3 Results and Discussion

7.3.1 Preparation of Ni_2P-CdS hybrid aerogels

Nearly monodisperse Ni_2P and CdS nanoparticles were synthesized through solution-phase arrested-precipitation reactions by reacting $Ni(acac)_2$ with tri-octylphosphine (TOP) and CdO with Bis(trimethylsilyl)sulfide (TMS), respectively. Power X-ray diffraction patterns (**Figure 7.1a** and **c**) show that Ni_2P and CdS both exhibit hexagonal structures, characteristic of their respective structure. No additional reflections were observed, suggesting an absence of significant (> 5%) crystalline impurities. Transmission electron microscopy (TEM) images (**Figure 7.1b** and **d**) indicate CdS and Ni_2P nanoparticles are both spherical with an average size of 4.8 nm and 6.1 nm, respectively.

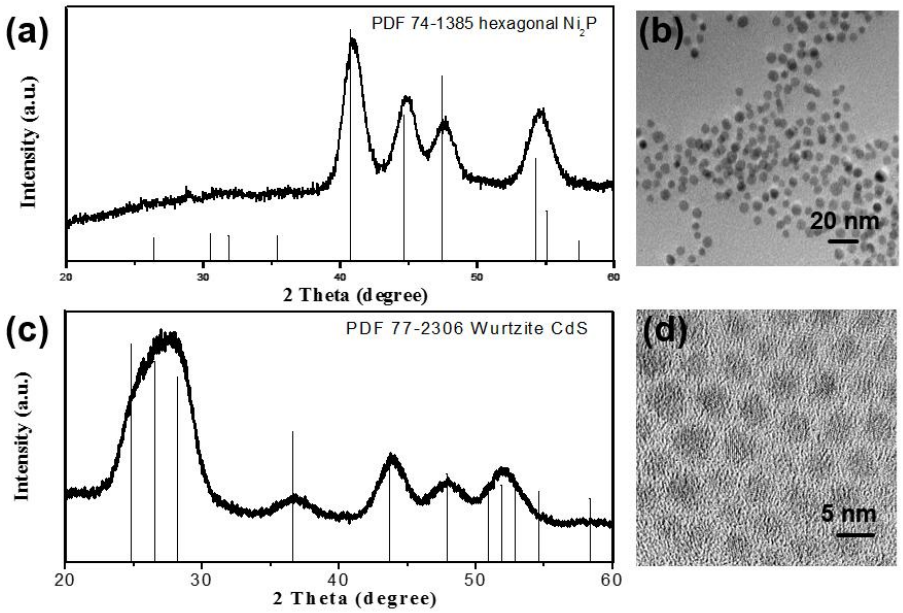

Figure 7.1 (a) PXRD pattern and (b) TEM image of Ni_2P nanoparticles. (c) PXRD pattern and (d) TEM image of CdS nanoparticles.

Following synthesis, CdS and Ni_2P nanoparticles were isolated and capped with thioglycolic acid (details in section 7.2.3) separately. The resultant thiolate-capped nanoparticles were dispersed in methanol and then mixed different proportions to generate a hybrid sol for gelation. Tetranitromethane (TNM), an oxidizing agent, was used to achieve controlled surface oxidation that could lead to gelation. **Scheme 7.1** describes the gelation process where thiolate ligands are oxidatively removed from the particles' surface by TNM yielding as disulfides, RS-SR. Subsequently, TNM further oxidizes the exposed surface sulfide, leading to formation of inter-particle disulfide ($S\text{-}S^{2-}$) bonding and assembly of nanoparticles. The formed wet gel was aged and solvent-exchanged with acetone to remove the byproducts from oxidation. Ni_2P-CdS wet gels were then dried using a CO_2 supercritical dryer, enabling a process that avoided pore collapse and maintained the integrity of the gel. The resulting Ni_2P-CdS aerogels (**Figure 7.2a**), showed a

minimum volume loss (5-10%) when compared to the wet gels prior to supercritical drying.

Scheme 7.1 Scheme showing the main steps involved in formation of CdS aerogels from thiolate capped-CdS NCs

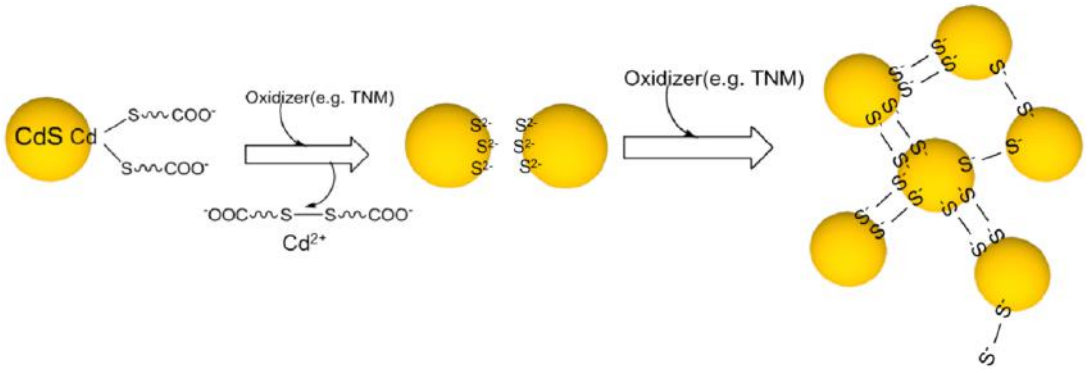

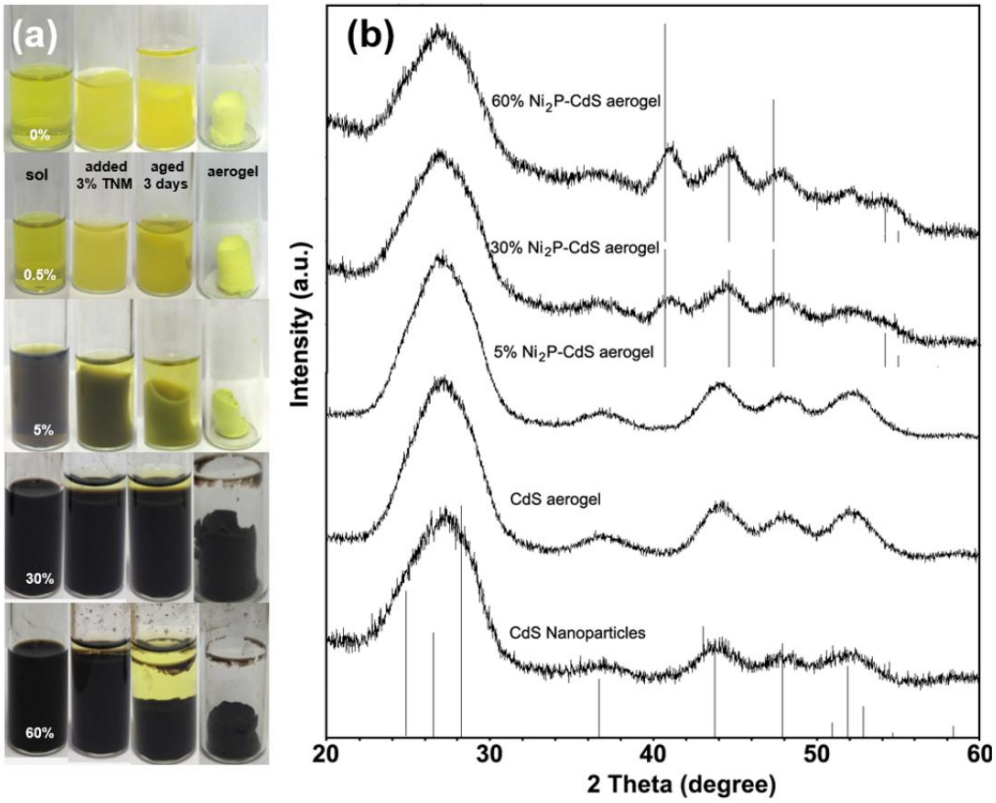

Figure 7.2 (a) Photographs of sols, gels, and aerogels with different loadings of Ni_2P throughout the formation process and (b) PXRD patterns of CdS nanoparticles and aerogels with different loadings of Ni_2P. Reference spectra for CdS and Ni2P are shown as stick diagrams at the bottom and top, respectively.

Figure 7.2b shows the PXRD patterns for hybrid aerogels with different compositions. When the Ni_2P loading is smaller than 20%, no obvious diffraction peak corresponding to the Ni_2P phase is observed due to the small amount of Ni_2P and the strong diffraction peaks from CdS. For a Ni_2P loading of more than 30%, peaks that correspond to Ni_2P and CdS are observed. These peaks are nearly identical to ones observed before gelation (**Figure 7.1**), indicating neither the size nor the structure of the two components has changed significantly.

Scheme 2 shows the two possible processes that may occur during co-gelation. In the top pathway, a phase separation between two components occurs, while in the bottom pathway, the two components are well-mixed to form a well-dispersed system. For photocatalytic HER, a good dispersion of co-catalyst on light absorbers (**Scheme 2**, bottom pathway) is desired because it provides a rapid charge injection from photo-absorbs to co-catalyst.

Scheme 7.2 Illustration of possible pathways of co-gelation of two nanoparticle components

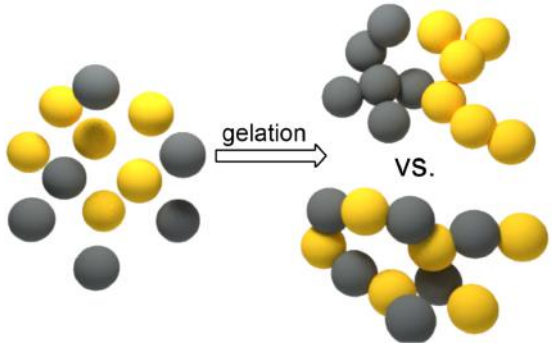

As shown in **Figure 7.2a**, with the increasing loading of Ni_2P nanoparticles, the color of the final aerogels changed from bright yellow (0%) to yellow (0.5%), to black-yellow (5%), and to black (30%, 60%). The color is consistent through the entire aerogel (top, bottom, inside core, and outside layer), indicating a likely good

dispersion of Ni_2P nanoparticles. However, the TEM images of the hybrid aerogels (**Figure 7.3b**, 5% Ni_2P-CdS was chosen as a representative composition) showed that Ni_2P nanoparticles are more likely embedded inside the aerogel network as aggregations, which may cause poor interactions between Ni_2P (co-catalyst) and CdS (light absorber) nanoparticles and limit the number of accessible active sites. Moreover, aerogels with these Ni_2P clusters have poor thermal stability. The Ni_2P nanoparticles sintered (**Figure 7.3c**) when applying a thermal treatment (Ar@250 °C, 1 hour) for extra organic surfactant removal, which would further decrease the activity of a catalyst.[143] As mentioned above, ligand exchange was operated separately for Ni_2P and CdS nanoparticles with thioglycolic acid. Thioglycolic acid was selected because of its short length which provides efficient removal of surface ligands and easy accessibility to the particle surface, resulting in a better catalytic performance.[140] However, a dilemma presented as this short chain thiol may lead to Ni_2P nanoparticles' insufficient surface stabilization and cause aggregation of Ni_2P before gelation and incorporation into the CdS porous matrix (**Figure 7.3a**). The issue can be resolved by simultaneously conducting ligand exchange for Ni_2P and CdS nanoparticles (**section 7.2.3.2**). As shown in **Figure 7.3d**, the existence of CdS nanoparticles during ligand exchange can prevent Ni_2P nanoparticles from aggregation. Ni_2P nanoparticles (slightly bigger and darker particles) dispersed uniformly in the hybrid aerogel before and after the thermal treatment (**Figure 7.3e** and **f**). This is consistent with what was observed from the PXRD data (**Figure 7.4**) that no obvious change in peak breadths was observed before and after annealing, suggesting a good thermal stability. The final

Ni_2P loadings in different hybrid aerogels were evaluated by energy dispersive spectroscopy (EDS) (**Table 7.1**). The close values of the target and actual Ni_2P loadings indicate a good control over compositions can be achieved using this protocol. Accordingly, hybrid aerogels with different Ni_2P loadings were prepared from nanoparticles ligand-exchanged together, following by annealed to remove extra surface ligands, and testing to evaluate the catalytic activities of visible light-induced HER.

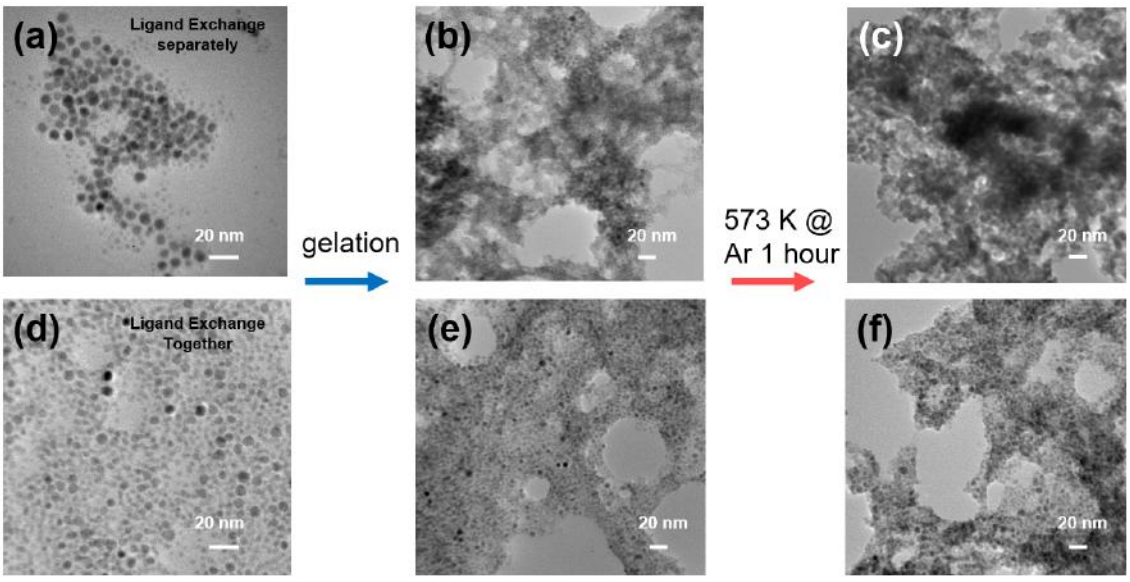

Figure 7.3 TEM images of sols of CdS and Ni_2P nanoparticles ligand-exchanged separately (a) and together (d), their corresponding aerogel before (b), (e) and after annealing (c), (f), respectively.

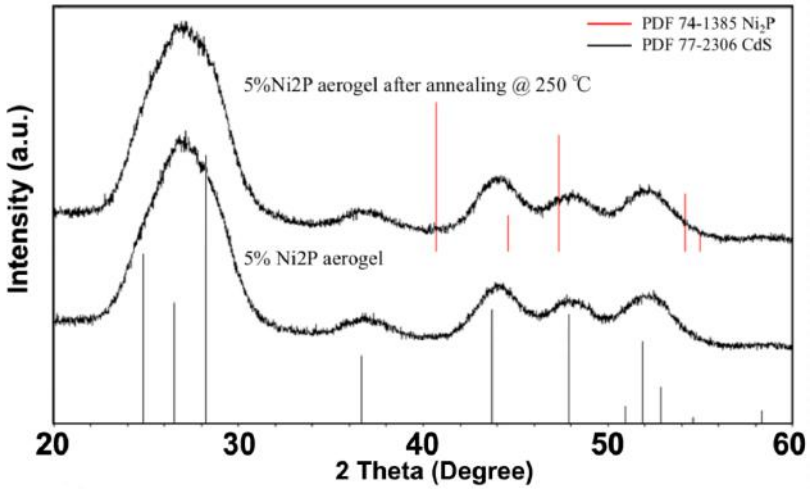

Figure 7.4 PXRD patterns of a 5.0% Ni_2P-CdS aerogel before and after annealing

Table 7.1 Targeted and actual compositions (from EDS) of Ni_2P-CdS hybrid aerogels

Target Ni_2P loading (wt. %)	Actual Ni_2P loading from EDS (wt. %)
0.5	0.5
1	1.1
5	4.9
30	33.3
60	57.8

7.3.2 Visible light-induced HER

The light-induced HER activity of the hybrid aerogels was evaluated under visible light irradiation (λ > 420 nm) using Na_2S/Na_2SO_3 as the hole scavenger. **Figure 7.5a** shows the optical images taken during the generation of hydrogen bubbles from the photocatalysis of 0.5% Ni_2P-CdS aerogel. Once the hydrogen bubbles started being generated, they can carry the aerogels flowing around in the solution. The photocatalytic activity occurring within the system is modeled in **Figure 7.5b**. Following the absorption of photons from light, the CdS nanoparticles generate electron-hole pairs. The photo-generated electrons are transported to the

catalytically active Ni_2P sites, where available water molecules are reduced to hydrogen bubbles, while the photo-generated holes react with the hole scavengers. **Figure 7.5c** shows the hydrogen evolution rates of CdS nanoparticles and CdS aerogels with different loadings of Ni_2P. The pure CdS nanoparticles afforded the lowest rate (21.2 $\mu mol*h^{-1}*mg^{-1}$) while the pure CdS aerogels doubled the activity (43.6 $\mu mol*h^{-1}*mg^{-1}$). When 0.1% Ni_2P was loaded into the CdS aerogel, the activity was dramatically improved to a value of 271.0 $\mu mol*h^{-1}*mg^{-1}$. The CdS aerogel with a Ni_2P loading of 0.5% showed the best rate of hydrogen evolution (778.2 $\mu mol*h^{-1}*mg^{-1}$) with a TOF of 23090 per mole of Ni_2P, which places the 0.5% Ni_2P-CdS hybrid aerogel among the top tier of visible light-induced HER catalysts. Further increasing the Ni_2P loading resulted in a decrease in the hydrogen evolution rate, likely due to the excess light absorption of Ni_2P. The stability of the 0.5% Ni_2P-CdS aerogel is shown in **Figure 7.5d**. The system was evacuated every hour and the process was repeated for 5 times. The hydrogen evolution rate of the 0.5% Ni_2P-CdS aerogel remained within 770-810 $\mu mol*hr^{-1}*mg^{-1}$, indicating a good stability for visible light-induced HER.

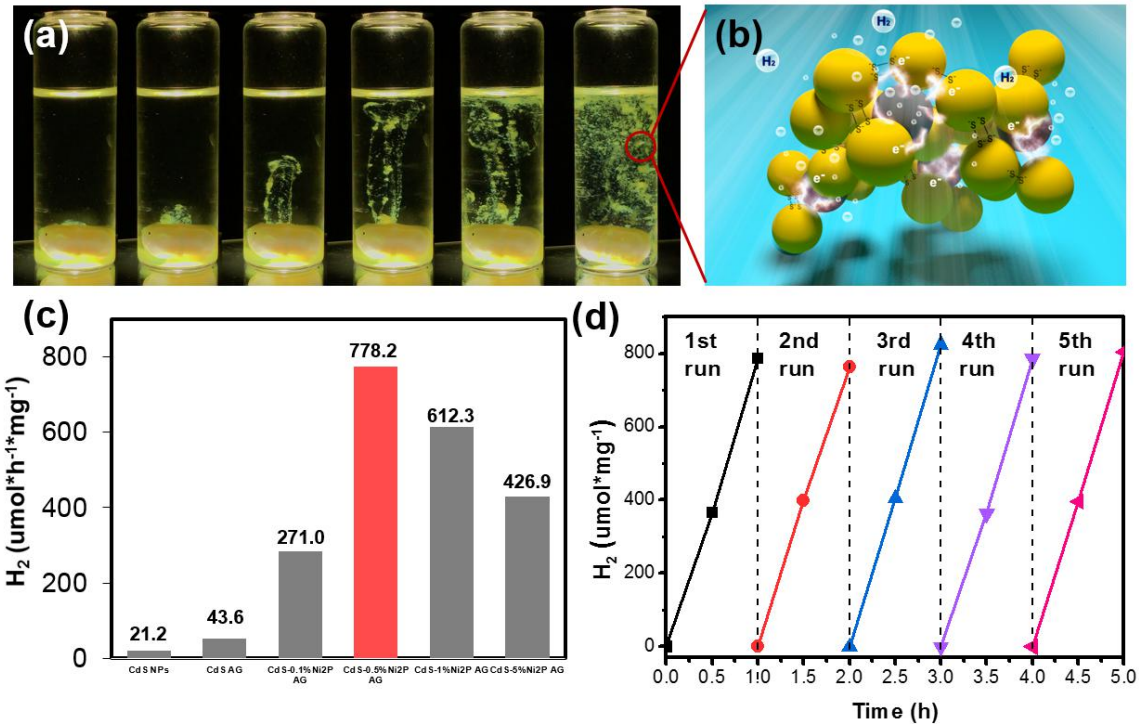

Figure 7.5 (a) Images taken during the generation of hydrogen bubbles from the photocatalysis. (b) Representation of the photocatalytic activity occurring within the system. (c) The H_2 evolution rate of the hybrid aerogels loaded with different amounts of Ni_2P at room temperature under visible light irradiation. (d) Cycling runs for photocatalytic hydrogen evolution using 0.5% Ni_2P-CdS aerogels. The system contains 0.2 mg of catalyst immersed in a 20-mL aqueous solution containing 0.75 M Na_2S and 1.05 M Na_2SO_3.

In order to study the rational factors that lead to the superior photocatalytic HER performance of the hybrid aerogel, a serious of studies were carried out.

7.3.3 Morphology of Ni_2P-CdS hybrid aerogels

TEM images (**Figure 7.6**) reveal the morphology of the 0.5% Ni_2P-CdS hybrid aerogels which exhibit a 3-D porous network in which Ni_2P nanoparticles are dispersed uniformly. High-resolution TEM shows both Ni_2P and CdS maintain the small spherical shape of the initial nanoparticles. The distance between ordered lattice planes of 0.286 nm in a bigger particle can be assigned to the (101) plane of hexagonal Ni_2P, while 0.190 nm in a smaller particle corresponds the (201)

plane of hexagonal CdS. The fast Fourier transform (FFT) of the HRTEM images show ordered diffraction spots (inset of **Figure 7.6c**), which confirms that both Ni_2P and CdS nanoparticles are single crystalline with high quality. The intimate mixing of the two components, combine with the small size and high crystallinity of CdS and Ni_2P nanoparticles are important for visible light-induced HER because they greatly shorten the distance that photogenerated electrons and holes have to travel to reaction sites and thus reduce the likelihood of electron-hole recombination.

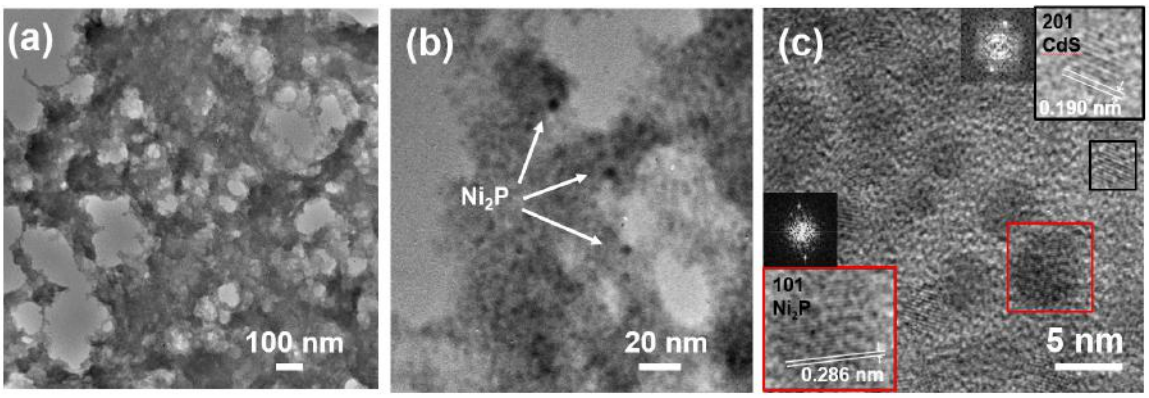

Figure 7.6 (a), (b) TEM images and (c) HRTEM image of a 0.5% Ni_2P-CdS aerogel (inset: FFT of the selected areas).

7.3.4 Surface area measurements of Ni_2P-CdS hybrid aerogels

The 3-D porous structure was confirmed by surface area measurements (**Figure 7.7**). The surface areas of CdS nanoparticles and aerogels were determined by appying of the Brunauer-Emmett-Teller (BET) model. The pore-size distribution and average pore diameter were determined using the Barrett-Joyner-Halenda (BJH) model. CdS nanoparticles exhibit a mesoporous structure (2-50 nm pore diameter) that has a surface area of 27.73 m^2/g, while the CdS and Ni_2P-CdS aerogels both exhibit a combination of mesoporous and macroporous structure (2-200 nm pore diameter) with a surface area of 174.19 and 173.98 m^2/g, respectively. The surface area of nanoparticles is much lower than the theoretical value 248.00 m^2/g, presumably due to the aggregation and overlap of particles. However, by assembling nanoparticles into aerogels, the accessible surface area increased by more than 6 times, which is much closer to the theoretical value. The adsorption-desorption isotherms of the CdS and Ni_2P-CdS aerogel are almost identical, indicating that the hybrid aerogel successfully retained the porous structure from its native. More importantly, the wider size distribution of the aerogels (2-200 nm)

compared to that of the nanoparticles (2-50 nm) enables efficient transport of both reactants to and products from active sites in the system.[139] Additionally, materials with high surface areas can absorb and internally scatter light effectively, improving photon harvesting. The large surface area can also facilitate the adsorption of sacrificial reagents/hole scavengers and thus increase the consumption rate of photo-generated holes, surpassing electron-hole recombination, which ultimately enhances catalytic efficiency.

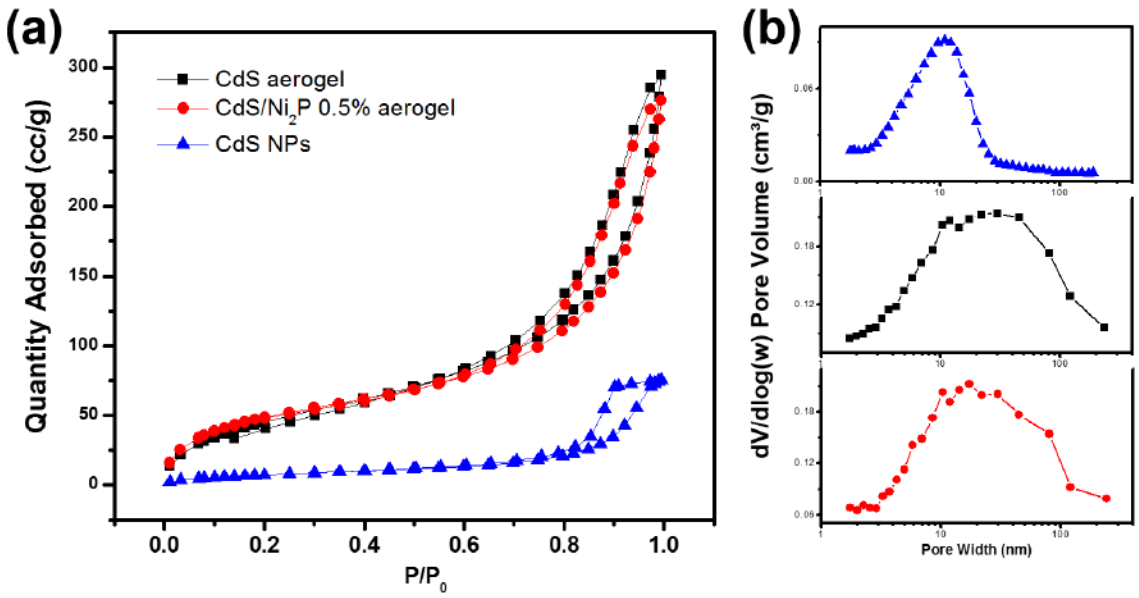

Figure 7.7 (a) N_2 physisorption isotherms of a CdS aerogel, 0.5% Ni_2P-CdS aerogel, and CdS nanoparticles. (b) Pore size distribution of (top to bottom) CdS nanoparticles, CdS aerogel, and 0.5% Ni_2P-CdS aerogel.

7.3.5 Optical properties of Ni_2P-CdS hybrid aerogels

UV-vis diffuse reflectance spectroscopy (UV-vis DRS) was used to access the optical properties of both the CdS aerogel and 0.5% Ni_2P-CdS hybrid aerogel as shown in **Figure 7.8a**. The absorption edge of the CdS aerogel was not shifted after incorporating of Ni_2P, revealing that the incorporation of Ni_2P does not impact the visible-light-suited band gap of the CdS.

The photoluminescence spectra with an excitation wavelength of 405 nm provided in **Figure 7.8b** shows that the CdS aerogel has two emission bands at 460 and 560 nm, corresponding to the band-edge emission and surface trap states.[142] Following Ni_2P loading, the emission peaks of the CdS aerogel were quenched, likely due to the fast rate at which electrons are transferred from CdS to Ni_2P, suppressing the electron-hole recombination and enhancing the photocatalytic activity.

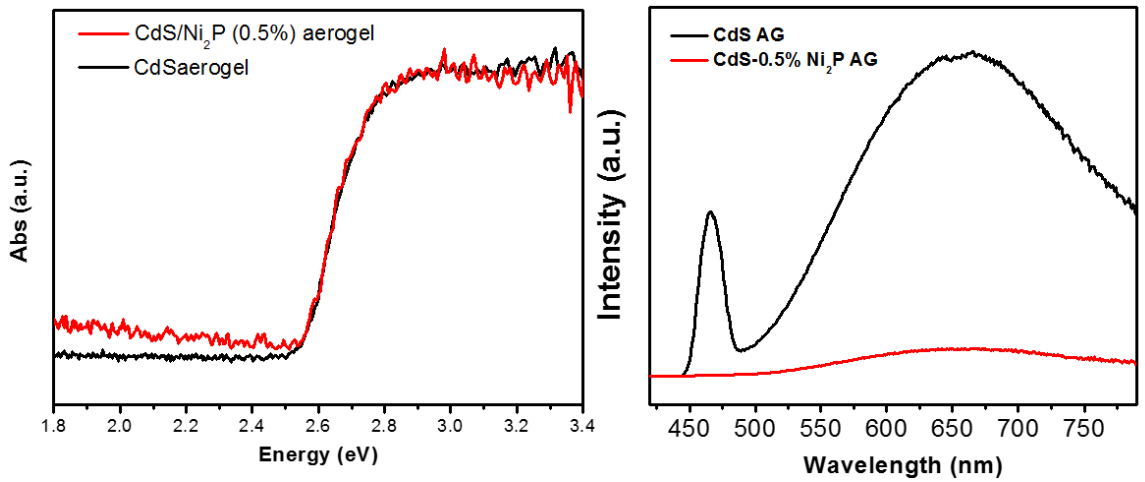

Figure 7.8 (a) UV-vis diffuse reflectance spectra of 0.5% Ni_2P-CdS aerogel and CdS aerogel. (b) Photoluminescence spectra of CdS aerogel and 0.5% Ni_2P-CdS aerogel.

7.3.6 Bonding Possibilities

It is well established that CdS aerogels are formed *via* disulfide ($S–S^{2-}$) bonding, while the bonding between the CdS and Ni_2P nanoparticles remains unclear. CdS and Ni_2P particles could be connected by S-P bonds that are produced by oxidizing surface S and P species with TNM (**Figure 7.9a**, top), or crosslinked by carboxylate terminal groups on the thiol ligand with metal cations (**Figure 7.9a**, bottom). One major difference between these two possibilities is that the latter requires a carboxylate group present in the capping ligands, while the former does

not. In order to differentiate between these two scenarios, 4-fluorothiophenol was used to replace thioglycolic acid as the capping ligand. Sols of 4-fluorothiophenolate capped CdS nanoparticles, and both 4-fluorothiophenolate capped CdS and Ni_2P nanoparticles were prepared (**Figure 7.9b** top). After adding a solution of 3% TNM, the CdS wet gel was still formed (**Figure 7.9b** bottom left), while the hybrid Ni_2P-CdS wet gel was no longer formed (**Figure 7.9b** bottom right). A phase separation occurred instead, in which yellow CdS nanoparticles remained dispersed in the solution while black Ni_2P nanoparticles precipitated at the bottom (**Figure 7.9b** bottom right), indicating that the metal ion cross-linking is responsible for the bonding between CdS and Ni_2P. Indeed, the gel formation due to metal ion cross-linking was observed in Ni_2P aerogels,[144] in which the TNM etched Ni^{2+} ions from the surface. These Ni^{2+} ions subsequently linked together carboxylates (thiolates) in adjoining particles. Accordingly, we hypothesize that in a Ni_2P-CdS hybrid aerogel, CdS nanoparticles are connected *via* disulfide ($S–S^{2-}$) bonding, while CdS and Ni_2P nanoparticles are connected by crosslinking the terminal carboxylate group with metal cations at surface. This enables the interactions between one Ni_2P nanoparticle with multiple CdS nanoparticles at the same time (**Figure 7.5b**), providing quick and powerful electron injections. However, this needs to be verified by further surface analysis study such as XPS.

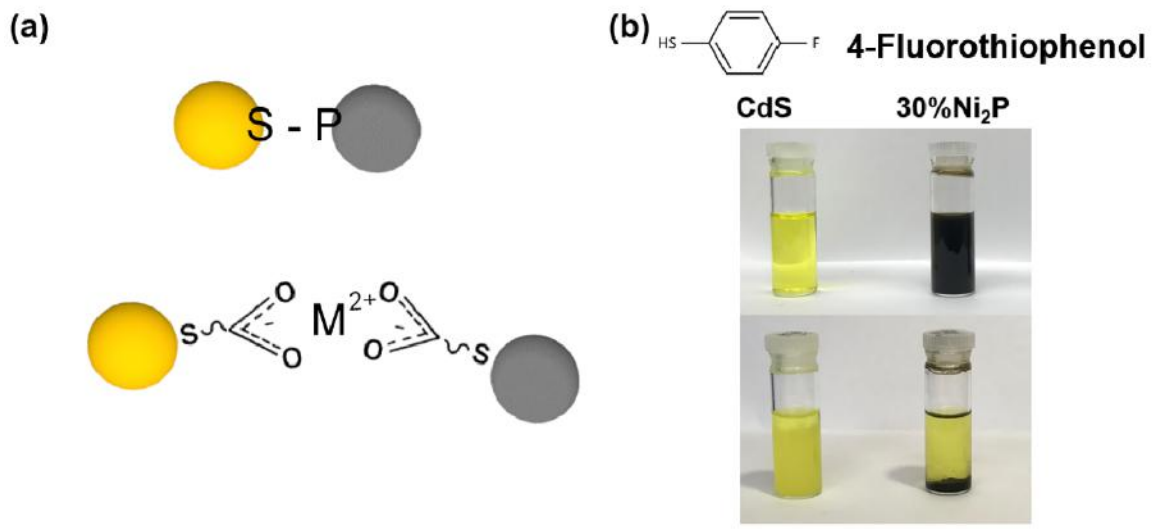

Figure 7.9 (a) Illustration of two bonding possibilities (b) optical images for sols of 4-fluorothiophenol capped CdS nanoparticles (left), 30% Ni_2P and CdS nanoparticles (right) before (top) and after (bottom) adding 3% TNM solution.

7.4 Conclusions

Ni_2P-CdS aerogels with different compositions were successfully prepared from discrete CdS and Ni_2P nanoparticles using oxidative gelation processes followed by supercritical drying. The nanoparticle components remained crystalline and the aerogel exhibited a meso/macroporous structure with a high specific surface area. Hybrid aerogels were shown to have enhanced performances towards photocatalytic hydrogen evolution. with the 0.5% Ni_2P-CdS aerogel showing a H_2 evolution rate of 778.2 $mol \cdot h^{-1} mg^{-1}$ under visible light irradiation. This superior photocatalytic performance, compared to a CdS aerogel (43.6 $\mu mol * h^{-1} * mg^{-1}$) or CdS nanoparticles (3 $\mu mol * h^{-1} * mg^{-1}$), is attributed to (1) the small size of CdS and Ni_2P nanoparticles, and their intimate mixing, which can greatly shorten the distance that photogenerated electrons and holes have to travel to surface reaction sites and thus reduce the likelihood of electron-hole recombination; (2)

the meso/macroporous structure, which allows for efficient absorption and internal scattering of light (enhanced light harvesting) and enables rapid flux of reactants to, and products from, those sites; and (3) the fast charge separation at the CdS/Ni_2P interface, which again reduces the possibility of electron-hole recombination and improves the catalytic activity.

CHAPTER 8. CONCLUSIONS AND PROSPECTUS

8.1 Conclusions

Due to the increasing global energy demand and the climate change impact of CO_2 from energy production, great efforts have been made to develop new systems that produce clean energy or utilize energy more efficiently. Producing hydrogen from water utilizing visible light or electricity is a promising and appealing pathway because water is a clean and renewable energy source. While Magnetic refrigeration is a cooling technology based on the magnetocaloric effect that it consumes 30% less energy than traditional gas-compression refrigeration and requires no refrigerant. Potential candidate materials for these applications have drawn increasing attention.

Transition metal phosphides exhibit a wide range of unique magnetic, redox and catalytic properties. For example, the magnetic properties can be altered from paramagnetic Co_2P to ferromagnetic $Co_xFe_{2-x}P$ with a tunable Curie point close to or above room temperature,[54] which makes this material potentially suitable for magnetic imaging, therapies, refrigeration, or data storage.[55-57] On the other hand, transition metal phosphide nanoparticles are also emerging as a new class of water splitting electro-catalysts with reported high activity in binary metal phosphides such as Ni_2P, Co_2P, and CoP. The OER and HER catalytic activities of metal phosphide materials can also be further improved by introduction of a second metal into binary metal phosphide systems. Recently, the ternary metal phosphides CoFeP, NiCoP, and NiFeP have shown improved OER activity over the binary phases (Co_2P, Fe_2P or Ni_2P), attributed to synergism between the two

metals. However, despite their promise, comparatively little research has been done on ternary (relative to binary) nanoparticles of metal phosphides.

8.1.1 Establishing Synthetic Methods of Transition Metal Phosphides

In this dissertation research, we first systemically studied the effects of synthetic levers on nickel phosphide nanoparticle formation. A phase-control strategy enabling the arrested-precipitation synthesis of nanoparticles of Ni_5P_4 and NiP_2 as phase-pure samples using different Ni organometallic precursors and trioctylphosphine (TOP) was described. The composition and purity of the product can be tuned by changing reaction parameters, including the Ni precursor, the oleylamine (OAm) and TOP concentrations, temperature, time and the presence or absence of a moderate temperature soak step to facilitate formation of Ni and/or Ni-P amorphous nanoparticle intermediates. Notably, the 230 °C intermediate step favors the ultimate formation of Ni_2P and hinders further phosphidation to form Ni_5P_4 or NiP_2 as phase-pure products. In the absence of this step, increasing the P/Ni ratio (13-20), reaction temperature (350-385 °C) and time (10-48 h) favors more P-rich phases, and these parameters can be adjusted to generate either Ni_5P_4 or NiP_2. This part successfully addressed a knowledge gap in the phase evolution for the P rich side of the Ni-P nanoparticle system and elucidate different key synthetic levers.

Then we applied these synthetic levers to the synthesis of different ternary metal phosphide nanomaterials with control of phase and composition. The entire solid solution of $Co_xFe_{2-x}P$ nanoparticles can by prepared by using $Fe(CO)_5$, $Co_2(CO)_8$, and TOP in an arrested precipitation reaction. The method employs

CoFe alloy particles as precursors that are phosphided with TOP, and the resultant nanoparticles are hollow due to diffusion differences between the metal and phosphorus (Kirkendall effect). At intermediate x, the mechanism involves the fusion of small alloy particles into a larger particle, which then acts as a template for the further phosphidation, giving rise to particles with scalloped edges. The target composition is controlled by the initial metal precursor ratio and the size of $Co_xFe_{2-x}P$ can be tuned by varying OAm/metal ratio (16.5 to 20 nm with standard deviations ≤14%). The Curie temperature of $Co_xFe_{2-x}P$ nanoparticles shows a clear composition dependence that is reflective of the behavior of the bulk: it first increases and then decreases with the increase of Fe substitution. The high T_C attained in CoFeP and $Co_{0.7}Fe_{1.3}P$ render these nanoparticles superparamagnetic at room temperature, enabling consideration of transition metal phosphides for applications including magnetic, imaging, and hyperthermia therapies.

Similarly, new phases $Co_{2-x}Mn_xP$ ($0 \leq x \leq 1.2$) can be prepared by injecting $Co_2(CO)_8$ and $Mn_2(CO)_{10}$ into a solution of hot 1-octadecene and oleylamine, followed by injection of TOP and elevation of the solution temperature to 350 °C. While no synthetic method of nanoparticles of "M_2P" phase manganese phosphides has been reported due to the highly oxophilic nature of manganese, we hypothesize that incorporating Co into the system can stabilize Mn in a low-valent state and thus favors the formation of the "M_2P" phase. The CoMnP nanoparticles (ca. 5 nm in diameter) are nearly monodisperse and homogenous in nature. The composition can also be controlled by varying the initial metal precursor ratio.

We also demonstrated the synthesis of $Fe_{2-x}Mn_xP$ ($0 \leq x \leq 0.9$) nanorods with control of Mn incorporation from the solution-phase by reacting manganese and iron carbonyl complexes with TOP. The resultant nanorods are homogeneous in nature and have average lengths of 74.7 ± 10.0 nm ($0 \leq x \leq 0.7$) and 48.9 ± 7.3 nm ($x = 0.9$). However, in this case, the final composition cannot be controlled precisely by changing the starting metal precursor ratio due to the formation of MnO with adventitious oxygen as a competing factor. An alternative method using long reaction times and multiple injections of Mn-precursors was developed enabling a Mn uptake to 0.9.

8.1.2 Catalytic Behavior of new TMP nanoparticles

The new manganese-based phosphide materials are active and efficient water oxidation catalysts. $Co_{2-x}Mn_xP$ exhibit compositional dependent OER properties, in which the lowest overpotential (0.33 V) with a Faradaic efficiency of 96% can be achieved at $x = 1$. For $Fe_{2-x}Mn_xP$ nanorods, after an initial increase between $x = 0$ (Fe_2P) and $x = 0.2$, the OER overpotential decreases with the incorporation of Mn into the system, up to the highest value of x prepared ($x = 0.9$). These data suggest the stoichiometry of bimetallic phosphides is a key determiner of activity, either reflecting electronic modulation of the active site or the participation of multiple metal sites to achieve water oxidation and O_2 formation/release. Moreover, augmented access to the surface (perhaps accompanied by surface reconstruction) via annealing to remove surface ligands is shown to further decrease the overpotential in $Fe_{2-x}Mn_xP$ by nearly 0.1 V, resulting in overpotentials as low as 0.35 V.

The surface of metal phosphides can be oxidized and generate metal phosphate and hydroxide/oxo-hydroxide moieties in-situ under the OER catalytic conditions, which are expected to be highly active species toward water oxidation catalysis. However, after a long reaction time, both catalysts showed modest decreases in activities, ascribed to loss of phosphate from the catalyst surface and surface overoxidation.

Finally, we successfully assembled a series of hybrid aerogels, containing preformed Ni_2P nanoparticles and CdS nanoparticles, for HER photocatalysis. The nanoparticle components remained their original crystal structure and the resultant aerogels exhibit a meso/macroporous structure with a high specific surface area. The 0.5% Ni_2P/CdS hybrid aerogel has a H_2 evolution rate of 778 $\mu mol \cdot h^{-1} mg^{-1}$ under visible light irradiation. This superior photocatalytic HER performance of the hybrid aerogel is attributed to (1) the small size of CdS and Ni_2P nanoparticles, and their intimate mixing, which can greatly shorten the distance that photogenerated electrons and holes have to travel to surface reaction sites and thus reduce the likelihood of electron-hole recombination; (2) the meso/macroporous structure, which allows for efficient absorption and internal scattering of light (enhanced light harvesting) and enables rapid flux of reactants to, and products from, those sites; and (3) the fast charge separation at the CdS/Ni_2P interface, which again reduces the possibility of electron-hole recombination and improves the catalytic activity.

8.2 Prospectus

8.2.1 Application of Synthetic Methods to New More Metal Phosphides

For HER catalysis, P can act as proton acceptor on the surface and thus facilitate the H_2 generation.[75] While for lithium-ion battery materials, a P-rich system is expected to have a higher capacity than a metal-rich system.[14] So the strategy developed in the dissertation research (high temperature, extended reaction time, high TOP/OAm ratio etc.) to prepare more P-rich nickel phosphide nanoparticles should be applicable to other metal phosphide systems (both binary and ternary phases), thus facilitating the development of this important class of nanomaterials for energy storage and catalysis.

In the case of synthesizing $Fe_{2-x}Mn_xP$, an extra injection of Mn-precursor successfully increase the Mn incorporation from 0.7 to 0.9, because it provides more Mn precursor available in solution. Therefore, increasing the injection amount of Mn or performing multiple injection is expected to yield more Mn-rich phases.

$Co_{2-x}Mn_xP$ and $Fe_{2-x}Mn_xP$ nanoparticles have been synthesized through decomposition of metal carbonyl species in a hot solution, followed by reaction with TOP into relative phosphides. It is anticipated that $Ni_{2-x}Mn_xP$ may be able to accessed through similar method. Because $Ni(CO)_4$ has a low boiling point (43 ºC) and ix extremely toxic, which makes it difficult to handle, $Ni(COD)_2$ should be used as a suitable zero-valent Ni precursor.

8.2.2 Improving OER Activity of Transition Metal Phosphide Nanomaterials

Both $Co_{2-x}Mn_xP$ and $Fe_{2-x}Mn_xP$ show composition-dependent OER activities, but there are also other factors that affect OER activity, such as particle size, morphology, site occupancy (tetrahedral *vs.* square pyramidal), surface area, and

corrosion. Modification of particle size and morphology is expected to expose more active facets on the surface and increase the electroactive surface area. The electronic characteristics will depend on distributions of the two-metal site occupancy. Addressing these factors is expected to yield better-performing transition metal phosphide materials for OER catalysis.

In the case of $Co_{2-x}Fe_xP$ nanoparticles, the smaller particle size can be achieved by decreasing the OAm/metal ratio, increasing the surface area. Morphology can be controlled by using a different intermediate step: converting CoFe alloy to CoFeP results in a particle with scalloped edges while $CoFeO_2$ to CoFeP results in large particles adopting the shape of a sea urchin. Low temperature synthesis method or electro-deposition techniques can be used to prepare amorphous materials form which different heating profiles will lead to materials with varied crystallinity. The metastable phases may exhibit site occupancies that differ from the thermodynamically dictated distribution in bulk materials (monitored by Mossbauer in Fe-containing phases), enabling further tuning of properties.

An alternative approach to increase surface area is to create porous electrode assemblies. Metal phosphide nanoparticles can be assembled through metal cation crosslinking or oxidation-induced gelation method,[144, 145] resulting in aerogels with high intrinsic surface areas, transforming a planar 2-D electrode into an accessible 3-D electrode. which is desired for the OER/HER electrocatalysis.

Corrosion plays an important role in activity. The surface of metal phosphides oxidizes, generating metal phosphate and hydroxide/oxo-hydroxide moieties in-

situ under the OER catalytic condition, which are expected to be highly active species toward water oxidation catalysis. Thus, phosphide aerogels prepared by the oxidation-induced gelation method will have particles with oxidized surfaces that are connected by phosphate species, which makes it an interesting material for the OER catalysis. The pre-oxidized surface may preempt the activation process, or the phosphate “bridge” may act as a proton acceptor; either will result in an enhanced catalytic activity.

The corrosion process is, nevertheless, deleterious over time. Metal phosphide nanoparticles showed modest decreases in the OER activities with time, ascribed to the loss of phosphate species from the catalyst surface. Therefore, using a phosphate buffer should be explored as a means to slow the leaching rate of phosphate into solution, resulting in an enhanced stability.

8.2.3 Exploiting Our Tool Box for Hybrid Aerogel Catalyst Formation

In the dissertation research, a protocol was established for the assembly of CdS and Ni_2P nanoparticles into a hybrid aerogel system with high surface area and photocatalytic hydrogen evolution activity. It should be straightforward to swap out the component in this system to further increase the HER activity or generate catalysts for other applications. For example, replacing Ni_2P with CoFeP nanoparticles is expected to result in an enhanced HER activity (based on the relative electrocatalytic performances of Ni_2P and CoFeP for HER) while replacing CdS with TiO_2 and Ni_2P with $M_{2-x}Mn_xP$ may result in a system for efficient OER photocatalysis. In addition, by changing gelation parameters, such as surface

ligand or oxidant concentration, the kinetics of gelation can be altered to modify surface area and pore characteristics and thus affects the HER catalytic activity.

APPENDIX A. COMPARISON OF THE OER ACTIVITIES OF THE COMNP CATALYSTS WITH RECENTLY PUBLISHED RESULTS (CHAPTER 5)

Table A1. Comparison of the OER activities of the CoMnP catalysts reported here in alkaline conditions with recently published results

Materials	Overpotential at 10 mA cm^{-2} (mV)	Electrolyte	Main Paper Reference [SI reference]
IrO_2	320	1 M KOH	2[146]
IrO_2	320	1 M KOH	11[89]
NiO_x	360	0.5 M KOH	23[147]
$MnCo_2O_4$/N-rmGO (~0.24 mg/cm^2)	340	1 M KOH	8[148]
CoP nanorods/C (0.71 mg/cm^2)	340	1 M KOH	11[4]
CoP nanoparticles/C (0.71 mg/cm^2)	320	1 M KOH	11[4]
Ni_2P nanowires (~0.10 mg/cm^2)	400	1 M KOH	9[19]
Ni_2P nanoparticles (~0.10 mg/cm^2)	500	1 M KOH	9[19]
CoFeP (~0.57 mg/cm^2)	370	0.1 M KOH	16[26]
CoP/C (0.40 mg/cm^2)	360	0.1 M KOH	24[100]
CoP hollow polyhedrons (~0.10 mg/cm^2)	400	1 M KOH	13[25]
Ni_2P/Ni foam (0.14 mg/cm^2)	290	1 M KOH	10[88]
CoP nanoparticles/C nanotubes (0.29 mg/cm^2)	330	0.1 M NaOH	14[24]
CoMnP nanoparticles (0.28 mg/cm^2)	330	1 M KOH	This work

APPENDIX B. TEM IMAGES, PXRD PATTERNS, AND ELECTROCATALYTIC OXYGEN EVOLUTION PROPERTIES OF DIFFERENT COMPOSITIONS OF $CO_{2-X}MN_XP$ NANOPARTICLES (CHAPTER 5)

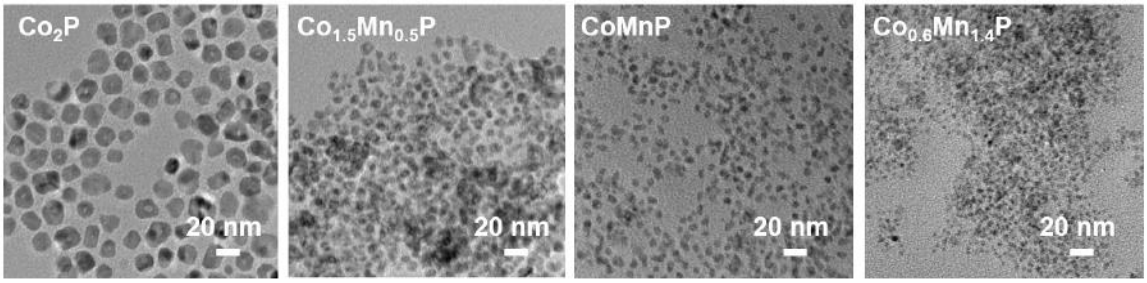

Figure B1 TEM images of different compositions of $Co_{2-x}Mn_xP$ nanoparticles.

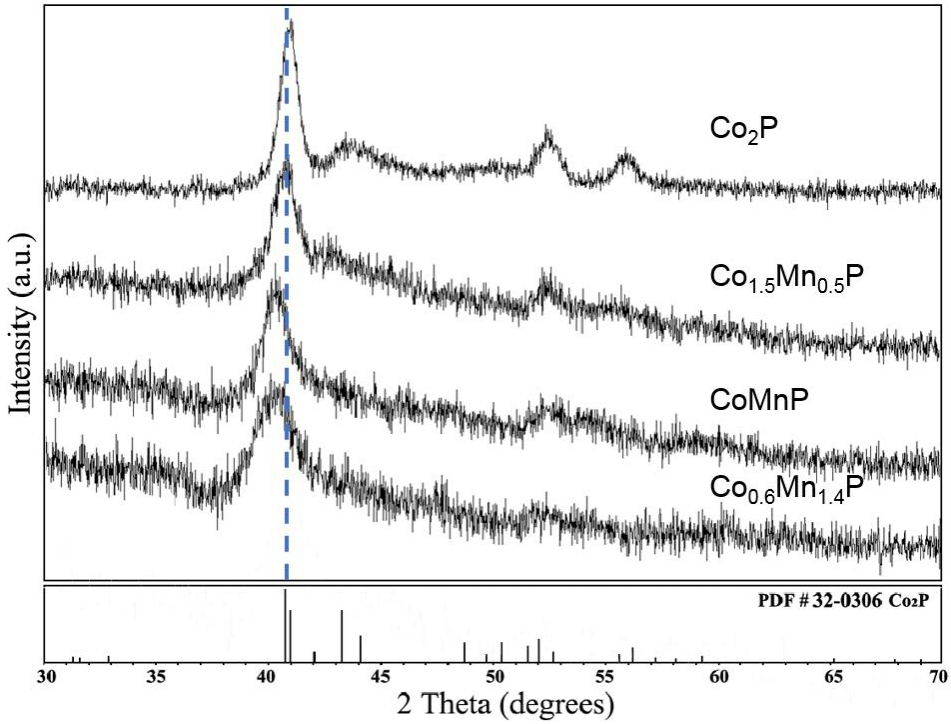

Figure B2 PXRD patterns of different compositions of $Co_{2-x}Mn_xP$ nanoparticles.

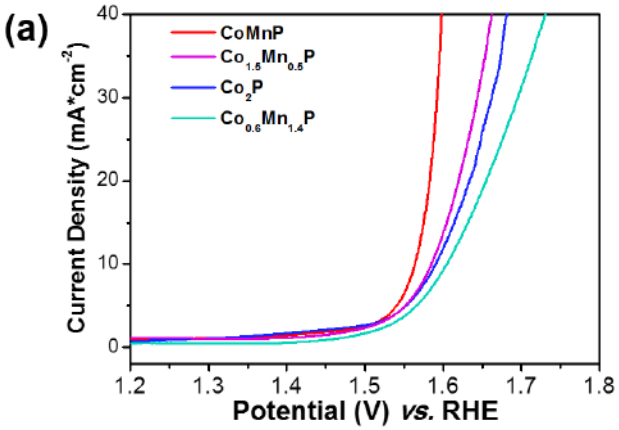

(b)

Catalyst	Overpotential (V)
Co_2P	0.37
$Co_{1.5}Mn_{0.5}P$	0.36
CoMnP	0.33
$Co_{0.6}Mn_{1.4}P$	0.39

Figure B3 Electrocatalytic oxygen evolution properties of $Co_{2-x}Mn_xP$ nanoparticles: (a) Polarization curves of the $Co_{2-x}Mn_xP$ nanorods in 1.0 M KOH; (b) overpotentials required at j = 10 mA/cm^2.

Figure B1 shows TEM images of different compositions of $Co_{2-x}Mn_xP$ nanoparticles, the average size changed from 17.7 to 6.1 to 4.1 to 3.2 nm when the x changed from 0 to 0.5 to 1 to 1.4. The peaks in Co_2P around 40.7° and is slightly shifted toward lower 2 theta values as the content of the bigger volume atom Mn increased (**Figure B2**), indicative of solid-solution formation. **Figure B3** shows the composition dependent properties of the OER catalysis.

APPENDIX C. COMPARISON OF THE OER ACTIVITIES OF THE $FE_{1.1}MN_{0.9}P$ CATALYST WITH RECENTLY PUBLISHED RESULTS (CHAPTER 6)

Table C1. Comparison of the OER activities of the $Fe_{1.1}Mn_{0.9}P$ catalysts reported here in alkaline conditions with recently published results

Materials	Overpotential at 10 mA cm^{-2} (mV)	Electrolyte	Main Paper Reference[SI] reference
IrO_2	320	1 M KOH	3[42]
IrO_2	360	1 M KOH	9[21]
IrO_2	470	0.1 M KOH	37[121]
CoP nanorods/C (0.71 mg/cm^2)	340	1 M KOH	11[89]
CoP nanoparticles/C (0.71 mg/cm^2)	320	1 M KOH	11[89]
Ni_2P nanowires/FTO (~0.10 mg/cm^2)	400	1 M KOH	7[19]
Ni_2P nanoparticles/FTO (~0.10 mg/cm^2)	500	1 M KOH	7[19]
FeP@Au nanoparticles (0.2 mg/cm^2)	320	1 M KOH	39[123]
NiCoP/rGO hybrids (0.15 mg/cm^2)	270	1 M KOH	40[124]
CoFeP (~0.57 mg/cm^2)	370	0.1 M KOH	14[26]
CoP/C (0.40 mg/cm^2)	360	0.1 M KOH	38[100]
CoP hollow polyhedrons (~0.10 mg/cm^2)	400	1 M KOH	13[25]
$Fe_{1.1}Mn_{0.9}P$ nanoparticles (0.28 mg/cm^2)	350	1 M KOH	This work

APPENDIX D. PERMISSION/LICENSE AGREEMENT FOR COPYRIGHT MATERIALS

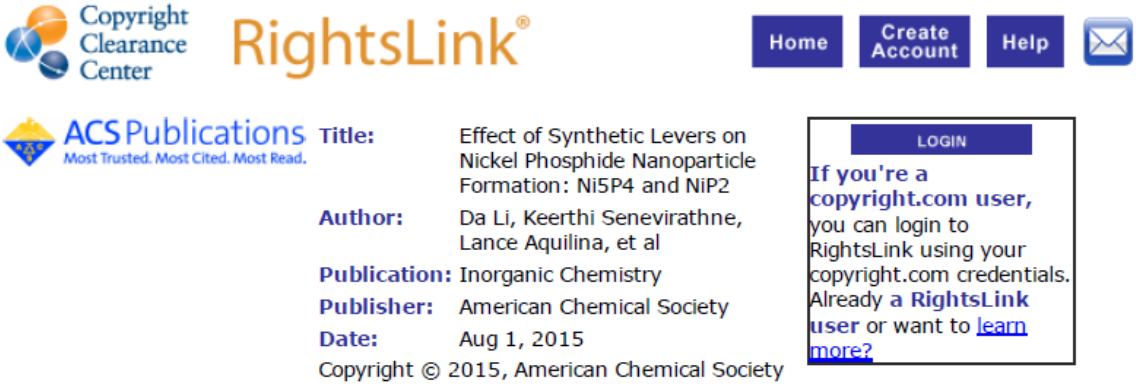

PERMISSION/LICENSE IS GRANTED FOR YOUR ORDER AT NO CHARGE

This type of permission/license, instead of the standard Terms & Conditions, is sent to you because no fee is being charged for your order. Please note the following:

- Permission is granted for your request in both print and electronic formats, and translations.
- If figures and/or tables were requested, they may be adapted or used in part.
- Please print this page for your records and send a copy of it to your publisher/graduate school.
- Appropriate credit for the requested material should be given as follows: "Reprinted (adapted) with permission from (COMPLETE REFERENCE CITATION). Copyright (YEAR) American Chemical Society." Insert appropriate information in place of the capitalized words.
- One-time permission is granted only for the use specified in your request. No additional uses are granted (such as derivative works or other editions). For any other uses, please submit a new request.

BACK CLOSE WINDOW

BIBLIOGRAPHY

(1) Brock, S. L.; Perera, S. C.; Stamm, K. L. Chemical Routes For Production of Transition-Metal Phosphides on the Nanoscale: Implications For Advanced Magnetic and Catalytic Materials. *Chemistry-A European Journal* **2004,** *10.* 3364-3371.

(2) Brock, S. L.; Senevirathne, K. Recent developments in synthetic approaches to transition metal phosphide nanoparticles for magnetic and catalytic applications. *Journal of Solid State Chemistry* **2008,** *181.* 1552-1559.

(3) Oyama, S. T. Novel catalysts for advanced hydroprocessing: transition metal phosphides. *Journal of Catalysis* **2003,** *216.* 343-352.

(4) Popczun, E. J.; Read, C. G.; Roske, C. W.; Lewis, N. S.; Schaak, R. E. Highly Active Electrocatalysis of the Hydrogen Evolution Reaction by Cobalt Phosphide Nanoparticles**. *Angew. Chem. Int. Ed.* **2014,** *53.* 5427-5430.

(5) Savithra, G. H. L.; Muthuswamy, E.; Bowker, R. H.; Carrillo, B. A.; Bussell, M. E.; Brock, S. L. Rational Design of Nickel Phosphide Hydrodesulfurization Catalysts: Controlling Particle Size and Preventing Sintering. *Chemistry of Materials* **2013,** *25.* 825-833.

(6) Muthuswamy, E.; Kharel, P. R.; Lawes, G.; Brock, S. L. Control of Phase in Phosphide Nanoparticles Produced by Metal Nanoparticle Transformation: Fe2P and FeP. *Acs Nano* **2009,** *3.* 2383-2393.

(7) Gaudette, A. F.; Burns, A. W.; Hayes, J. R.; Smith, M. C.; Bowker, R. H.; Seda, T.; Bussell, M. E. Mossbauer spectroscopy investigation and hydrodesulfurization properties of iron-nickel phosphide catalysts. *Journal of Catalysis* **2010,** *272.* 18-27.

(8) Senevirathne, K.; Burns, A. W.; Bussell, M. E.; Brock, S. L. Synthesis and characterization of discrete nickel phosphide nanoparticles: Effect of surface ligation

chemistry on catalytic hydrodesulfurization of thiophene. *Advanced Functional Materials* **2007,** *17.* 3933-3939.

(9) Ha, D. H.; Moreau, L. M.; Bealing, C. R.; Zhang, H. T.; Hennig, R. G.; Robinson, R. D. The structural evolution and diffusion during the chemical transformation from cobalt to cobalt phosphide nanoparticles. *Journal of Materials Chemistry* **2011,** *21.* 11498-11510.

(10) Badari, C. A.; Lonyi, F.; Drotar, E.; Kaszonyi, A.; Valyon, J. A study of the hydrodenitrogenation of propylamine over supported nickel phosphide catalysts using amorphous and nanostructured silica supports. *Applied Catalysis B-Environmental* **2015,** *164.* 48-60.

(11) Sawhill, S. J.; Layman, K. A.; Van Wyk, D. R.; Engelhard, M. H.; Wang, C.; Bussell, M. E. Thiophene hydrodesulfurization over nickel phosphide catalysts: effect of the precursor composition and support. *Journal of Catalysis* **2005,** *231.* 300-313.

(12) Wang, J. L.; Yang, Q.; Zhang, Z. D.; Sun, S. H. Phase-Controlled Synthesis of Transition-Metal Phosphide Nanowires by Ullmann-Type Reactions. *Chemistry-A European Journal* **2010,** *16.* 7916-7924.

(13) Ma, J. J.; Ni, S. B.; Lv, X. H.; Yang, X. L.; Zhang, L. L. The preparation of Ni5P4/Ni composite via a chemical corrosion method and its application in lithium ion batteries. *Materials Letters* **2014,** *133.* 94-96.

(14) Aso, K.; Hayashi, A.; Tatsumisago, M. Phase-Selective Synthesis of Nickel Phosphide in High-Boiling Solvent for All-Solid-State Lithium Secondary Batteries. *Inorganic Chemistry* **2011,** *50.* 10820-10824.

(15) Dismukes, G. C.; Laursen, A. B.; Patraju, K. R.; Whitaker, M.; Retuerto, M.; Sarkar, T.; Yao, N.; Ramanujachary, K. V.; Greenblatt, M. Nanocrystalline Ni5P4: A hydrogen evolution electrocatalyst of exceptional efficiency in both alkaline and acidic media. *Energy & Environmental Science* **2015,** *8.* 1027-1034.

(16) Jiang, P.; Liu, Q.; Sun, X. P. NiP2 nanosheet arrays supported on carbon cloth: an efficient 3D hydrogen evolution cathode in both acidic and alkaline solutions. *Nanoscale* **2014,** *6.* 13440-13445.

(17) Popczun, E. J.; McKone, J. R.; Read, C. G.; Biacchi, A. J.; Wiltrout, A. M.; Lewis, N. S.; Schaak, R. E. Nanostructured Nickel Phosphide as an Electrocatalyst for the Hydrogen Evolution Reaction. *Journal of the American Chemical Society* **2013,** *135.* 9267-9270.

(18) Stern, L.-A.; Feng, L.; Song, F.; Hu, X. Ni_2P as a Janus Catalyst for Water Splitting: The Oxygen Evolution Activity of Ni_2P Nanoparticles. *Energy Environ. Sci.* **2015,** *8.* 2347-2351.

(19) Han, A.; Chen, H. L.; Sun, Z. J.; Xu, J.; Du, P. W. High Catalytic Activity for Water Oxidation Based on Nanostructured Nickel Phosphide Precursors. *Chemical Communications* **2015,** *51.* 11626-11629.

(20) Li, J.; Li, J.; Zhou, X.; Xia, Z.; Gao, W.; Ma, Y.; Qu, Y. Highly Efficient and Robust Nickel Phosphides as Bifunctional Electrocatalysts for Overall Water-Splitting. *ACS Applied Materials & Interfaces* **2016,** *8.* 10826-10834.

(21) Dutta, A.; Samantara, A. K.; Dutta, S. K.; Jena, B. K.; Pradhan, N. Surface-Oxidized Dicobalt Phosphide Nanoneedles as a Nonprecious, Durable, and Efficient OER Catalyst. *ACS Energy Letters* **2016,** *1.* 169-174.

(22) Read, C. G.; Callejas, J. F.; Holder, C. F.; Schaak, R. E. General Strategy for the Synthesis of Transition Metal Phosphide Films for Electrocatalytic Hydrogen and Oxygen Evolution. *ACS Applied Materials & Interfaces* **2016,** *8.* 12798-12803.

(23) Chang, J.; Xiao, Y.; Xiao, M.; Ge, J.; Liu, C.; Xing, W. Surface Oxidized Cobalt-Phosphide Nanorods as an Advanced Oxygen Evolution Catalyst in Alkaline Solution. *ACS Catal.* **2015,** *5.* 6874-6878.

(24) Hou, C.-C.; Cao, S.; Fu, W.-F.; Chen, Y. Ultrafine CoP Nanoparticles Supported on Carbon Nanotubes as Highly Active Electrocatalyst for Both Oxygen and Hydrogen Evolution in Basic Media. *ACS Applied Materials & Interfaces* **2015,** *7.* 28412-28419.

(25) Liu, M.; Li, J. Cobalt Phosphide Hollow Polyhedron as Efficient Bifunctional Electrocatalysts for the Evolution Reaction of Hydrogen and Oxygen. *ACS Applied Materials & Interfaces* **2016,** *8.* 2158-2165.

(26) Mendoza-Garcia, A.; Zhu, H. Y.; Yu, Y. S.; Li, Q.; Zhou, L.; Su, D.; Kramer, M. J.; Sun, S. H. Controlled Anisotropic Growth of Co-Fe-P from Co-Fe-O Nanoparticles. *Angewandte Chemie-International Edition* **2015,** *54.* 9642-9645.

(27) Li, Y.; Zhang, H.; Jiang, M.; Kuang, Y.; Sun, X.; Duan, X. Ternary NiCoP Nanosheet Arrays: An Excellent Bifunctional Catalyst for Alkaline Overall Water Splitting. *Nano Research* **2016,** *9.* 2251-2259.

(28) Han, A.; Chen, H.; Zhang, H.; Sun, Z.; Du, P. Ternary metal phosphide nanosheets as a highly efficient electrocatalyst for water reduction to hydrogen over a wide pH range from 0 to 14. *Journal of Materials Chemistry A* **2016,** *4.* 10195-10202.

(29) Xing, J.; Li, H.; Ming-Cheng Cheng, M.; Geyer, S. M.; Ng, K. Y. S. Electro-synthesis of 3D porous hierarchical Ni-Fe phosphate film/Ni foam as a high-efficiency bifunctional electrocatalyst for overall water splitting. *Journal of Materials Chemistry A* **2016,** *4.* 13866-13873.

(30) Henkes, A. E.; Schaak, R. E. Trioctylphosphine: A general phosphorus source for the low-temperature conversion of metals into metal phosphides. *Chemistry of Materials* **2007,** *19.* 4234-4242.

(31) Henkes, A. E.; Vasquez, Y.; Schaak, R. E. Converting Metals into Phosphides: A General Strategy for the Synthesis of Metal Phosphide Nanocrystals. *Journal of the American Chemical Society* **2007,** *129.* 1896-1897.

(32) Muthuswamy, E.; Savithra, G. H. L.; Brock, S. L. Synthetic Levers Enabling Independent Control of Phase, Size, and Morphology in Nickel Phosphide Nanoparticles. *Acs Nano* **2011,** *5.* 2402-2411.

(33) Barry, B. M.; Gillan, E. G. Low-temperature solvothermal synthesis of phosphorus-rich transition-metal phosphides. *Chemistry of Materials* **2008,** *20.* 2618-2620.

(34) Perera, S. C.; Fodor, P. S.; Tsoi, G. M.; Wenger, L. E.; Brock, S. L. Application of De-silylation Strategies to the Preparation of Transition Metal Pnictide Nanocrystals: The Case of FeP. *Chemistry of Materials* **2003,** *15.* 4034-4038.

(35) Park, J.; Koo, B.; Hwang, Y.; Bae, C.; An, K.; Park, J.-G.; Park, H. M.; Hyeon, T. Novel Synthesis of Magnetic Fe2P Nanorods from Thermal Decomposition of Continuously Delivered Precursors using a Syringe Pump. *Angewandte Chemie* **2004,** *116.* 2332-2335.

(36) Ye, E. Y.; Zhang, S. Y.; Lim, S. H.; Bosman, M.; Zhang, Z. H.; Win, K. Y.; Han, M. Y. Ternary Cobalt-Iron Phosphide Nanocrystals with Controlled Compositions, Properties, and Morphologies from Nanorods and Nanorice to Split Nanostructures. *Chemistry-a European Journal* **2011,** *17.* 5982-5988.

(37) Perera, S. C.; Tsoi, G.; Wenger, L. E.; Brock, S. L. Synthesis of MnP Nanocrystals by Treatment of Metal Carbonyl Complexes with Phosphines: A New, Versatile Route to Nanoscale Transition Metal Phosphides. *Journal of the American Chemical Society* **2003,** *125.* 13960-13961.

(38) Gregg, K. A.; Perera, S. C.; Lawes, G.; Shinozaki, S.; Brock, S. L. Controlled synthesis of MnP nanorods: Effect of shape anisotropy on magnetization. *Chemistry of Materials* **2006,** *18.* 879-886.

(39) Liyanage, D. R.; Danforth, S. J.; Liu, Y.; Bussell, M. E.; Brock, S. L. Simultaneous Control of Composition, Size, and Morphology in Discrete $Ni_{2-x}Co_xP$ Nanoparticles. *Chem. Mater.* **2015,** *27.* 4349-4357.

(40) Hitihami-Mudiyanselage, A.; Arachchige, M. P.; Seda, T.; Lawes, G.; Brock, S. L. Synthesis and Characterization of Discrete $Fe_xNi_{2-x}P$ Nanocrystals ($0 < x < 2$): Compositional Effects on Magnetic Properties. *Chem. Mater.* **2015,** *27.* 6592-6600.

(41) Colson, A. C.; Whitmire, K. H. Synthesis of Fe2–xMnxP Nanoparticles from Single-Source Molecular Precursors. *Chemistry of Materials* **2011,** *23.* 3731-3739.

(42) McCrory, C. C. L.; Jung, S.; Peters, J. C.; Jaramillo, T. F. Benchmarking Heterogeneous Electrocatalysts for the Oxygen Evolution Reaction. *Journal of the American Chemical Society* **2013,** *135.* 16977-16987.

(43) Frame, F. A.; Townsend, T. K.; Chamousis, R. L.; Sabio, E. M.; Dittrich, T.; Browning, N. D.; Osterloh, F. E. Photocatalytic Water Oxidation with Nonsensitized IrO2 Nanocrystals under Visible and UV Light. *Journal of the American Chemical Society* **2011,** *133.* 7264-7267.

(44) Brück, E.; Tegus, O.; Cam Thanh, D. T.; Trung, N. T.; Buschow, K. H. J. A review on Mn based materials for magnetic refrigeration: Structure and properties. *International Journal of Refrigeration* **2008,** *31.* 763-770.

(45) Jeong, D.; Jin, K.; Jerng, S. E.; Seo, H.; Kim, D.; Nahm, S. H.; Kim, S. H.; Nam, K. T. Mn5O8 Nanoparticles as Efficient Water Oxidation Catalysts at Neutral pH. *Acs Catalysis* **2015,** *5.* 4624-4628.

(46) Jin, K.; Park, J.; Lee, J.; Yang, K. D.; Pradhan, G. K.; Sim, U.; Jeong, D.; Jang, H. L.; Park, S.; Kim, D.; Sung, N. E.; Kim, S. H.; Han, S.; Nam, K. T. Hydrated Manganese(II) Phosphate (Mn-3(PO4)(2)center dot 3H(2)O) as a Water Oxidation Catalyst. *Journal of the American Chemical Society* **2014,** *136.* 7435-7443.

(47) Jin, K.; Chu, A.; Park, J.; Jeong, D.; Jerng, S. E.; Sim, U.; Jeong, H. Y.; Lee, C. W.; Park, Y. S.; Yang, K. D.; Pradhan, G. K.; Kim, D.; Sung, N. E.; Kim, S. H.; Nam, K. T. Partially Oxidized Sub-10 nm MnO Nanocrystals with High Activity for Water Oxidation Catalysis. *Scientific Reports* **2015,** *5.*

(48) Kuo, C. H.; Mosa, I. M.; Poyraz, A. S.; Biswas, S.; E-Sawy, A. M.; Song, W. Q.; Luo, Z.; Chen, S. Y.; Rusling, J. F.; He, J.; Suib, S. L. Robust Mesoporous Manganese Oxide Catalysts for Water Oxidation. *Acs Catalysis* **2015,** *5.* 1693-1699.

(49) Liang, Y. Y.; Wang, H. L.; Zhou, J. G.; Li, Y. G.; Wang, J.; Regier, T.; Dai, H. J. Covalent Hybrid of Spinel Manganese-Cobalt Oxide and Graphene as Advanced Oxygen Reduction Electrocatalysts. *Journal of the American Chemical Society* **2012,** *134.* 3517-3523.

(50) Dung, N. H.; Ou, Z. Q.; Caron, L.; Zhang, L.; Thanh, D. T. C.; de Wijs, G. A.; de Groot, R. A.; Buschow, K. H. J.; Brück, E. Mixed Magnetism for Refrigeration and Energy Conversion. *Advanced Energy Materials* **2011,** *1.* 1215-1219.

(51) Hoglin, V.; Cedervall, J.; Andersson, M. S.; Sarkar, T.; Hudl, M.; Nordblad, P.; Andersson, Y.; Sahlberg, M. Phase Diagram, Structures and Magnetism of the $FeMnP_{1-x}Si_x$ System. *RSC Adv.* **2015,** *5.* 8278-8284.

(52) Hudl, M.; Häggström, L.; Delczeg-Czirjak, E.-K.; Höglin, V.; Sahlberg, M.; Vitos, L.; Eriksson, O.; Nordblad, P.; Andersson, Y. Strongly Enhanced Magnetic Moments in Ferromagnetic $FeMnP_{0.5}Si_{0.5}$. *Appl. Phys. Lett.* **2011,** *99.* 152502.

(53) Fruchart, R.; Roger, A.; Senateur, J. P. Crystallographic and Magnetic Properties of Solid Solutions of Phosphides M_2P M=Cr Mn Fe Co and Ni. *J. Appl. Phys.* **1969,** *40.* 1250-&.

(54) Fruchart, R.; Roger, A.; Sendteur, J. P. Crystallographic and Magnetic Properties of Solid Solutions of Phosphides M2P M=Cr Mn Fe Co and Ni. *Journal of Applied Physics* **1969,** *40.* 1250-&.

(55) Balli, M.; Fruchart, D.; Gignoux, D.; Tobola, J.; Hlil, E. K.; Wolfers, P.; Zach, R. Magnetocaloric effect in ternary metal phosphides (Fe1-xNix)(2)P. *Journal of Magnetism and Magnetic Materials* **2007,** *316.* 358-360.

(56) Guillou, F.; Bruck, E. Tuning the metamagnetic transition in the (Co, Fe)MnP system for magnetocaloric purposes. *Journal of Applied Physics* **2013,** *114.*

(57) Guo, J.; Yang, W.; Wang, C. Magnetic Colloidal Supraparticles: Design, Fabrication and Biomedical Applications. *Advanced Materials* **2013,** *25.* 5196-5214.

(58) Hettiarachchi, M. A.; Abdelhamid, E.; Nadgorny, B.; Brock, S. L. Synthesis of colloidal MnSb nanoparticles: consequences of size and surface characteristics on magnetic properties. *Journal of Materials Chemistry C* **2016,** *4.* 6790-6797.

(59) Howe, J.; Fultz, B., *Transmission Electron Microscopy and Diffractometry of Materials*. Springer: Berlin, 2001.

(60) Williams, D.; Carter, B., *Transmission Electron Microscopy*. Springer: 1996.

(61) Carenco, S.; Boissiere, C.; Nicole, L.; Sanchez, C.; Le Floch, P.; Mezailles, N. Controlled Design of Size-Tunable Monodisperse Nickel Nanoparticles. *Chemistry of Materials* **2010,** *22.* 1340-1349.

(62) Moreau, L. M.; Ha, D.-H.; Bealing, C. R.; Zhang, H.; Hennig, R. G.; Robinson, R. D. Unintended Phosphorus Doping of Nickel Nanoparticles during Synthesis with TOP: A Discovery through Structural Analysis. *Nano Letters* **2012,** *12.* 4530-4539.

(63) Carenco, S.; Hu, Y.; Florea, I.; Ersen, O.; Boissiere, C.; Mezailles, N.; Sanchez, C. Metal-Dependent Interplay between Crystallization and Phosphorus Diffusion during the Synthesis of Metal Phosphide Nanoparticles. *Chemistry of Materials* **2012,** *24.* 4134-4145.

(64) Wang, J. W.; Johnston-Peck, A. C.; Tracy, J. B. Nickel Phosphide Nanoparticles with Hollow, Solid, and Amorphous Structures. *Chemistry of Materials* **2009,** *21.* 4462-4467.

(65) Moreau, L. M.; Ha, D. H.; Zhang, H. T.; Hoyden, R.; Muller, D. A.; Robinson, R. D. Defining Crystalline/Amorphous Phases of Nanoparticles through X-ray Absorption Spectroscopy and X-ray Diffraction: The Case of Nickel Phosphide. *Chemistry of Materials* **2013,** *25.* 2394-2403.

(66) Xia, Y.; Tang, Z. Monodisperse inorganic supraparticles: formation mechanism, properties and applications. *Chemical Communications* **2012,** *48.* 6320-6336.

(67) Liu, J.; Sun, Z. K.; Deng, Y. H.; Zou, Y.; Li, C. Y.; Guo, X. H.; Xiong, L. Q.; Gao, Y.; Li, F. Y.; Zhao, D. Y. Highly Water-Dispersible Biocompatible Magnetite Particles with Low Cytotoxicity Stabilized by Citrate Groups. *Angewandte Chemie-International Edition* **2009,** *48.* 5875-5879.

(68) Naravanaswamy, A.; Xu, H.; Pradhan, N.; Peng, X. Crystalline nanoflowers with different chemical compositions and physical properties grown by limited ligand protection. *Angewandte Chemie-International Edition* **2006,** *45.* 5361-5364.

(69) Xia, Y.; Trung Dac, N.; Yang, M.; Lee, B.; Santos, A.; Podsiadlo, P.; Tang, Z.; Glotzer, S. C.; Kotov, N. A. Self-assembly of self-limiting monodisperse supraparticles from polydisperse nanoparticles. *Nature Nanotechnology* **2011,** *6.* 580-587.

(70) Hitihami-Mudiyanselage, A.; Arachchige, M. P.; Seda, T.; Lawes, G.; Brock, S. L. Synthesis and Characterization of Discrete FexNi2-xP Nanocrystals (0 < x < 2): Compositional Effects on Magnetic Properties. *Chemistry of Materials* **2015,** *27.* 6592-6600.

(71) Danforth, S. J.; Liyanage, D. R.; Hitihami-Mudiyanselage, A.; Ilic, B.; Brock, S. L.; Bussell, M. E. Probing hydrodesulfurization over bimetallic phosphides using monodisperse Ni2-xMxP nanoparticles encapsulated in mesoporous silica. *Surface Science*.

(72) Colson, A. C.; Whitmire, K. H. Synthesis of Fe2-xMnxP Nanoparticles from Single-Source Molecular Precursors. *Chem. Mater.* **2011,** *23.* 3731-3739.

(73) Kibsgaard, J.; Tsai, C.; Chan, K.; Benck, J. D.; Norskov, J. K.; Abild-Pedersen, F.; Jaramillo, T. F. Designing an improved transition metal phosphide catalyst for hydrogen evolution using experimental and theoretical trends. *Energy & Environmental Science* **2015,** *8.* 3022-3029.

(74) Burns, A. W.; Gaudette, A. F.; Bussell, M. E. Hydrodesulfurization properties of cobalt-nickel phosphide catalysts: Ni-rich materials are highly active. *Journal of Catalysis* **2008,** *260.* 262-269.

(75) Callejas, J. F.; Read, C. G.; Popczun, E. J.; McEnaney, J. M.; Schaak, R. E. Nanostructured Co2P Electrocatalyst for the Hydrogen Evolution Reaction and Direct Comparison with Morphologically Equivalent CoP. *Chemistry of Materials* **2015,** *27.* 3769-3774.

(76) Popczun, E. J.; Roske, C. W.; Read, C. G.; Crompton, J. C.; McEnaney, J. M.; Callejas, J. F.; Lewis, N. S.; Schaak, R. E. Highly branched cobalt phosphide nanostructures for hydrogen-evolution electrocatalysis. *Journal of Materials Chemistry A* **2015,** *3.* 5420-5425.

(77) Callejas, J. F.; McEnaney, J. M.; Read, C. G.; Crompton, J. C.; Biacchi, A. J.; Popczun, E. J.; Gordon, T. R.; Lewis, N. S.; Schaak, R. E. Electrocatalytic and Photocatalytic Hydrogen Production from Acidic and Neutral-pH Aqueous Solutions Using Iron Phosphide Nanoparticles. *Acs Nano* **2014,** *8.* 11101-11107.

(78) Liyanage, D. R.; Danforth, S. J.; Liu, Y.; Bussell, M. E.; Brock, S. L. Simultaneous Control of Composition, Size, and Morphology in Discrete Ni2-xCoxP Nanoparticles. *Chemistry of Materials* **2015,** *27.* 4349-4357.

(79) Seo, W. S.; Shim, J. H.; Oh, S. J.; Lee, E. K.; Hur, N. H.; Park, J. T. Phase- and size-controlled synthesis of hexagonal and cubic CoO nanocrystals. *Journal of the American Chemical Society* **2005,** *127.* 6188-6189.

(80) Chiang, R. K.; Chiang, R. T. Formation of hollow Ni2P nanoparticles based on the nanoscale Kirkendall effect. *Inorganic Chemistry* **2007,** *46.* 369-371.

(81) Oyama, S. T.; Lee, Y. K. The active site of nickel phosphide catalysts for the hydrodesulfurization of 4,6-DMDBT. *Journal of Catalysis* **2008,** *258.* 393-400.

(82) Pan, Y.; Liu, Y. Q.; Liu, C. G. An efficient method for the synthesis of nickel phosphide nanocrystals via thermal decomposition of single-source precursors. *Rsc Advances* **2015,** *5.* 11952-11959.

(83) Li, D.; Senevirathne, K.; Aquilina, L.; Brock, S. L. Effect of Synthetic Levers on Nickel Phosphide Nanoparticle Formation: Ni5P4 and NiP2. *Inorganic Chemistry* **2015,** *54.* 7968-7975.

(84) Goodenough, J. B. Interpretation of structure and magnetism in transition-metal pnictides M2X and (M1−xM′x)2X. *Journal of Solid State Chemistry* **1973,** *7.* 428-447.

(85) Kumar, S.; Krishnamurthy, A.; Srivastava, B. K., Influence of Co Doping on Structural and Magnetic Properties of Fe(2)P. In *Latest Trends in Condensed Matter Physics: Experimental and Theoretical Aspects*, Singhal, R. K., Ed. Trans Tech Publications Ltd: Stafa-Zurich, 2011; Vol. 171, pp 93-106.

(86) Kumar, S.; Chander, S.; Krishnamurthy, A.; Srivastava, B. K. Magnetic behaviour of alloys in the series (Fe1-xCox)(2)P. *Journal of Magnetism and Magnetic Materials* **2001,** *237.* 135-142.

(87) Lewis, N. S.; Nocera, D. G. Powering the planet: Chemical challenges in solar energy utilization. *P Natl Acad Sci USA* **2007,** *104.* 20142-20142.

(88) Stern, L.-A.; Feng, L.; Song, F.; Hu, X. Ni2P as a Janus catalyst for water splitting: the oxygen evolution activity of Ni2P nanoparticles. *Energy & Environmental Science* **2015,** *8.* 2347-2351.

(89) Chang, J.; Xiao, Y.; Xiao, M.; Ge, J.; Liu, C.; Xing, W. Surface Oxidized Cobalt-Phosphide Nanorods As an Advanced Oxygen Evolution Catalyst in Alkaline Solution. *ACS Catalysis* **2015,** *5.* 6874-6878.

(90) Wang, P.; Song, F.; Amal, R.; Ng, Y. H.; Hu, X. Efficient Water Splitting Catalyzed by Cobalt Phosphide-Based Nanoneedle Arrays Supported on Carbon Cloth. *ChemSusChem* **2016,** n/a-n/a.

(91) Surówka, J.; Budniok, A.; Bzowski, B. e.; Warczewski, J. Electrolytic composite CoPTiO2 layers as electrode materials for oxygen electroevolution. *Thin Solid Films* **1997,** *307.* 233-239.

(92) Mendoza-Garcia, A.; Zhu, H. Y.; Yu, Y. S.; Li, Q.; Zhou, L.; Su, D.; Kramer, M. J.; Sun, S. H. Controlled Anisotropic Growth of Co-Fe-P from Co-Fe-O Nanoparticles. *Angew. Chem. Int. Ed.* **2015,** *54.* 9642-9645.

(93) Mendoza-Garcia, A.; Su, D.; Sun, S. Sea urchin-like cobalt-iron phosphide as an active catalyst for oxygen evolution reaction. *Nanoscale* **2016,** *8.* 3244-3247.

(94) Ha, D.-H.; Moreau, L. M.; Bealing, C. R.; Zhang, H.; Hennig, R. G.; Robinson, R. D. The structural evolution and diffusion during the chemical transformation from cobalt to cobalt phosphide nanoparticles. *Journal of Materials Chemistry* **2011,** *21.* 11498-11510.

(95) Fjellvag, H.; Kjekshus, A. MAGNETIC AND STRUCTURAL-PROPERTIES OF TRANSITION-METAL SUBSTITUTED MNP .1. MN1-TCOTP (0.00 LESS-THAN-OR-EQUAL TO T LESS-THAN-OR-EQUAL TO 0.30). *Acta Chemica Scandinavica Series a-Physical and Inorganic Chemistry* **1984,** *38.* 563-573.

(96) Fujii, S.; Ishida, S.; Asano, S. ELECTRONIC-STRUCTURES AND MAGNETIC-PROPERTIES OF FE2P, CO2P AND COMNP. *Journal of Physics F-Metal Physics* **1988,** *18.* 971-980.

(97) Grosvenor, A. P.; Cavell, R. G.; Mar, A. Next-nearest neighbour contributions to P 2p(3/2) X-ray photoelectron binding energy shifts of mixed transition-metal phosphides M1-xM ' P-x with the MnP-type structure. *Journal of Solid State Chemistry* **2007,** *180.* 2702-2712.

(98) Jung, S.; McCrory, C. C. L.; Ferrer, I. M.; Peters, J. C.; Jaramillo, T. F. Benchmarking nanoparticulate metal oxide electrocatalysts for the alkaline water oxidation reaction. *Journal of Materials Chemistry A* **2016,** *4.* 3068-3076.

(99) Fominykh, K.; Feckl, J. M.; Sicklinger, J.; Doblinger, M.; Bocklein, S.; Ziegler, J.; Peter, L.; Rathousky, J.; Scheidt, E. W.; Bein, T.; Fattakhova-Rohlfing, D. Ultrasmall Dispersible Crystalline Nickel Oxide Nanoparticles as High-Performance Catalysts for Electrochemical Water Splitting. *Advanced Functional Materials* **2014,** *24.* 3123-3129.

(100) Ryu, J.; Jung, N.; Jang, J. H.; Kim, H. J.; Yoo, S. J. In Situ Transformation of Hydrogen-Evolving CoP Nanoparticles: Toward Efficient Oxygen Evolution Catalysts Bearing Dispersed Morphologies with Co-oxo/hydroxo Molecular Units. *Acs Catalysis* **2015,** *5.* 4066-4074.

(101) Surendranath, Y.; Kanan, M. W.; Nocera, D. G. Mechanistic Studies of the Oxygen Evolution Reaction by a Cobalt-Phosphate Catalyst at Neutral pH. *Journal of the American Chemical Society* **2010,** *132.* 16501-16509.

(102) Gileadi, E., *Electrode Kinetics for Chemists, Chemical Engineers and Materials Scientists*. Wiley-VCH: New York, 1993; p 127-184.

(103) Zhang, M.; de Respinis, M.; Frei, H. Time-resolved observations of water oxidation intermediates on a cobalt oxide nanoparticle catalyst. *Nat Chem* **2014,** *6.* 362-367.

(104) Gerken, J. B.; McAlpin, J. G.; Chen, J. Y. C.; Rigsby, M. L.; Casey, W. H.; Britt, R. D.; Stahl, S. S. Electrochemical Water Oxidation with Cobalt-Based Electrocatalysts from pH 0–14: The Thermodynamic Basis for Catalyst Structure, Stability, and Activity. *Journal of the American Chemical Society* **2011,** *133.* 14431-14442.

(105) Kärkäs, M. D.; Verho, O.; Johnston, E. V.; Åkermark, B. Artificial Photosynthesis: Molecular Systems for Catalytic Water Oxidation. *Chemical Reviews* **2014,** *114.* 11863-12001.

(106) Winkler, J. R.; Gray, H. B., Electronic Structures of Oxo-Metal Ions. In *Molecular Electronic Structures of Transition Metal Complexes I*, Mingos, D. M. P.; Day, P.; Dahl, J. P., Eds. Springer: New York, 2012; Vol. 142, pp 17-28.

(107) Blanchard, P. E. R.; Grosvenor, A. P.; Cavell, R. G.; Mar, A. X-ray Photoelectron and Absorption Spectroscopy of Metal-Rich Phosphides M2P and M3P (M = Cr-Ni). *Chemistry of Materials* **2008,** *20.* 7081-7088.

(108) Su, J.; Vayssieres, L. A Place in the Sun for Artificial Photosynthesis? *ACS Energy Letters* **2016,** *1.* 121-135.

(109) Frame, F. A.; Townsend, T. K.; Chamousis, R. L.; Sabio, E. M.; Dittrich, T.; Browning, N. D.; Osterloh, F. E. Photocatalytic Water Oxidation with Nonsensitized IrO_2 Nanocrystals under Visible and UV Light. *J. Am. Chem. Soc.* **2011,** *133.* 7264-7267.

(110) Reier, T.; Oezaslan, M.; Strasser, P. Electrocatalytic Oxygen Evolution Reaction (OER) on Ru, Ir, and Pt Catalysts: A Comparative Study of Nanoparticles and Bulk Materials. *ACS Catalysis* **2012,** *2.* 1765-1772.

(111) Jeong, D.; Jin, K.; Jerng, S. E.; Seo, H.; Kim, D.; Nahm, S. H.; Kim, S. H.; Nam, K. T. Mn_5O_8 Nanoparticles as Efficient Water Oxidation Catalysts at Neutral pH. *ACS Catal.* **2015,** *5.* 4624-4628.

(112) Li, D.; Baydoun, H.; Verani, C. N.; Brock, S. L. Efficient Water Oxidation Using CoMnP Nanoparticles. *Journal of the American Chemical Society* **2016,** *138.* 4006-4009.

(113) Colson, A. C.; Whitmire, K. H. Synthesis of $Fe_{2-x}Mn_xP$ Nanoparticles from Single-Source Molecular Precursors. *Chem. Mater.* **2011,** *23.* 3731-3739.

(114) Gregg, K. A.; Perera, S. C.; Lawes, G.; Shinozaki, S.; Brock, S. L. Controlled Synthesis of MnP Nanorods: Effect of Shape Anisotropy on Magnetization. *Chemistry of Materials* **2006,** *18.* 879-886.

(115) Muthuswamy, E.; Brock, S. L. Oxidation Does Not (Always) Kill Reactivity of Transition Metals: Solution-Phase Conversion of Nanoscale Transition Metal Oxides to

Phosphides and Sulfides. *Journal of the American Chemical Society* **2010,** *132.* 15849-15851.

(116) Thurston, J. H.; Whitmire, K. H. Molecular Precursors for Ferroelectric Materials: Synthesis and Characterization of Bi2M2(μ-O)(sal)4(Hsal)4(OEt)2 and BiM4(μ-O)4(sal)4(Hsal)3(OiPr)4 (sal = O2CC6H4O, Hsal = O2CC6H4OH) (M = Nb, Ta). *Inorganic Chemistry* **2003,** *42.* 2014-2023.

(117) Fernando, D.; Nigro, T. A. E.; Dyer, I. D.; Alia, S. M.; Pivovar, B. S.; Vasquez, Y. Synthesis and Catalytic Activity of the Metastable Phase of Gold Phosphide. *Journal of Solid State Chemistry* **2016,** *242.* 182-192.

(118) Brutchey, R. L. Diorganyl Dichalcogenides as Useful Synthons for Colloidal Semiconductor Nanocrystals. *Accounts of Chemical Research* **2015,** *48.* 2918-2926.

(119) Wang, J.; Singh, A.; Liu, P.; Singh, S.; Coughlan, C.; Guo, Y.; Ryan, K. M. Colloidal Synthesis of Cu_2SnSe_3Tetrapod Nanocrystals. *J. Am Chem. Soc.* **2013,** *135.* 7835-7838.

(120) Norako, M. E.; Brutchey, R. L. Synthesis of Metastable Wurtzite $CuInSe_2$ Nanocrystals. *Chemistry of Materials* **2010,** *22.* 1613-1615.

(121) Lee, Y.; Suntivich, J.; May, K. J.; Perry, E. E.; Shao-Horn, Y. Synthesis and Activities of Rutile IrO2 and RuO2 Nanoparticles for Oxygen Evolution in Acid and Alkaline Solutions. *The Journal of Physical Chemistry Letters* **2012,** *3.* 399-404.

(122) Ryu, J.; Jung, N.; Jang, J. H.; Kim, H.-J.; Yoo, S. J. In Situ Transformation of Hydrogen-Evolving CoP Nanoparticles: Toward Efficient Oxygen Evolution Catalysts Bearing Dispersed Morphologies with Co-oxo/hydroxo Molecular Units. *ACS Catalysis* **2015,** *5.* 4066-4074.

(123) Masud, J.; Umapathi, S.; Ashokaan, N.; Nath, M. Iron phosphide nanoparticles as an efficient electrocatalyst for the OER in alkaline solution. *Journal of Materials Chemistry A* **2016,** *4.* 9750-9754.

(124) Li, J.; Yan, M.; Zhou, X.; Huang, Z.-Q.; Xia, Z.; Chang, C.-R.; Ma, Y.; Qu, Y. Mechanistic Insights on Ternary Ni2−xCoxP for Hydrogen Evolution and Their Hybrids with Graphene as Highly Efficient and Robust Catalysts for Overall Water Splitting. *Advanced Functional Materials* **2016,** *26.* 6785-6796.

(125) Blanchard, P. E. R.; Grosvenor, A. P.; Cavell, R. G.; Mar, A. X-ray Photoelectron and Absorption Spectroscopy of Metal-Rich Phosphides M2P and M3P (M = Cr−Ni). *Chemistry of Materials* **2008,** *20.* 7081-7088.

(126) Xiong, D.; Wang, X.; Li, W.; Liu, L. Facile synthesis of iron phosphide nanorods for efficient and durable electrochemical oxygen evolution. *Chemical Communications* **2016,** *52.* 8711-8714.

(127) Gao, T.; Krumeich, F.; Nesper, R.; Fjellvåg, H.; Norby, P. Microstructures, Surface Properties, and Topotactic Transitions of Manganite Nanorods. *Inorganic Chemistry* **2009,** *48.* 6242-6250.

(128) Long, C.; Jiang, L.; Wei, T.; Yan, J.; Fan, Z. High-performance asymmetric supercapacitors with lithium intercalation reaction using metal oxide-based composites as electrode materials. *Journal of Materials Chemistry A* **2014,** *2.* 16678-16686.

(129) Miao, R.; He, J.; Sahoo, S.; Luo, Z.; Zhong, W.; Chen, S.-Y.; Guild, C.; Jafari, T.; Dutta, B.; Cetegen, S. A.; Wang, M.; Alpay, S. P.; Suib, S. L. Reduced Graphene Oxide Supported Nickel–Manganese–Cobalt Spinel Ternary Oxide Nanocomposites and Their Chemically Converted Sulfide Nanocomposites as Efficient Electrocatalysts for Alkaline Water Splitting. *ACS Catalysis* **2017,** *7.* 819-832.

(130) Yamashita, T.; Hayes, P. Analysis of XPS spectra of Fe2+ and Fe3+ ions in oxide materials. *Applied Surface Science* **2008,** *254.* 2441-2449.

(131) Menezes, P. W.; Indra, A.; Das, C.; Walter, C.; Göbel, C.; Gutkin, V.; Schmeiβer, D.; Driess, M. Uncovering the Nature of Active Species of Nickel Phosphide Catalysts in

High-Performance Electrochemical Overall Water Splitting. *ACS Catalysis* **2016,** *7.* 103-109.

(132) Dutta, A.; Pradhan, N. Developments of Metal Phosphides as Efficient OER Precatalysts. *The Journal of Physical Chemistry Letters* **2016,** *8.* 144-152.

(133) Bajorowicz, B.; Cybula, A.; Winiarski, M. J.; Klimczuk, T.; Zaleska, A. Surface Properties and Photocatalytic Activity of KTaO3, CdS, MoS2 Semiconductors and Their Binary and Ternary Semiconductor Composites. *Molecules* **2014,** *19.* 15339-15360.

(134) Feng, L. G.; Vrubel, H.; Bensimon, M.; Hu, X. L. Easily-prepared dinickel phosphide (Ni2P) nanoparticles as an efficient and robust electrocatalyst for hydrogen evolution. *Physical Chemistry Chemical Physics* **2014,** *16.* 5917-5921.

(135) Cao, S.; Chen, Y.; Wang, C. J.; He, P.; Fu, W. F. Highly efficient photocatalytic hydrogen evolution by nickel phosphide nanoparticles from aqueous solution. *Chemical Communications* **2014,** *50.* 10427-10429.

(136) Moon, J. S.; Jang, J. H.; Kim, E. G.; Chung, Y. H.; Yoo, S. J.; Lee, Y. K. The nature of active sites of Ni2P electrocatalyst for hydrogen evolution reaction. *Journal of Catalysis* **2015,** *326.* 92-99.

(137) Sun, Z. J.; Zheng, H. F.; Li, J. S.; Du, P. W. Extraordinarily efficient photocatalytic hydrogen evolution in water using semiconductor nanorods integrated with crystalline Ni2P cocatalysts. *Energy & Environmental Science* **2015,** *8.* 2668-2676.

(138) Cao, S.; Chen, Y.; Wang, C.-J.; He, P.; Fu, W.-F. Highly efficient photocatalytic hydrogen evolution by nickel phosphide nanoparticles from aqueous solution. *Chemical Communications* **2014,** *50.* 10427-10429.

(139) DeSario, P. A.; Pietron, J. J.; DeVantier, D. E.; Brintlinger, T. H.; Stroud, R. M.; Rolison, D. R. Plasmonic enhancement of visible-light water splitting with Au-TiO2 composite aerogels. *Nanoscale* **2013,** *5.* 8073-8083.

(140) Korala, L.; Germain, J. R.; Chen, E.; Pala, I. R.; Li, D.; Brock, S. L. CdS aerogels as efficient photocatalysts for degradation of organic dyes under visible light irradiation. *Inorganic Chemistry Frontiers* **2017**.

(141) Korala, L.; Wang, Z.; Liu, Y.; Maldonado, S.; Brock, S. L. Uniform Thin Films of CdSe and CdSe(ZnS) Core(Shell) Quantum Dots by Sol–Gel Assembly: Enabling Photoelectrochemical Characterization and Electronic Applications. *ACS Nano* **2013,** *7.* 1215-1223.

(142) Mohanan, J. L.; Arachchige, I. U.; Brock, S. L. Porous Semiconductor Chalcogenide Aerogels. *Science* **2005,** *307.* 397-400.

(143) Layan Savithra, G. H.; Muthuswamy, E.; Bowker, R. H.; Carrillo, B. A.; Bussell, M. E.; Brock, S. L. Rational Design of Nickel Phosphide Hydrodesulfurization Catalysts: Controlling Particle Size and Preventing Sintering. *Chemistry of Materials* **2013,** *25.* 825-833.

(144) Hitihami-Mudiyanselage, A.; Senevirathne, K.; Brock, S. L. Bottom-Up Assembly of Ni2P Nanoparticles into Three-Dimensional Architectures: An Alternative Mechanism for Phosphide Gelation. *Chemistry of Materials* **2014,** *26.* 6251-6256.

(145) Hitihami-Mudiyanselage, A.; Senevirathne, K.; Brock, S. L. Assembly of Phosphide Nanocrystals into Porous Networks: Formation of InP Gels and Aerogels. *ACS Nano* **2013,** *7.* 1163-1170.

(146) McCrory, C. C. L.; Jung, S. H.; Peters, J. C.; Jaramillo, T. F. Benchmarking Heterogeneous Electrocatalysts for the Oxygen Evolution Reaction. *Journal of the American Chemical Society* **2013,** *135.* 16977-16987.

(147) Fominykh, K.; Feckl, J. M.; Sicklinger, J.; Döblinger, M.; Böcklein, S.; Ziegler, J.; Peter, L.; Rathousky, J.; Scheidt, E.-W.; Bein, T.; Fattakhova-Rohlfing, D. Ultrasmall Dispersible Crystalline Nickel Oxide Nanoparticles as High-Performance Catalysts for Electrochemical Water Splitting. *Advanced Functional Materials* **2014,** *24.* 3123-3129.

(148) Liang, Y.; Wang, H.; Zhou, J.; Li, Y.; Wang, J.; Regier, T.; Dai, H. Covalent Hybrid of Spinel Manganese–Cobalt Oxide and Graphene as Advanced Oxygen Reduction Electrocatalysts. *Journal of the American Chemical Society* **2012,** *134.* 3517-3523.

ABSTRACT

SYNTHESIS OF DISCRETE TRANSITION METAL (NI, CO, FE, MN) PHOSPHIDE NANOPARTICLES: COMPOSITIONAL EFFECT ON CATALYTIC AND MAGNETIC PROPERTIES

by

DA LI

December 2017

Advisor: Dr. Stephanie L. Brock

Major: Chemistry (Inorganic)

Degree: Doctor of Philosophy

This dissertation research is focused on the synthesis, characterization of binary and ternary transition metal (Ni, Co, Fe, Mn) phosphide nanomaterials and their catalytic and magnetic properties.

A phase-control strategy enabling the arrested-precipitation synthesis of nanoparticles of Ni_5P_4 and NiP_2 is presented. The composition and purity of the product can be tuned by changing key synthetic levers, including the metal precursor, the oleylamine (OAm) and Trioctylphosphine (TOP) concentrations, temperature, time and the presence or absence of a moderate temperature soak step to facilitate formation of Ni and/or Ni-P amorphous nanoparticle intermediates.

New $Co_xFe_{2-x}P$ nanoparticles ($0 \leq x \leq 2$), $Co_{2-x}Mn_xP$ nanoparticles ($0 \leq x \leq 1.4$), and $Fe_{2-x}Mn_xP$ nanorods ($0 \leq x \leq 0.9$) are synthesized with control of size, morphology, and composition. The $Co_xFe_{2-x}P$ nanoparticles exhibit composition dependent magnetic properties, while $M_{2-x}Mn_xP$ (M = Co, Fe) nanomaterials are capable of catalyzing water oxidation at low overpotentials with high Faradaic

efficiency. A new protocol is established to combine metal chalcogenide semiconductor aerogels with Ni_2P nanoparticles. The resulting hybrid aerogels are photocatalytically active for the hydrogen evolution reaction (HER).

AUTOBIOGRAPHICAL STATEMENT

Da Li

EDUCATION

2012–2017 Wayne State University, Detroit, MI **Ph.D., Chemistry**
2007–2011 East China University of Science and Technology, Shanghai, China **B.S.,Chemistry**

HONORS AND AWARDS

2017 The Electrochemical Society Student Poster Contest 2nd Place
2017 The Michigan Catalysis Society (MCS) Outstanding Student Presentation Award
2017 Esther and Stanley Kirschner Graduate Award in Inorganic Chemistry
2017 WSU Graduate & Postdoctoral Research Symposium Presentation Award
2017 Summer Dissertation Fellowship
2015 Thomas C. Rumble University Graduate Fellowship
2014 Graduate School Citation for Excellence in Teaching Service
2013 Department Citation for Excellence in Teaching Service
2011 Outstanding Undergraduate Student in Science and Engineering of ECUST

PUBLICATIONS

1. **Li, D.**, Whisnant K. G., Brock, S. L. "Visible Light Induced Photocatalytic Hydrogen Evolution Using a Ni2P-CdS Hybrid Aerogel System." *In preparation.*
2. **Li, D.**, Liyanage, D., Brock, S. L. "Compositional Tuning of Catalytic and Magnetic Function in Nanoscale Transition Metal Phosphides." ***Account of Chemical Research****, Invited manuscript in preparation.*
3. Liyanage, D., **Li., D.**, Cheek, Q. B., Brock, S. L. 2017**, *Journal of Material Chemistry A,* *In revision***.
4. Korala, L., Germain, J. R., Chen, E., Pala, I. R., **Li, D.**, Brock, S. L. ***Inorganic Chemistry Frontiers***, 2017, Accepted
5. **Li, D.**, Baydoun, H., Kulikowski, B., Brock, S. L. ***Chemistry of Materials***, 2016, 29, 3048-3054.
6. **Li, D.**, Perera, M., Kulikowski, B., Lawes, G., Seda, T., Brock, S. L. ***Chemistry of Materials***, 2016, 28, 3920-3927.
7. **Li, D.**, Baydoun, H., Verani, C. N., Brock, S. L. ***Journal of the American Chemical Society****,* 2016**,** 138, 4006-4009.
8. **Li, D.**, Senevirathne, K., Aquilina, L., Brock, S. L. ***Inorganic Chemistry****,* 2015, 54, 7968-7975
9. **Li, D.**, Xie, H., Zhang, M., Liu, J., Yang, X. ***NANO***, 2012, 07, 115002-115008.
10. **Li, D.**, Xie, H., Duan, C. Liu, J. ***Journal of Experimental Nanoscience****,* 2011, 6, 209-216.
11. Wang, J., **Li, D.**, Liu, J., Yang, X., He, J. Lu, Y. ***Soft Nanoscience Letters***, 2011, 1, 81-85.
12. **Li, D**., Liu, J. ***Paint & Coatings Industry***, 2010, 40, 67-70.